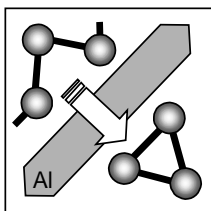




# The aluminium-induced layer exchange forming polycrystalline silicon on glass for thin-film solar cells



Dissertation  
zur  
Erlangung des Doktorgrades  
der Naturwissenschaften  
(Dr. rer. nat.)

dem  
Fachbereich Physik  
der Philipps-Universität Marburg  
vorgelegt von

Oliver Nast  
aus Stuttgart

Marburg/Lahn 2000

Vom Fachbereich  
der Philipps-Universität Marburg als Dissertation am 14. Sept. 2000  
angenommen.

Erstgutachter Prof. Dr. W. Fuhs  
Zweitgutachter Prof. Dr. G. Weiser  
Tag der mündlichen Prüfung am 2. Nov. 2000

# Contents

<b>Zusammenfassung .....</b>	<b>5</b>
<b>Chapter 1: Introduction.....</b>	<b>7</b>
<b>Chapter 2: Metal-induced crystallization of amorphous silicon.....</b>	<b>11</b>
2.1 Metal and a-Si interaction .....	11
2.2 The Al and Si layer exchange process.....	17
<b>Chapter 3: Experimental .....</b>	<b>23</b>
3.1 Preparation.....	23
3.2 Characterisation.....	25
<b>Chapter 4: Parameters of the Al-induced layer exchange process .....</b>	<b>29</b>
4.1 Si grain formation and growth.....	29
4.2 Al and a-Si layer thickness ratio.....	35
4.3 Temperature dependence.....	38
4.4 Influence of the polycrystalline Al.....	40
4.5 The Al/Si interface layer .....	42
4.5.1 Microscopical investigations.....	42
4.5.2 XPS measurements.....	46
4.5.3 No interface oxide .....	51
<b>Chapter 5: Characterisation of the poly-Si films on glass .....</b>	<b>55</b>
5.1 The Al content.....	55
5.2 Grain structure and orientation.....	59
5.3 Electrical properties.....	69
5.3.1 Hall effect measurements .....	69
5.3.2 Influence of the annealing temperature .....	73

5.3.3 Substitutional and non-substitutional Al concentration .....	74
<b>Chapter 6: Model of the layer exchange process.....</b>	<b>79</b>
6.1 The overall layer exchange .....	79
6.2 Interface interaction .....	82
6.3 Crystallization .....	86
6.4 Si grain growth.....	91
6.5 Discussion .....	97
<b>Chapter 7: Al-induced layer exchange for thin-film solar cells.....</b>	<b>101</b>
7.1 ALILE engineering for seeding layers.....	101
7.2 ALILE poly-Si absorber layers .....	108
<b>Chapter 8: Conclusions .....</b>	<b>113</b>
<b>References.....</b>	<b>117</b>
<b>Acknowledgments .....</b>	<b>125</b>
<b>List of publications .....</b>	<b>127</b>

# Zusammenfassung

In der vorliegenden Arbeit wird der aluminiuminduzierte Schichtaustausch von Silicium- und Aluminiumfilmen auf Glas entwickelt und untersucht. Er basiert auf der aluminiuminduzierten Kristallisation von amorphen Silicium (a-Si) bei Temperaturen unter der eutektischen Temperatur des Si/Al-Systems von  $577^{\circ}\text{C}$ . Der aluminiuminduzierte Schichtaustausch stellt ein Verfahren dar, das ermöglicht, zusammenhängende, großkörnige polykristalline Siliciumfilme (poly-Si) auf Glas zu erzeugen. Die Untersuchungen sind im Bereich der Entwicklung von Dünnsolarzellen auf Siliciumbasis angesiedelt. In diesem Bereich ist die Prozessierung von großkörnigen poly-Si-Filmen auf Niedertemperatursubstrate von besonderer Bedeutung. Beim gegenwärtigen Stand der Forschung werden die zunächst amorphen Siliciumfilme mit Hilfe der Laser- oder Festphasenkristallisation umgewandelt. Der aluminiuminduzierte Schichtaustausch zeichnet sich gegenüber diesen Kristallisationsverfahren durch folgenden Vorteile aus: (i) Relativ kurze Prozessierungszeiten ( $\sim 30$  min) verglichen zur Festphasenkristallisation, (ii) einfaches isothermisches Heizen verglichen zur Laserkristallisation und (iii) echtes Niedertemperaturverfahren ( $< 550^{\circ}\text{C}$ ).

In dieser Arbeit wurden sowohl die Prozessschritte des aluminiuminduzierten Schichtaustausches im Temperaturbereich von  $350^{\circ}\text{C}$  bis  $525^{\circ}\text{C}$  untersucht als auch die gewachsenen poly-Si Filme charakterisiert. Die wichtigsten Ergebnisse sind:

- Die Atome des amorphen Silicium lösen sich im Kontakt mit dem Al-Film. Die im Al gelösten Si-Atome kristallisieren an der Al/a-Si-Grenzfläche. Die gebildeten Si-Keime wachsen durch weitere Siliciumdiffusion in der Al-Schicht, bis sie vom Glassubstrat und der Al/a-Si-Grenzfläche im vertikalen Wachstum begrenzt werden. Das laterale Wachstum wird fortgesetzt, bis benachbarte Si-Körner zusammenstoßen und einen kontinuierlichen poly-Si-Film bilden. Das Al, indem die Si-Kristallisation und das Wachstum erfolgt, wird von der kristallinen Si-Phase verdrängt. Als Gesamtreaktion findet ein Austausch der Al- und Si-Schichten statt. Die Dicke des poly-Si Films ist durch die Al-Schicht bedingt.
- Für den Schichtaustausch ist eine Oxidgrenzschicht zwischen den a-Si- und Al-Filmen notwendig. Diese Oxidschicht bleibt zwischen den beiden Schichten stabil, obwohl

praktisch alle Al- und Si-Atome während der Kristallisation die Seite bezüglich dieser Grenzschicht wechseln.

- Der Schichtaustausch wird folgendermaßen von Prozessparametern beeinflusst: Die Si-Körner sind um so größer, (i) je niedriger die Kristallisationstemperatur ist, (ii) je größer die Körner des polykristallinen Aluminiumfilms sind und (iii) je dicker das Grenzflächenoxid ist. Bei der Bildung großer Si-Körner ist jedoch der Gesamtprozess verlangsamt. Die Schichtreihenfolge spielt für den Prozeß des Al/Si-Schichtaustausches eine untergeordnete Rolle, jedoch können durch Beeinflussung des Grenzflächenoxids und der Struktur des poly-Al-Films in einem mehrlagigen Al/Si-System selektiv Schichten getauscht werden.
- Die poly-Si-Filme bestehen aus Körnern, die je nach Prozessparametern einen Durchmesser von 10  $\mu\text{m}$  und mehr haben können. Die Filme zeigen eine (100)-Vorzugsorientierung. Das Material weist eine Al-Konzentration von  $3 \times 10^{19} \text{ cm}^{-3}$  auf. Ein großer Teil dieser Al-Atom besetzt substitutionelle Si-Gitterplätze und bewirkt eine Löcherkonzentration von ca.  $2 \times 10^{18} \text{ cm}^{-3}$ . Die Löchermobilität ist zwischen 55 und 70 cm/Vs. Sie reicht somit an die von kristallinem Si in diesem Dotierungsbereich heran.

Basierend auf den Ergebnissen der Untersuchungen wird ein Modell für den aluminiuminduzierten Schichtaustausch aufgestellt. Der Prozess der a-Si-Dissoziation, Si-Diffusion und anschließender Si-Kristallisation in der Al-Matrix lässt sich mit diesem Modell auf den Unterschied der chemischen Potentiale des Silicium an den a-Si/Al und Al/c-Si Grenzflächen zurückführen. Das Wachstum von großkörnigen polykristallinem Silicium kann damit beschrieben werden, dass die Si-Verarmungsgebiete, die die wachsenden Si-Körner innerhalb der Al-Matrix umgeben, zu einem frühen Stadium der poly-Si Filmbildung wechselwirken und weitere Si-Nukleation unterbinden.

Aufgrund der Möglichkeit großkörniges poly-Si auf Glas mit einfachen Techniken bei niedrigen Temperaturen zu prozessieren, ist der aluminiuminduzierte Schichtaustausch eine faszinierende Methode. Neben Aluminium sind andere Metalle, die die Kristallisation induzieren, denkbar, aber auch andere Schichtstrukturen und andere Temperaturbehandlungen. Die vorliegende Arbeit ist somit erst die Spitze des Eisberges in einem neuen Feld der poly-Si-Bildung durch den metallinduzierten Schichtaustausch.

# Chapter 1:

## Introduction

"We enter the new millennium in a period of rapid evolution of photovoltaics and with high hopes for the future of this technology. We are fortunate to live in exciting times!", wrote K. Zweibel and M.A. Green in the editorial of the millennium special issue of the journal *Progress in Photovoltaics: Research and Applications* [1]. The rapid evolution is driven by the need to supply the world's growing demand for energy while limiting the impact of climate change caused by carbon dioxide emissions [2]. The direct conversion of sunlight into electricity using solar cells will contribute an increasing share to the overall energy production in the future. The size of market share strongly depends on the possible reduction of production cost for photovoltaic energy. In the current state of the photovoltaic industry, the solar cell production is dominated by crystalline silicon with a market share of over 80 % [3]. The material of the remaining 20 % is mainly amorphous silicon. However, mono- and multicrystalline Si wafer-based technology severely limits cost reduction due to a list of critical issues [4]: (i) Complex production steps of the solar cells and modules, (ii) considerable material loss during wafer fabrication, (ii) cell size is limited to wafer size, (iii) external assembling and serious connection to form larger modules, and (iv) large amount of highly purified feedstock is required. To overcome this predicament, thin-film solar cell technology, where the photoactive layer is directly deposited onto a foreign substrate, has been extensively investigated. This technology seems to be a promising alternative to achieve efficiencies at least as high as the current commercial wafer technologies of about 15%, but at significantly lower production costs [5].

At present, thin-film solar cells, based on amorphous silicon (a-Si:H), cadmium telluride CdTe and chalcopyrites  $\text{Cu}(\text{In,Ga})(\text{S,Se})_2$ , are already commercially available or on the verge of commercialisation [6]. However, amorphous silicon technology suffers from low efficiencies. Substantial effort has been made to compensate for this disadvantage by introducing sophisticated double and triple junction solar cells, also based on amorphous alloys. Nevertheless, the stabilised efficiencies have stayed below 13% up to

now [6]. Additionally, it has to be taken into account that the more sophisticated the solar cell structures, the smaller the margin of reducing cell production costs [7]. Non-silicon based solar cells suffer from two types of disadvantages: (i) Toxicity [8] and (ii) scarcity of some of the material components [9]. Both disadvantages become critical issues when photovoltaics is considered as a technology to supply energy world-wide on a GW-scale.

Compared to the cell technologies mentioned above, crystalline Si thin-film technology is at the beginning of its development. Silicon has significant advantages over other solar cell materials. It is non-toxic and the second most abundant element on the earth's crust [10]. Until recently, it was believed that crystalline silicon (c-Si) thin-film solar cells ought to be at least 10  $\mu\text{m}$  in thickness to achieve reasonable efficiencies (>10%) due to the fact that c-Si is an indirect semiconductor with weak light absorption [11]. However, advanced light trapping schemes open the way to use thinner films and still maintain high efficiencies [12,13]. Efficiencies as high as 10.1% have been reported for 2.0  $\mu\text{m}$  thick microcrystalline Si solar cells [14].

One of the main obstacles that hampers the development of Si thin-film solar cells is the difficulty of processing crystalline silicon layers onto foreign substrates. To achieve efficiencies in the range of 15% and above large-grained polycrystalline silicon films seem to be mandatory [15]. The deposition of silicon on foreign substrates is most commonly carried out using chemical vapour deposition techniques [16]. However, this type of deposition directly onto amorphous substrates leads to microcrystalline Si with grain sizes typically in the range of tens of nm. Alternatively, silicon is epitaxially grown onto Si wafers at high temperatures [15]. The grown monocrystalline Si film can be detached from the Si wafer and attached to any other substrate because the film/wafer interface is either partially oxidised or of porous nature. The Si wafer is believed to be reused many times. Although, this technological development reduces material loss, it retains most of the disadvantages of Si wafer-based technology listed above. The margin of cell production costs therefore appears small.

Instead of depositing crystalline silicon directly onto the foreign substrate, research efforts have been directed to initially deposit amorphous silicon and then transform the amorphous to the crystalline phase using various crystallization techniques. The studies concerning this topic can be separated into two categories: High and low temperature crystallization [11]. The process temperature dictates what kind of substrates can be used and, therefore, influences the substrate cost predominantly. In the high temperature

approach ( $\sim 1000^\circ\text{C}$ ), expensive substrates such as graphite, quartz, special high-temperature glass or high-temperature ceramics have to be used, which withstand the processing temperature. Si grains with sizes of several mm can be processed by melting the amorphous silicon prior to crystallization. The techniques used are either zone-melting recrystallization or large-area melting steps [17]. The main drawback of the high-temperature approach is the limited choice of substrates, which decreases the potential of substantially reducing solar cell production costs compared to conventional wafer-based technology.

In the low-temperature approach ( $< 600^\circ\text{C}$ ), cheap substrates such as conventional glass can be used. This advantage implies the potential of cost-efficient thin-film solar cell production. However, the formation of large-grained poly-Si films at such low temperatures is a major challenge. The transformation of amorphous silicon to polycrystalline silicon (poly-Si) on low-temperature substrates has been extensively investigated using solid phase crystallization (SPC) [18,19] or laser crystallization (LC) [20,21]. SPC is based on isothermal annealing of a-Si at temperatures of about  $600^\circ\text{C}$ . At these temperatures poly-Si films with grain sizes of several  $\mu\text{m}$  are slowly formed over extended periods of time ( $>10$  h) [18]. The crystallization temperatures, which are still relatively high, and the long processing times are the main disadvantages of SPC and are probably the reasons why research activities in this area have decreased in recent years. When using LC, the a-Si is liquefied for a very short time with laser pulse periods of less than 100 ns [22]. The achievable Si grain sizes of the crystallized material are in the  $\mu\text{m}$  range and of good crystallographic quality [23]. However, possible contamination of the molten Si from low-temperature substrates is still under debate. LC, based on Excimer-laser technology, can also be regarded as an expensive technique compared to simple furnace annealing processing. Furthermore, major obstacles could arise when LC is implemented to process large-area poly-Si thin-films on an industrial scale.

An alternative crystallization process to LC and SPC is metal-induced crystallization (MIC). Certain metals in contact with amorphous silicon induce the transformation process from the amorphous to the crystalline phase at temperatures well below the eutectic temperature of the metal/Si system. MIC is of interest for the formation of poly-Si thin-films on foreign substrates, since some of the crystallization temperatures are within the framework of the low-temperature approach. Although, MIC has been investigated over several decades [24], it seems that this type of crystallization technique has recently gained increased attention in the field of thin-film devices [25-29].

The aluminium-induced layer exchange process investigated in this work is based on aluminium-induced crystallization. The process fits well within the framework of developing a crystallization technique under the following requirements: (i) Low-temperature process ( $< 550^{\circ}\text{C}$ ), (ii) cost-efficient substrates (glass), (iii) industrially relevant deposition techniques (thermal evaporation and sputtering deposition), (iii) relatively short crystallization time ( $\sim 30$  min) and (iv) simple. To the best of the author's knowledge, there have not been any reports on an aluminium-induced layer exchange of Al/a-Si systems on foreign substrates prior to this work. It is the first time that this layer exchange phenomenon has been studied for the formation of large-grained poly-Si films on glass. There seem to be some parallels between the flux-method concept developed by the company Kyocera and this study, however, very little information has been published on the flux-method process itself [30].

The work presented is structured into six main chapters. Chapter 2 following this general introduction provides some background information on studies concerned with metal-induced crystallization. All investigations discussed fit within the low-temperature approach. Additionally, the chapter gives an introduction to the aluminium-induced layer exchange phenomenon as a special metal-induced crystallization process. This more specific introduction also builds up the outline of the subsequent investigations. After a brief presentation of the experimental details in chapter 3, chapter 4 analyses the poly-Si layer formation and various process parameters. In chapter 5, the polycrystalline Si thin-films are characterised concerning their Al content, their grain structure and their electrical properties. Chapter 6 finally brings together the results presented and partially discussed in the previous chapters attempting to give a comprehensive model of the aluminium-induced layer exchange process. The major process steps are analysed to draw a picture of the crystallization process from start to finish. For the sake of comprehensiveness, steps, where still little is known about the detailed mechanisms, are also discussed to highlight gaps in the understanding of individual sub-processes. Chapter 7 gives an outline of the possible uses of poly-Si films formed by the aluminium-induced layer exchange process for Si thin-film solar cells.

The work presented on the aluminium-induced layer exchange can probably be regarded as the tip of the iceberg of a new way of fabricating large-grained polycrystalline silicon thin-films by low-temperature metal-induced layer exchange processes.

## Chapter 2:

# Metal-induced crystallization of amorphous silicon

The following brief overview addresses the crystallization of amorphous silicon when in contact with metals. It focuses on metal-induced transformation of a-Si at temperatures below the eutectic temperature of the related Si/metal system. The crystallization is, therefore, a solid phase transition according to the binary phase diagram. The overview focuses on the idea of investigating low-temperature crystallization of a-Si for low-cost Si thin-film solar cells. It excludes literature on Si thin-film studies where poly-Si containing very large grains ( $\sim 100 \mu\text{m}$ ) was grown from metal solutions for the potential use in solar cell fabrication (e.g. [31,32]). The reason for this is that the processing temperatures are generally high and are, therefore, not compatible with low-cost foreign substrates. In addition to the literature overview in chapter 2.1, chapter 2.2 gives a brief introduction to the layer exchange phenomenon, which is the subject of the entire study presented. This introduction provides the reasoning for the outline of the following investigation and therefore helps to produce a complete picture of the studies on isolated process parameters reported in this work.

## 2.1 Metal and a-Si interaction

The interaction of amorphous silicon in contact with various metals has already been studied over the last several decades. Nevertheless, many questions still remain open. The scientific as well as the technological attraction of the metal/a-Si system is based on the fact that amorphous silicon, when in contact with certain metals transforms into crystalline Si at temperatures much lower than the commonly reported temperature for solid phase crystallization of bare a-Si, which is about  $600^\circ\text{C}$  at the lower limit [18,33]. Furthermore, the transformation temperatures are significantly below the eutectic temperatures of the

Si/metal systems. Table 1 lists some Si/metal systems with their eutectic temperatures  $T_{eu}$  and the reported crystallization temperatures  $T_{cryst}$ :

metal	$T_{eu}$ (°C)	$T_{cryst}$ (°C)	Reference
Al	577	150	[34]
Ag	830	350	[35]
Au	360	130	[36]
Sb	630	430	[37]
Cu	802	485	[38]
Ni	964	500	[39]

Table 1: List of Si/metal systems with their eutectic temperatures and crystallization temperatures reported. All eutectic temperatures are taken from Ref. [40].

Herd et al. have given a distinction between the different a-Si/metal systems [24]. On one hand, there is the category of simple eutectic systems (SE systems) such as Al/Si, Au/Si, or Ag/Si. Within these systems there is no formation of stable silicides in thermodynamic equilibrium. However, metastable silicide transition phases might be involved in the metal-induced crystallization (MIC) process [36,41]. The possible role of an intermediate phase in Al-induced crystallization of a-Si will be discussed in chapter 6.1. On the other hand, there is the category of compound forming metal/Si systems (CF systems) such as Ni/Si, Pd/Si or Cu/Si. In these systems stable metal silicide phases exist in thermal equilibrium and play an important role during the crystallization process. Both categories will be discussed here. The emphasis will, however, be on the simple metal/Si systems, since they are the most relevant for the work presented.

The following discussion will begin with the category of the compound forming metal/Si systems, and will initially focus on Ni as the crystallization inducing metal, because Ni has attracted the widest attention recently [25,26,39,42,43]. The interest in Ni-induced crystallization is fuelled by the idea to replace the a-Si in thin-film transistors with low-temperature poly-Si material for improved application in active-matrix liquid crystal display devices. Ni seems to be a promising candidate to crystallize a-Si for use in this field [25]. Hayzelden and Batstone have investigated Ni-induced crystallization by studying the transformation of Ni-implanted amorphous Si [42,44], whilst Jin et al. conducted research on Ni-covered a-Si thin-films [43]. In both cases it seems that the fundamental crystallization process follows the same rules. In the initial phase of the

process, a metallic silicide, specifically  $\text{NiSi}_2$ , is either formed at the Ni/a-Si interface, as in the study of Jin et al., or as  $\text{NiSi}_2$  precipitates within the Ni-implanted a-Si material. The  $\text{NiSi}_2$  precipitates migrate in the form of nodules through the amorphous silicon phase leaving a trace of c-Si behind as schematically described in Fig. 1. The Ni-silicide is at the planar growth front of the c-Si needle. Hayzelden and Batstone used a dissociation mechanism to describe the growth process [42]. This mechanism is based on the fact that the chemical potential of Ni is lower at the  $\text{NiSi}_2$ /a-Si interface, whereas the chemical potential of Si is lower at the  $\text{NiSi}_2$ /c-Si interface. The  $\text{NiSi}_2$  layer dissociates at the Ni silicide/c-Si interface to provide free silicon atoms for the Si crystal growth. Ni, enriched at this interface, diffuses to the  $\text{NiSi}_2$ /a-Si interface where new  $\text{NiSi}_2$  is formed. Consequently, a net migration of the Ni silicide occurs transforming amorphous to crystalline silicon, driven by the overall reduction of Gibbs energy.

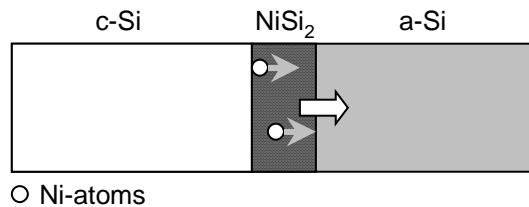


Fig. 1: Schematical diagram of Ni-induced crystallization according to Refs. [42] and [43].

If the above stated model for the Ni/Si system is generalised, it can be summarised that in CF systems, it is not the metal itself that directly mediates the crystallization process. It is a form of the metal silicide that induces the transformation of the amorphous to the crystalline Si phase. Additionally, it is noteworthy that the individual Si atoms do not strongly change their local position by long range diffusion, rather, their surrounding changes. Initially, the Si atoms are incorporated in the amorphous Si matrix. During the migration of the  $\text{NiSi}_2$  nodules the surrounding of the individual Si atom transforms to a Ni silicide. Finally, the Si is released by the dissociation of the  $\text{NiSi}_2$  at the  $\text{NiSi}_2$ /c-Si interface and incorporated into the crystalline Si structure. The maximal relocation distance of a Si atom is given by the possible diffusion length of the atom through the migrating Ni silicide. The thickness of the planar  $\text{NiSi}_2$  growth front is stated as 5 nm [42].

Whilst the discussion of compound forming metal/Si systems was kept brief, the following discussion on the category of simple eutectic systems has to be more in depth, since the Al/Si system investigated in this work falls into this category. Herd et al. claimed to have found a simple relationship between the eutectic melting temperature,  $T_{\text{eu}}$ , and the temperature of the on-set of the metal-induced crystallization of a-Si in SE systems [24].

However, their rule that the crystallization temperature is  $0.72 \times T_{eu}$  ( $T_{eu}$  in Kelvin) is no longer valid when more recent literature is considered (see Table 1). Nevertheless, the crystallization process in SE systems seems to be of a common nature. The process can be separated into three major steps: (i) the dissociation of Si atoms from the amorphous silicon into the metal, (ii) the diffusion of the Si atoms through the metal, and (iii) the incorporation of the dissolved Si atoms to the growing Si crystals. These Si crystals have either nucleated at the Si/metal interface or within the metal itself, fed from the Si solute. This simplified three step description of the crystallization process in SE systems was adapted by Bian et al. to explain their findings on the formation of large Si grains ( $\sim 1 \mu\text{m}$ ) in an a-Si/Ag/a-Si trilayer structure [35]. Tsai et al. could also explain the interfacial reactions between Au and hydrogenated amorphous Si, observed in their investigation, using this model [45]. Regarding the Al/Si system, Konno and Sinclair have conducted ex- and in-situ cross-section transmission electron microscopy studies [46,47]. They gave evidence that in an Al/a-Si multilayer structure heated to  $200^\circ\text{C}$  the formation of crystalline Si nuclei occurs within the Al layers accompanied by the dissociation of the a-Si layer. The results were interpreted as an indication that the Si atoms diffuse through the Al to undergo the transition from the amorphous to the energetically more favourable crystalline phase. The phenomenological dissociation-diffusion-crystallization model is therefore supported by these studies.

So far, the discussion of the SE systems was limited to the transformation of amorphous to crystalline silicon. However, metals of the SE systems also mediate the rearrangement of polycrystalline silicon. Allen et al. studied the interaction of poly-Si in contact with Au [48,49]. They showed that at temperatures below  $300^\circ\text{C}$ , initially large Si grains of the polycrystalline material increase their size even further, at the expense of smaller grains. The low temperature for the restructuring of the poly-Si material is due to an Au-mediated process, according to Allen et al. The smaller Si grains are dissociated by the adjacent Au. The dissolved Si atoms diffuse through the metal to the larger crystalline Si grains. Larger grains are more stable due to a reduced ratio of Au/Si surface to crystalline volume. Results, very similar to those for the Au/poly-Si system, have been reported for the interaction of Al with poly-Si material [50,51]. The rearrangement of the Si films involves the dissociation of Si into the Al and the diffusion of the Si atoms through the metal film. These studies concerning the metal/poly-Si interaction also support the dissociation-diffusion-crystallization model.

All the literature concerning the SE systems, as yet discussed, studied the interaction of metals with Si thin-films deposited on foreign substrates or oxidised Si wafers. However, SE systems are also used to induce epitaxial growth on crystalline Si substrates, called solid phase epitaxy (SPE). In the field of SPE, special attention has been paid to Al-induced crystallization of a-Si. Majni et al. reported that when a c-Si wafer is covered by an Al layer (700 nm) and an a-Si film (650 nm) the Si is dissolved and transported to the c-Si wafer [52]. The dissolution and diffusion of the Si takes place at temperatures well below the eutectic temperature of 577°C, and the dissolved Si grows epitaxially onto the c-Si. The newly formed Si layer is p-type with a hole concentration of  $2 \times 10^{18} \text{ cm}^{-3}$  according to Hall effect measurements. Fig. 2 gives a schematical description of the overall process of SPE.

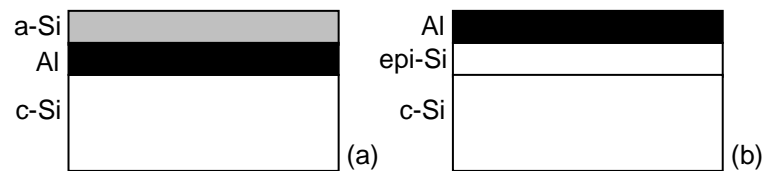


Fig. 2: Schematical diagram of solid phase epitaxy of a-Si onto a c-Si wafer; (a) the initial layer structure before annealing and (b) after annealing at temperatures between 400°C and 500°C. Epi-Si stands for epitaxially grown silicon.

Solid phase epitaxy of amorphous silicon has gained interest in the field of photovoltaics as a low-temperature process capable of forming good-quality epitaxial p-type Si layers. Tsaur et al. applied this process to the fabrication of a solar cell. They grew an epitaxial p-type Si layer on top of an n-type monocrystalline Si wafer [53]. The Al that had segregated to the surface was selectively etched away and contacts were deposited. Their solar cell had an open-circuit voltage of 0.54 V, a short-circuit current density of  $26 \text{ mA/cm}^2$  and a fill factor of 0.75 without any anti-reflection coating. The measured efficiency was 10.4 %. Besides processing pn-junctions on n-type wafers, Koschier et al. recently suggested the use of SPE for the formation of back-surface field layers on p-type substrates [54], and Wenham et al. used SPE, which they renamed to metal-mediated epitaxial growth, to investigate their thyristor photovoltaic devices [55].

When considering metal-induced crystallization for Si thin-film solar cells, two aspects must be kept in mind: (i) The localisation of the metal after the crystallization process and (ii) possible incorporation of metal impurities in the poly-Si material. Regarding the first aspect, in SE systems the metal, mediating the Si growth, seems to be repelled from the growing crystalline phase, since no stable metal silicide can be formed. Konno and Sinclair

have shown in TEM investigations that Al is ejected from its original position when the Si nucleation and growth occurs within the Al layer [46]. A similar effect of metal replacement has been discussed by Allen et al. in their study of the Au/poly-Si interaction [48]. The solid solubility of the metal in the crystalline Si phase for Al and Au is about  $10^{-2}$  at.% and  $10^{-4}$  at.%, respectively [56], thus, in both cases very low. In contrast to SE systems, the incorporation of metal silicide in the crystallized region cannot be excluded when dealing with CF metal/Si systems. In respect to small devices, e.g. thin-film transistors, the MIC process can be conducted in such a way that the residual  $\text{NiSi}_2$  phase is extracted from the active device area [25]. However, for large-area devices, e.g. solar cells, a localisation of areas harmful to the performance outside the active area does not seem to be feasible. The use of SE systems to form poly-Si films is therefore more promising with regard to photovoltaic applications.

When addressing the second aspect, i.e. the possible incorporation of metal atoms in the poly-Si material, the energy levels of incorporated metal impurities in c-Si are of interest. Ni as well as Au introduce deep states in the energy band gap of Si, whilst Al impurity level is only about 60 meV above the valence band [57]. Deep states are harmful to the photovoltaic performance of the device due to the enhanced Shockley-Read-Hall recombination, which results from their presence. This means that Ni and Au seem to be unsuitable as crystallization mediating metals when fabricating photovoltaic devices. By comparison, the shallow impurity states caused by Al give rise to p-type doping when the Al atoms occupy Si lattice sites (see chapter 5.3.). Incorporation of Al during the aluminium-induced crystallization process could therefore be beneficial for subsequent solar cell device fabrication depending on the solar cell structure, since p-type Si material is automatically formed during the process.

From a photovoltaic point of view, a crystallization process, which transforms amorphous silicon on low-cost substrates to poly-Si, is desired. The process requirements are: (i) Low-temperatures, (ii) the formation of continuous high-quality Si layers over large areas, and (iii) minimal potential of incorporating harmful impurities during the process. The first requirement is generally fulfilled by metal-induced crystallization as described above. It will be shown during this study that a layer exchange process based on aluminium-induced crystallization is able to match the latter two requirements, as well. The approach chosen is that Al and a-Si layers are subsequently deposited and a separate isothermal annealing process is employed. During this annealing step an Al-induced layer exchange occurs, which leads to the formation of a continuous poly-Si layer at low

temperatures on glass with a high crystallographic quality as documented in the following chapters. This has not been achieved by metal-induced crystallization prior to this study to the best of the author's knowledge.

An attempt to give an overview on MIC investigations relevant to this work ought to include approaches where Al induces crystallization already during the Si deposition. Drüsedau et al. have studied the formation of polycrystalline Si when deposited onto Al coated substrates at elevated temperatures [58,59]. The Al layers were between 4 and 32 nm thick. The subsequent deposition of 500 nm Si was conducted at a constant substrate temperature of 227°C. The silicon layer crystallized during the deposition and contained Si crystallites of about 10-30 nm in size. However, the Al is distributed in the crystallized region of the film, and no pure continuous poly-Si layer is formed. Boreland et al. reported similar difficulties in their studies on aluminium-induced crystal growth during chemical vapour deposition of Si [28]. The average grain size of their Si thin-films was only about 70 nm, and the Si films still contained a substantial amount of Al.

## 2.2 The Al and Si layer exchange process

The phenomenon investigated in this work is the aluminium-induced layer exchange process (ALILE). In this process, adjacent aluminium and amorphous silicon layers exchange places when heated at temperatures well below the eutectic temperature of the Si/Al binary system. All experimental details will be described in chapter 3. At this point, the key results and the basic parameters of this layer exchange are to be introduced, which leads to an outline of the investigation and discussion of the process subsequently presented.

The overall Al-induced layer exchange phenomenon is shown in Fig. 3. The initial system is a stacked Al and Si layer structure on glass. When this structure is heated, a layer exchange process occurs. During the exchange, a polycrystalline silicon layer is formed at the original position of the Al film. After selective removal of the Al that has segregated to the top of the Si film, a continuous poly-Si layer remains on the glass substrate, as revealed in Fig. 3c.

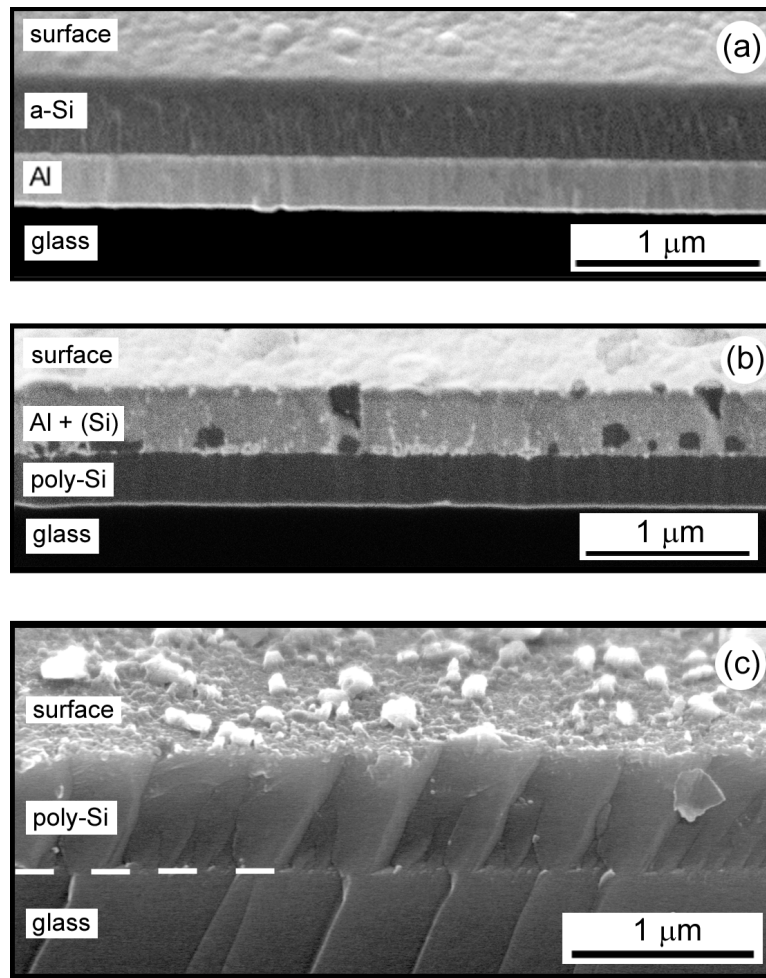


Fig. 3: Cross section FIB micrographs of the glass/Al/a-Si structure: (a) before annealing and (b) after annealing for 1 h at 500°C. (c) SEM micrograph after Al etching, exposing the continuous poly-Si layer. In (a) and (b) the samples are tilted by 45°, and in (c) the sample is tilted by 20°, therefore the scales are only valid horizontally. The short white dotted line in (c) is a guide to the eye.

The crystalline nature of the Si layer after ALILE was verified using Raman spectroscopy. Fig. 4 shows two spectra of a poly-Si layer on glass after crystallization. They were taken from the surface as well as from the interface between the Si film and the substrate, although the signal to noise ratio of the Raman signal detected through the glass was decreased. The peak maxima of the spectra are at  $520\text{ cm}^{-1}$ . There is no Raman response at  $480\text{ cm}^{-1}$  that would indicate an amorphous phase in the Si material [16]. The matching line shapes of the two peaks indicate that the crystalline character of the film is uniform throughout the film thickness. To verify that the crystallization is induced by the Al layer, an identical sample but without Al was subjected to the same annealing process. It is apparent from Fig. 4 that this Si film remained amorphous. Thus, it is the Al layer that is responsible for the transformation of an a-Si film into a poly-Si layer.

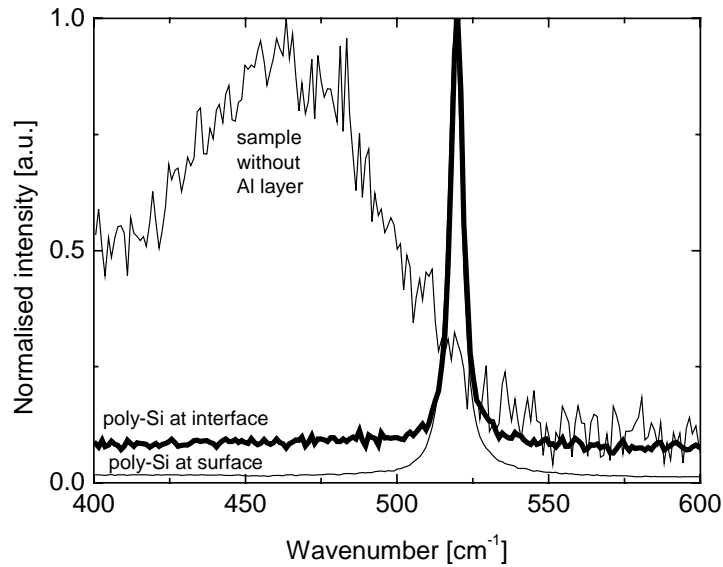


Fig. 4: Raman spectra of a sample annealed at 480°C for 45 min taken at the interface and the surface; the spectrum of an identical sample having undergone the same annealing treatment but without Al is also shown.

Raman measurements can also give a first impression of the good crystallographic quality of the poly-Si material. Fig. 5 depicts two Raman spectra comparing monocrystalline Si (c-Si) to poly-Si processed by ALILE. For better comparison each spectrum is normalised to its peak maximum. The peak position of the poly-Si film is identical to that for c-Si material indicating that the film is under no or negligible stress [60]. The analysis of the Raman spectrum of the poly-Si layer reveals that the signal is subject to greater noise than the comparative polished Si-wafer. This noise is due to higher surface roughness. Subtracting the background noise in Fig. 5 leads to an almost complete

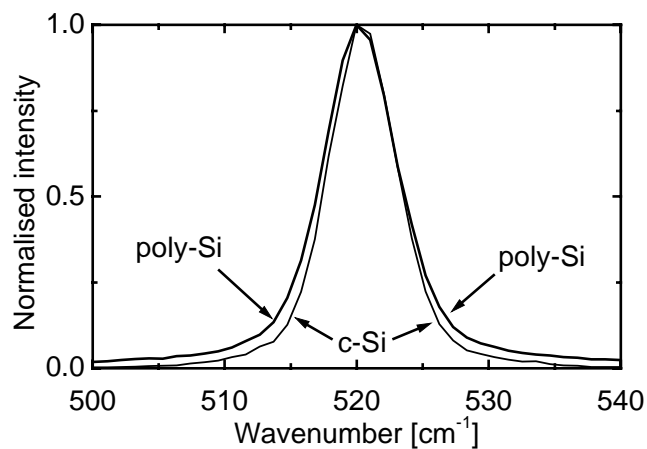


Fig. 5: Raman spectra of a crystallized sample and a polished crystalline Si wafer for comparison. Each spectrum is normalised to its maximum. The Raman signal of the poly-Si film is subject to greater noise due to higher surface roughness.

overlap of the two spectra taking into account the  $1 \text{ cm}^{-1}$  resolution of the Raman system. There is no detectable broadening of the poly-Si peak on the lower energy side, which would be caused by grain size and boundary effects [61]. Fauchet et al. pointed out that the phonon spectrum is not just affected by the grain size but also by defects within the grains [62]. Consequently, the Raman measurements give the first indication of the good crystallographic properties of the poly-Si and the complete crystallization of the amorphous material.

Since the key result of this study is the formation of continuous poly-Si films at low temperatures by an Al-induced layer exchange process, the key questions investigated are: Which process parameters influence the poly-Si formation? What are the properties of the Si layer grown? How is the poly-Si film formed? Why does the layer exchange occur? The work presented intends to provide answers to these questions. It is the isolated investigations - where possible - of the various process parameters that lead to a picture of the Si and Al interaction as well as the poly-Si layer formation. Fig. 6 gives a schematical overview of the set of parameters, which are of particular importance for the layer exchange process.

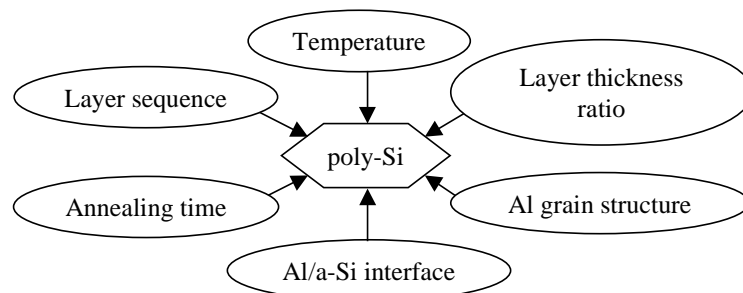


Fig. 6: Schematical presentation of the various influences on the formation of poly-Si by ALILE.

By successively increasing the annealing time, the formation and growth of poly-Si material is studied in chapter 4.1. In chapter 4.2 it will be shown that the ratio of the layer thicknesses of the Al and a-Si films is an inherent parameter of the layer exchange process and of major importance. The influence of the annealing temperature and the grain structure of the polycrystalline Al layer are studied in chapter 4.3 and 4.4, respectively. The layer sequence and the Al/a-Si interface are not entirely separable and will therefore be investigated together in chapter 4.5. It is worthwhile mentioning that the structure of the initial amorphous silicon layer is not listed as a main process parameter. Experiments conducted so far with hydrogenated and non-hydrogenated a-Si deposited using dc magnetron sputtering at various deposition rates have not shown a significant dependence of the layer exchange process on the amorphous structure of the initial Si material. Harris

et al. made similar observations when they compared the interaction of Al with a-Si deposited by electron-beam evaporation and chemical vapour deposition [50]. The structure of the amorphous Si as a process parameter is therefore not discussed in a separate chapter. The study of the ALILE process in conjunction with the analysis of the material properties of the poly-Si films are the basis of a model describing this layer exchange process, which is developed in chapter 6.



# Chapter 3:

## Experimental

This chapter on the preparation and characterisation techniques is kept short, because the standard deposition methods used in this work were conventional sputtering deposition and thermal evaporation. The characterisation methods applied were mainly common electron microscopy and spectroscopy techniques. Brief descriptions will only be given for more “exotic” methods, such as focused ion beam and orientation imaging microscopy. Their particular relevance to the research on ALILE will become apparent when these techniques are discussed in the course of the presentation of specific measurements.

### 3.1 Preparation

The aluminium and amorphous silicon layers were deposited onto glass. The type of glass substrate used was Corning 1737F. This alkaline earth aluminosilicate glass is superior to other commonly used glass substrates such as barium borosilicate glass (Corning 7059). The reason is that its thermal expansion coefficient ( $3.8 \times 10^{-6} \text{ }^\circ\text{C}^{-1}$ ) matches better to the one of silicon ( $2.6 \times 10^{-6} \text{ }^\circ\text{C}^{-1}$ ) compared to borosilicate glass substrates ( $4.7 \times 10^{-6} \text{ }^\circ\text{C}^{-1}$ ).<sup>\*</sup> An additional general advantage of the chosen substrate type is its higher strain point of 666 °C compared to 400-600°C of conventional glass.

Another important piece of information about the substrate is the material composition contained in the glass. Table 2 gives the molecular fractions of compounds of which the glass consists. These fractions given by the manufacturer can be converted to weight and atomic fractions of the individual elements as shown in table 3.

Before any deposition was carried out, the glass substrates were cleaned using RCA1 and an HF dip (dilute HF of about 2%) [63]. The clean substrates were immediately loaded

---

<sup>\*</sup> All material properties stated are extracted from the product information sheet for Corning glass 1737F available for example from Corning International Corporation Australia.

molecules	weight %
SiO <sub>2</sub>	55 to 59
Al <sub>2</sub> O <sub>3</sub>	16 to 18
BaO	7 to 9
B <sub>2</sub> O <sub>3</sub>	7 to 9
CaO	4 to 6
MgO	0.5 to 1
SrO	1 to 2
As <sub>2</sub> O <sub>3</sub>	1 to 2

element	weight %	atomic %
O	49,3	62,2
Si	26,6	19
Al	9,0	6,8
Ba	7,2	4
B	1,2	3,2
Ca	3,6	2,5
Mg	0,6	0,5
Sr	1,7	1
As	0,8	0,8

Table 2: Molecular fraction in Corning 1737

Table 3: Weight and atomic fractions of the elements contained in Corning 1737

into the deposition chambers to deposit various Al and a-Si layer sequences. Generally, the Al film was deposited using thermal evaporation. Prior to the evaporation the chamber was pumped down to  $7 \times 10^{-4}$  Pa. The following deposition was conducted at rates ranging from 0.5 to 10 nm/s. The amorphous silicon was deposited using dc magnetron sputtering at a rate of 25 nm/min in a 1.5 Pa argon atmosphere at 100 W after the base pressure read below  $2.4 \times 10^{-4}$  Pa. A 100 mm, 120  $\Omega$ cm boron doped Czochralski-Si wafer was used as the sputtering target. No substrate heating was employed in either thermal evaporation or sputtering deposition. It has to be noted that the samples were exposed to air during the transfer from one deposition chamber to the other.

The thermal annealing process of the Al and a-Si layer structure was conducted at temperatures ranging from 350°C to 525°C for annealing times from 5 min to 60 h. The heat treatment was mainly performed in a furnace with dry N<sub>2</sub> ambient. It was interrupted by removing the samples from the furnace and cooling them to below 100°C in less than 2 min in a strong N<sub>2</sub> flow. The only exception to this annealing procedure was during time dependent crystallization studies under an optical microscope, which was equipped with a heat stage. The stage could be heated up to the final temperature within 5 min in ambient air. However, within the temperature range investigated, an error of  $\pm 25^\circ\text{C}$  had to be allowed for temperature inhomogeneity within the stage.

To investigate the bare poly-Si layer formed during annealing, the Al that had precipitated on the surface during the process was selectively etched off using a standard Al etching solution (80 parts phosphoric acid, 5 parts nitric acid, 5 parts acetic acid, and 10 parts deionized water at 50°C to 55°C).

## 3.2 Characterisation

The aluminium-induced layer exchange process at temperatures below the eutectic temperature was studied using several microscopical, spectroscopical and electrical techniques. Although most of these techniques are standard characterisation techniques for semiconductor and material research, some specific advantages of the less common ones will be mentioned in the following exposition.

To investigate the interaction of the Al and a-Si layers optical microscopy, scanning electron microscopy {(SEM), Hitachi S900 and S4500} equipped with an energy-dispersive x-ray spectrometer {(EDS), Oxford Link ISIS 200 Microanalysis System} and focused ion beam microscopy {(FIB), FEI FIB200xP}, were employed. The FIB can be exceptionally useful to study the diffusive interaction of layered metal and semiconductor structures. Firstly, the Ga<sup>+</sup> beam of the FIB allows milling of clean cross sections as well as imaging (see for example Olson et al. for more details on FIB microscopy [64]). Secondly, due to the FIB's high voltage contrast between metallic and non-metallic materials, areas of Al and Si can clearly be distinguished. The relationship between the voltage contrast and the type of material was verified by cross sectional energy-dispersive x-ray spectroscopy.

To study the crystallographic structure of the polycrystalline silicon films transmission electron microscopy {(TEM), Philips CM200} and orientation imaging microscopy {(OIM), TexSEM} were used. The OIM captures and analyses the backscattered Kikuchi diffraction pattern (BKD) generated by the crystalline material [65]. The BKD is generated in a SEM set-up and reveals the lattice orientation in the microstructure. Thus, the analysis of the BKDs over an entire region allows to determine grain orientation as well as grain boundaries (GBs) due to the difference of lattice orientation from one side of the grain boundary to the other. The boundary level of the OIM is set to 5° in all measurements presented. The application of an OIM for investigating polycrystalline material will be discussed in chapter 5.2 using orientation imaging micrographs for better explanation. The

OIM studies of the poly-Si grain structure were complemented by utilising the electron channelling contrast of a conventional SEM. This technique enabled the investigation of larger areas of the fully crystallized poly-Si layers than commonly possible in TEM studies. The electron channelling images were made from the former glass/poly-Si interface after lifting the Si films off the glass substrate with concentrated HF. The separated poly-Si layers were turned upside-down and transferred onto metal substrates. This preparation ensured a smooth, clean surface. A secondary electron detector positioned below the objective lens of the SEM recorded a signal with a strong channelling contrast due to sensitivity of the electron backscattering coefficient to the crystallographic orientation of the Si grains [66].

As a standard measurement for the crystallographic quality of poly-Si layer, Raman Spectroscopy (Renishaw Ramascope equipped with a HeNe-Laser, wavelength 632.8 nm) was used. It was separately tested that the laser beam did not induce any crystallization in a-Si films on glass even after extended periods of exposure (>1 h). X-ray diffraction measurements were employed to investigate the orientation of the Si grains of the polycrystalline material. X-ray diffractograms of the poly-Si films were measured in symmetric  $\theta$ - $2\theta$  geometry. A Bruker D8 Advance diffractometer was used which was equipped with a Göbel mirror for parallel beam diffraction [67] and operated with  $\text{CuK}\alpha$  radiation ( $\lambda_{\alpha_1} = 1.5406 \text{ \AA}$ ). In order to obtain a reliable signal-to-noise ratio within a finite measurement time, a position sensitive detector {(PSD), Braun} was used to record the Bragg reflections in the fixed PSD mode. For this purpose the centre of the PSD was set to the scattering angle  $2\theta_0$  of the reflection under consideration, while the tube was positioned at  $\theta_0$ . Prior to the measurements of poly-Si films the PSD mode was verified for a quartz standard sample to yield the same relative intensities as in the usual locked-coupled mode for which both the X-ray tube and the PSD are step-wise moved along the  $\theta$  and  $2\theta$  circle, respectively.

The Al quantities remaining in the crystallized silicon were detected using secondary ion mass spectroscopy (SIMS); whilst the Si-O and Al-O compound distribution before and after the layer exchange process was qualitatively investigated with x-ray photoelectron spectroscopy (XPS). The XPS analysis involved the usage of a VG ESCALAB 220i XL surface science instrument that was equipped with a monochromated Al  $\text{K}\alpha_1$  X-ray source (the analyser pass energy was set to 20 eV). The ion bombardment for depth profiling involved a scanning  $\text{Ar}^+$  ion gun, which was operated at an energy of

3 keV. The electrical measurements were based on four-point probe as well as resistivity and Hall-effect measurements that were conducted on  $25 \text{ mm}^2$  squares of film, with Al dots fabricated on the corners using the Van der Pauw technique.



## Chapter 4:

# Parameters of the Al-induced layer exchange process

The investigations presented in this chapter focus on the parameters of the metal-induced Al and Si layer exchange process. They target the question: In what way do which parameters influence the formation of the poly-Si material? Firstly, the time dependent Si grain growth and formation of a poly-Si layer by ALILE is analysed. The subsequent studies concentrate on influences of the layer thickness ratio of the adjacent Al and a-Si films, the annealing temperature, the structure of the polycrystalline Al and the Al/Si interface.

### 4.1 Si grain formation and growth

The default structure to investigate the formation of poly-Si by ALILE was a glass substrate covered by one layer of Al and one layer of a-Si. The layers were of almost equal thicknesses (400 nm Al and 500 nm a-Si). The interaction of these two films was studied in various ways. Firstly, the duration of the annealing time for the crystallization process was varied from 5 min to 60 h at different temperatures. To investigate the interaction of the a-Si and Al layers in the glass/Al/a-Si structure, cross-sections of the samples were prepared and imaged using FIB. Fig. 7 depicts a series of samples before and after annealing at 500°C for 5 min, 10 min, and 60 min. All samples were prepared in the same thermal evaporation and sputtering process to ensure identical conditions prior to annealing. The Al layers in images Fig. 7a and Fig. 7b show slight grey variations within the layer. These variations were caused by the channelling behaviour of the ion beam during imaging. The ions penetrate into the polycrystalline Al to different depths according to the crystallographic orientation of the Al grains, consequently, giving rise to variations in secondary electrons generated. This effect is particularly prevalent in polycrystalline Al

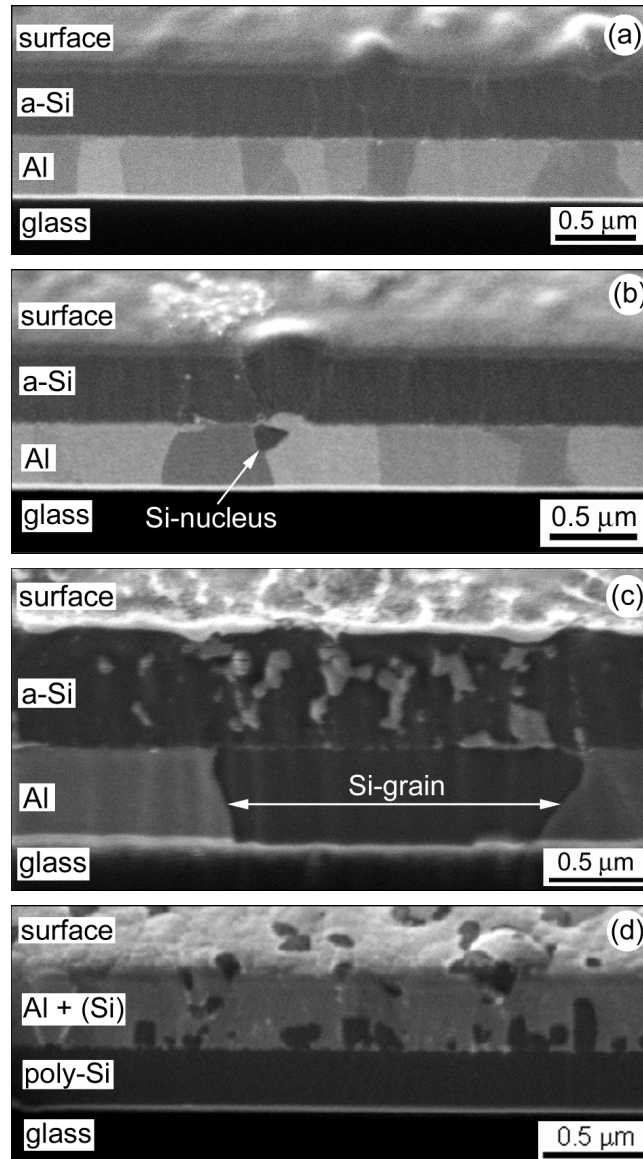


Fig. 7: Cross-section FIB micrographs of a-Si/Al/glass sample of which four individual pieces are shown (a) before annealing, (b) after annealing for 5 min, (c) 10 min and (d) 60 min at 500°C; the sample pieces are tilted by 45°.

[64]. No channelling effects in either poly-Si material or multicrystalline Si wafers could be detected.

Fig. 7a shows the glass/Al/a-Si structure before any heat treatment. During 5 min of annealing a Si-nucleus formed within the Al layer at the Al/a-Si interface, as apparent from Fig. 7b. A preferential nucleation site is where Al-grain boundaries meet the interface due to the greater ease of reducing the free energy at these sites [68]. The material contrast of the FIB was confirmed by EDS investigations. This result on the initial formation of Si nuclei within the Al layer is in agreement with TEM investigations by Konno and Sinclair of Al(6 nm)/Si(6 nm) multilayer systems [46,47]. The cross-section FIB measurements of a

sample annealed for 10 min (Fig. 7c) shows that the Si nuclei grew into the Al layer until they were confined between the Al/a-Si interface and the glass substrate. Sandwiched between these two boundaries the grains continued to grow laterally. The crystal growth terminated when adjacent grains impinged, finally forming a continuous polycrystalline silicon film on the substrate (Fig. 7d). During the poly-Si growth the Al segregated to the top of the sample. Si material, which was not incorporated into the poly-Si layer, formed small Si crystals within the newly evolved Al layer. These crystals are observed as dark areas in the Al layer in Fig. 7d. The overall process during the Si and Al layer interaction leads to an exchange of layer positions leaving the poly-Si film on the glass with the Al layer on top.

Besides FIB microscopy, the nucleation and growth behaviour of the Si grains were studied by employing in-situ optical microscopy in reflection mode. The samples were placed face down onto the heat stage of the microscope. During the annealing at temperatures ranging from 450°C to 525°C the crystal growth could be observed due to the weaker light reflection of the Si material compared to aluminium.

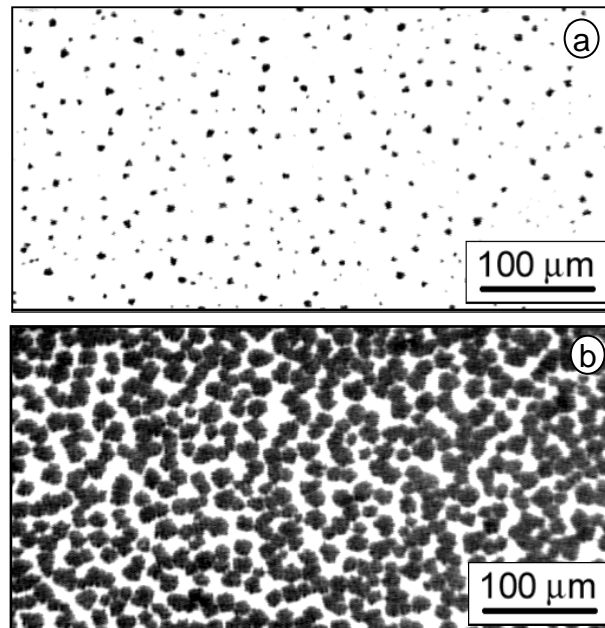


Fig. 8: Optical micrograph of the glass/Al interface taken during the annealing process at 475°C; the dark areas are Si crystals in the highly reflecting Al matrix, which had formed after 31 min (a) and 54 min (b).

Fig. 8 shows two optical micrographs exposing the Si grains as dark areas in the bright Al matrix after annealing for 31 min and 54 min at 475°C. The crystalline nature of the grains was verified by Raman spectroscopy. Whilst in Fig. 8a the Si crystals are still separated, the grains shown in Fig. 8b have started to coalesce and individual grains cannot

easily be distinguished anymore. The advantage of in-situ optical microscopy investigations lies in the opportunity of capturing images in film-like sequences directly during the annealing process. From these sequences the growth of individual grains can be observed and a clear distinction between separate grains and areas of coalesced grains is possible. To study the evolution of the grain size distribution, only images taken before significant coalescence occurred were taken into account. Due to the limited resolution of the microscopy system, grains with a diameter smaller than  $1\ \mu\text{m}$  could not be detected. The images were analysed by using the software package Image Tool (developed by the University of Texas, Health Science Center in San Antonio, Texas). Since the Si grain sizes exceed the layer thickness many times, the grain size distribution can be reduced to a two-dimensional analysis. Fig. 9 shows a series of grain size distributions as extracted from optical images taken after 27 min, 31 min, 38 min, 40 min, 42 min and 44 min during in-situ investigations at  $475^\circ\text{C}$ . The comparison of the graphs in Fig. 9 reveals that the density of small grains dropped significantly over this period of time, although less than 40% of the poly-Si film had formed after 44 min. Because the growth behaviour of the grains could be observed in real time, it became apparent that the grains continued to grow whilst fewer new grains were being formed. This is an indication that the nucleation rate decreases at an early stage of the crystallization process.

The same observation can also be extracted from Fig. 10 showing the crystallized fraction and number of grains versus annealing time. The number of grains within the

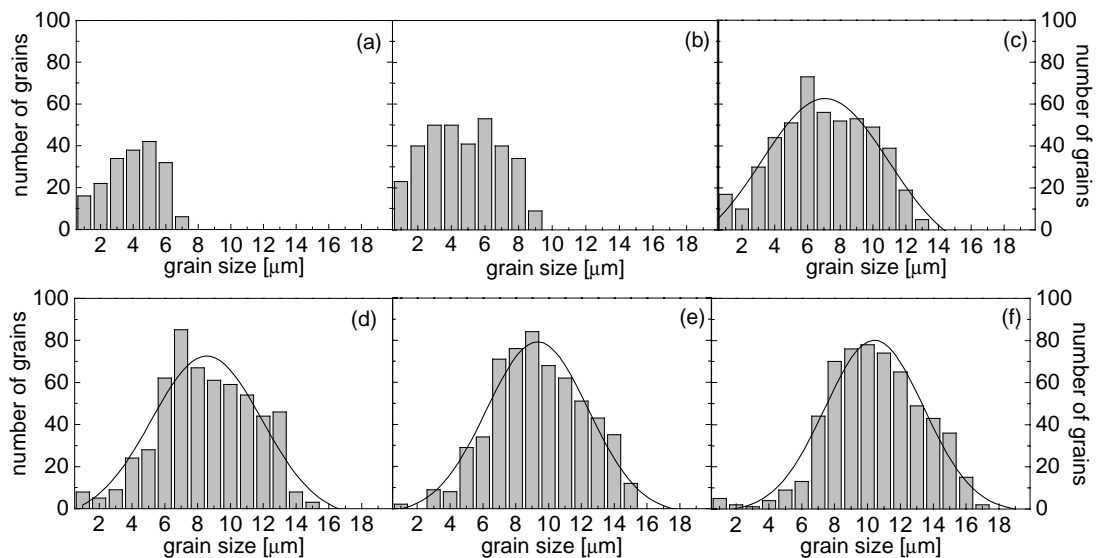


Fig. 9: Grain size distributions extracted from the analysis of optical images taken after (a) 27 min, (b) 31 min, (c) 38 min, (d) 40 min, (e) 42 min and (f) 44 min of annealing at  $475^\circ\text{C}$ . The solid line in (c)-(f) are Gaussian fits to the histograms.

analysed area saturated after about 40 min, even though only 30 % of the poly-Si layer was grown. The analysis was only performed on optical micrographs where the individual grains could still be clearly distinguished from each other. For the particular sample presented here a continuous poly-Si film was formed after 90 min. From Fig. 10 an upper limit for the total number of grains of 600 can be assumed. Considering that the analysed area was  $0.14 \text{ mm}^2$ , it can be concluded that the average grain diameter of the poly-Si layer is  $17 \mu\text{m}$  after full crystallization. It will be shown in chapter 4.3 and 4.5 that the size of the Si grains is sensitive to the temperature and the oxidised Al/a-Si interface, respectively. Since Al grain boundaries appear to provide preferential nucleation sites, the grain size distribution is also dependent on the grain size of the polycrystalline Al layer, which will be discussed in chapter 4.4.

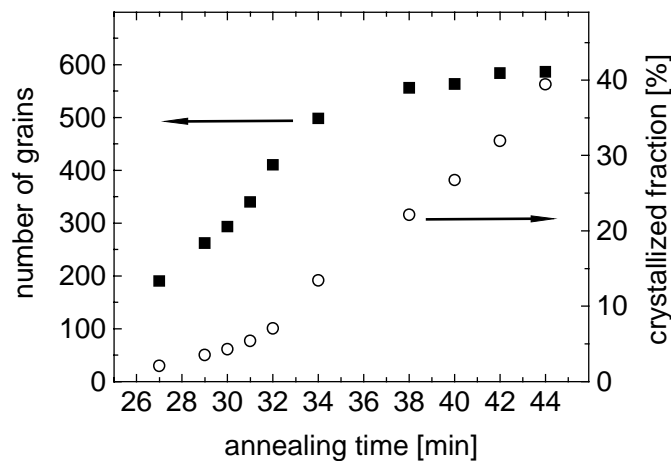


Fig. 10: Crystallized fraction and number of grains versus annealing time determined from a series of optical images where one of them is shown in Fig. 8. The sample was annealed at  $475^\circ\text{C}$ .

The observation that the number of grains saturates at an early stage of the crystallization process enables the determination of the grain growth velocity. In Fig. 9c-d the grain size distributions were analysed using Gaussian distribution functions. The curves are fitted to data taken from optical images where still little impingement had occurred, but the formation of new nuclei was already suppressed. The maxima of the Gaussian curves give the time dependent development of the average grain radius (open circles in Fig. 11). Instead of using a Gaussian fit function for determining the time-dependence of the average grain size, the grain size distribution as such could have been used. However, when the pure numerical average is calculated, grains with a grain diameter of  $1 \mu\text{m}$  have a distorting impact, since  $1 \mu\text{m}$  was the resolution limit of the in-situ optical microscopy system and this data is therefore subject to greater noise. This impact of noise is

diminished with the fit functions. Using the average radius extracted from the Gaussian curves, a linear fit to the data reveals a growth velocity of 4.5 nm/s in the time regime where nucleation is already strongly reduced, but still little impingement occurs.

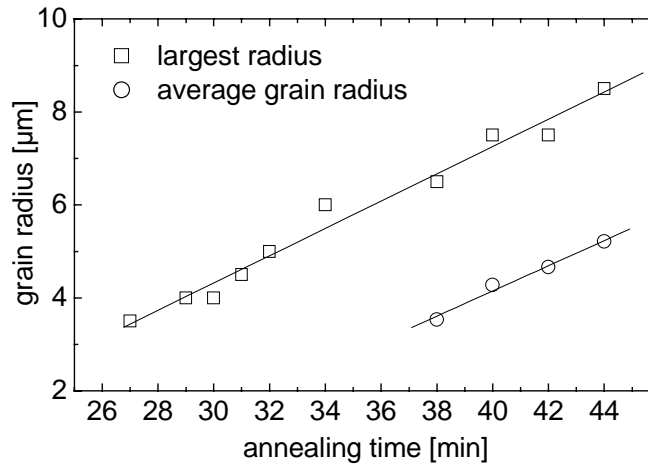


Fig. 11: Time dependence of the radius of the largest grains and the average grain radius according to the mid position of the Gaussian fits in Fig. 9c-f. The solid lines are linear fits to the sets of data.

The grain growth velocity can alternatively be determined from the analysis of the time dependence of the largest grain radii as depicted in Fig. 11 (open squares). The linear fit to this set of data gives a growth velocity of 4.8 nm/s, which is in good agreement with the analysis of the grain size distributions using Gaussian fit functions. Taking the average of the two values, it follows that the crystallization front proceeds into the Al matrix with a velocity of about 4.65 nm/s.

In the optical microscopy analysis presented here, a grain is considered to be an identity that has grown from one nucleation site. However, this optical analysis does not take into account that a grain, although grown from one nucleation site, may contain areas of varying crystallographic orientation due to twinning and faulty dendritic growth, because the growth process of the individual grains is of dendritic nature. Herd et al. have shown that the dendritic growth behaviour of Si crystals is common during metal-induced crystallization for numerous metals that are used to mediate the transformation of a-Si below the eutectic temperature [24]. This dendritic growth is especially prevalent in large grains formed during the Al-induced layer exchange process. These large grains can be achieved by adjusting the whole set of process parameters, which is discussed throughout the following chapters, accordingly. The dendritic growth becomes more distinct the lower the annealing temperature. Fig. 12 shows an optical micrograph of the glass/Al interface with large Si grains embedded in the Al matrix. The dendritic nature is apparent. The

question of what a grain is will be re-addressed in chapter 5.2, when direct grain size measurements are presented and will be compared to the in-situ optical microscopy analysis.

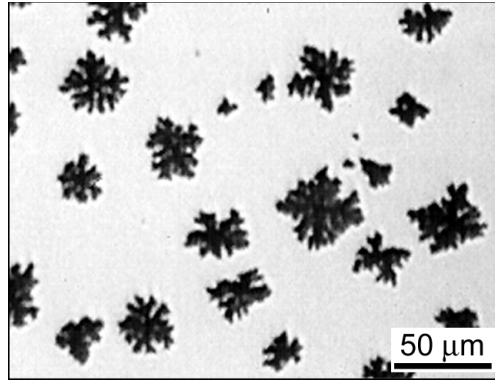


Fig. 12: Optical micrograph depicting the dendritic growth behaviour during ALILE at 425°C.

**Summary:** The Si grains nucleate primarily at the Al/a-Si interface and grow into the Al layer. Once the grains have reached a size similar to the thickness of the Al layer, they continue to grow laterally, constrained normal to the layer structure by the glass substrate and the Al/a-Si interface. At an early stage of the crystallization process, new nucleation is suppressed, which allows areas, growing from one nucleus, to extend laterally up to an average size larger than 10  $\mu\text{m}$  before impingement of neighbouring grains stops the growth. The Al segregates to the top part of the layer structure, and a continuous poly-Si layer is formed on the glass during the course of this layer exchange.

## 4.2 Al and a-Si layer thickness ratio

In the previous section the Si-crystal nucleation and growth was investigated by analyzing a glass/Al (0.4  $\mu\text{m}$ )/a-Si (0.5  $\mu\text{m}$ ) structure. In the following study, the ratio of the layer thicknesses will be varied. The investigation will show that this default structure of almost a 1:1 layer ratio is the most relevant ratio for the analysis of the Al/a-Si layer interaction under steady temperature conditions used in this work. The two possible variations are silicon over- or under-supply, meaning that the a-Si layer is thicker or thinner than the Al layer. Fig. 13a shows a structure where the a-Si layer was three times as thick as the Al layer. During the annealing process at 500°C a continuous poly-Si layer was formed on the glass substrate. This layer was as thick as the original Al film. The surplus

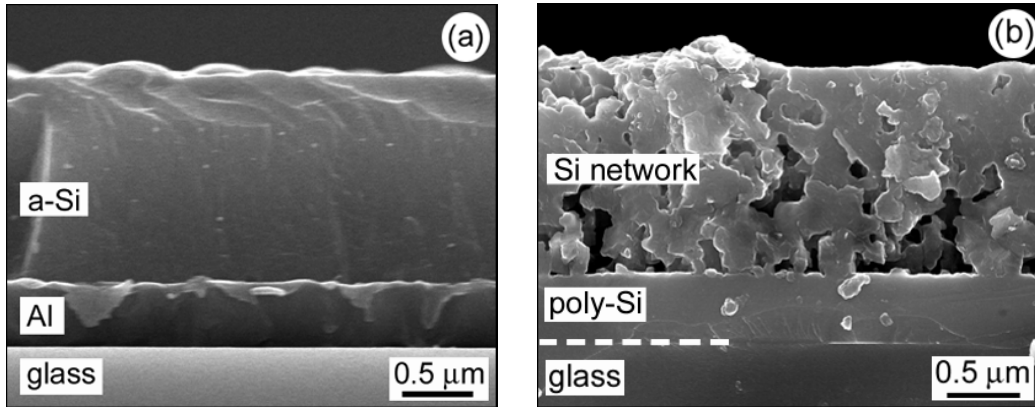


Fig. 13: Cross-section SEM micrographs showing (a) a specimen with a thicker a-Si than the Al layer before heat treatment, (b) the same specimen after crystallization at 500°C and Al etching. The short white dotted line in (b) is a guide to the eye.

of Si material resulted in the formation of a Si network, visible after Al etching as depicted in Fig. 13b. The crystalline nature of the Si network was verified using Raman spectroscopy.

If the Si layer is thinner than the Al layer, scarcity of Si material occurs and therefore no continuous poly-Si film can be formed. However, isolated islands of crystalline silicon grow. These islands have the thickness of the original Al layer and vary in size depending on the Si supply. In Fig. 14 a sample is shown where the initial a-Si layer was only half the thickness of the 0.5 μm thick Al layer. After annealing at 500°C and Al etching, Si islands were visible in SEM studies. Additionally, Si crystals were formed in the top layer and can be seen as protrusions on top of the Si islands. The Si bound in these crystals is lost for Si grain growth within the former Al layer.

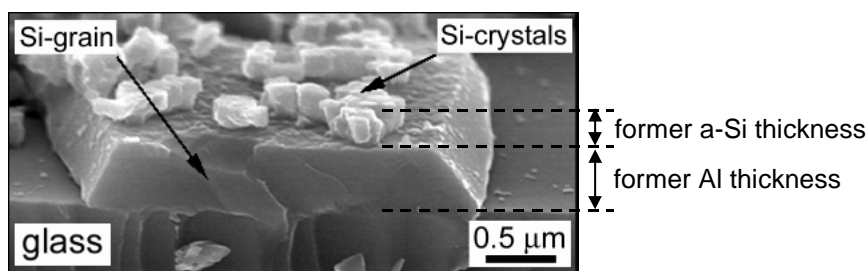


Fig. 14: Cross-section SEM micrograph of a specimen after crystallization at 500°C and Al etching where the original a-Si layer was only half the thickness of the Al layer.

Both cases indicated the importance of the Al/a-Si interface. As highlighted in the previous paragraph, once the Si grains have grown to a thickness equal to that of the Al film, further growth is confined to the space bounded by the substrate and the interface between the two layers. In the case of Si shortage, the original metal layer thickness still

determines the height of the newly formed Si islands, therefore preventing the formation of a continuous poly-Si layer prior to depletion of the silicon. In comparison, a thicker a-Si layer facilitates the formation of a continuous poly-Si layer, but with a thickness also determined by the original Al layer thickness.

Thus, it can be concluded that to form continuous poly-Si films under steady temperature conditions, the a-Si layer must be at least as thick as the Al layer, but that thicker a-Si layers will not give any advantage in the final thickness of the polycrystalline Si layer. A layer ratio of 1:1 therefore seems to be the ideal structure for the formation of a continuous poly-Si film. However, some Si is always not incorporated in the continuous polycrystalline Si film, because it is bound in the form of Si crystallites on the top of the Si film. These crystallites are depicted in the Al+(Si) layer shown in Fig. 7d as well as in Fig. 14. The amount of Si bound in the crystallites seems to vary, and no quantity can be given as yet. A layered structure with a-Si and Al films of similar thickness, with a slight surplus of Si to compensate for the Si lost in the crystallites, is therefore the most relevant structure to study the interaction between a-Si and Al material for the formation of poly-Si thin-films. This type of structure was previously called the default structure.

The relevance of the layer thickness ratio was already recognised by Harris et al. [50]. Their investigation concentrated on a Si and Al layer sequence deposited on oxidised Si substrates. Besides the difference in layer structure, they deposited the Si at 900 °C using CVD for their “thin-Al” films study - Si oversupply. Therefore, they most likely investigated the interaction of  $\mu\text{c-Si}$  with Al instead of a-Si. Harris et al. did not produce continuous poly-Si films during their annealing process. Another study conducted by Allen et al. revealed that the thickness of a Au layer also determines the thickness of Si grains growing within the metal film during the annealing of poly-Si/Au layer structures. [48] This shows the similarities of the interactions in simple eutectic systems during heat activated processes below the eutectic temperatures.

**Summary:** The Si grains grow normal to the layer structure only to a size identical to the thickness of the Al film. Therefore, the maximal thickness of a continuous poly-Si film formed by the aluminium-induced layer exchange is predetermined by the thickness of the metal layer, provided that enough silicon from the a-Si phase is supplied. Si shortage results in the formation of isolated crystalline silicon islands with a thickness according to the original Al layer thickness.

### 4.3 Temperature dependence

This study has so far focused on the general growth pattern of polycrystalline silicon during ALILE. On one hand, this formation is controlled by the diffusion of the silicon atoms from the a-Si material through the Al/a-Si interface into the Al layer, which regulates the supply of material for the poly-Si growth. On the other hand, the diffusion of the Si atoms within the Al layer determines the speed of the grain growth. Besides these two thermally activated diffusion processes, the actual nucleation rate is also dependent on the annealing temperature. The strong influence of the temperature on the overall process is revealed in Fig. 15. The two optical images show two samples, which were prepared using the identical deposition processes, but were annealed at different temperatures. The images were taken in-situ using an optical microscope equipped with a heat stage. The sample in Fig. 15a was annealed for 40 min at 450°C. During this time 164 grains formed within the analysed area with an average size of 9.3  $\mu\text{m}$  covering 10 % of the area. Fig. 15b depicts the second sample, which was annealed at 500°C for 8 min. In this case, 623 grains of average size 3.5  $\mu\text{m}$  were formed, covering about 8 % of the area. This means that at higher temperatures the nucleation rate strongly increases. Due to the high density of nuclei, neighbouring grains impinge quickly during growth and the grain sizes will remain small.

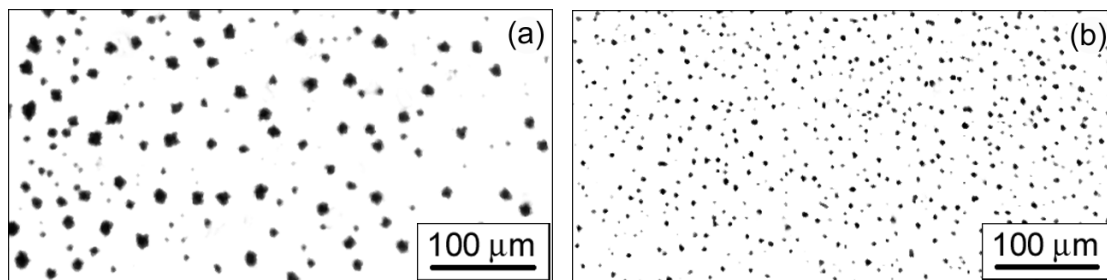


Fig. 15: Optical micrographs of samples deposited under identical conditions but annealed (a) at 450°C for 40 min and (b) at 500°C for 8 min.

To verify the results relating to the temperature dependence of ALILE, SEM channelling investigations were conducted. Fig. 16a and b show samples, deposited under identical conditions, fully crystallized at 375°C and 525°C, respectively. As expected from the results presented above, the sample annealed at the lower temperature contained significantly larger grains than the sample treated at 525°C. Although, the nucleation rate as well as the grain growth velocity are reduced by lowering the annealing temperature, it

seems that the formation of new nuclei decreases more strongly with decreasing temperature than the grain growth. In other words, the Si grains grow more slowly at lower temperatures, but, nevertheless, they have more space within the Al matrix with respect to neighbouring grains due to the significantly lower grain density. Therefore, to process large-grained poly-Si by using ALILE, lower temperatures are favourable. The trade-off is the slower crystallization process.

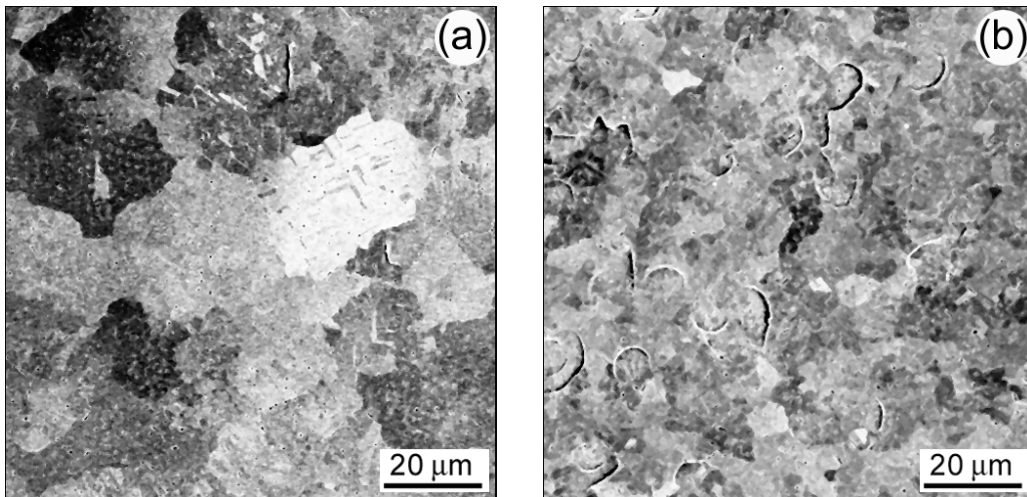


Fig. 16: Electron channelling SEM images of former glass/poly-Si interfaces of fully crystallized samples annealed at (a) 375°C and (b) 525°C.

Besides Si grains with various crystallographic orientations, the SEM images of Fig. 16, show additional features with regard to crystallographic quality. Firstly, crystallographic faults in the structure of individual grains manifest themselves as streaks contrasting to the surrounding grain, as shown in Fig. 16a. Secondly, little black dots ( $\sim 1\mu\text{m}$ ) can be seen. These dots stem from Al clusters that were trapped between the poly-Si film and the glass before the layer was lifted off the substrate, and will be analysed in detail in chapter 5.1. Furthermore, prominent dark lines are part of both images, but more numerous in Fig. 16b. They are attributed to cracks in the film, which occur during the process of lifting the poly-Si layer off the glass, turning it over, and transferring it to a metal substrate. The cracks cannot be easily avoided during the preparation.

**Summary:** The lateral extension of the grains of the poly-Si films is larger, the lower the annealing temperature during the layer exchange process. Although the nucleation rate as well as the grain growth velocity decreases with lower temperature, the nucleation rate is reduced more strongly. This significant decrease of nuclei formation is the requirement that the Si grains can grow to larger sizes at lower temperatures before impingement of neighbouring grains

occurs. Although large Si grains are desirable for the subsequent device fabrication, the time needed to form a continuous poly-Si layer increases drastically at lower processing temperatures.

## 4.4 Influence of the polycrystalline Al

Fig. 17a and b show a comparison of two 400 nm thick Al films evaporated at deposition rates of 1-2 nm/s and 7-8 nm/s, respectively. Since the ions of the FIB microscope penetrate to different depths according to the crystallographic orientation of the Al grains, the resulting ion channelling contrast highlights the varying grain size within the material. It is apparent from the micrographs that the Al film deposited using the slower rate consisted of grains typically 100 nm or less in size (small-grained Al, Fig. 17a), whilst the higher deposition rate lead to films of grains typically between 100 and 500 nm (large-grained Al, Fig. 17b), and therefore in the range of the total layer thickness. Graper has studied the Al grain size of 1  $\mu\text{m}$  thick Al films deposited by electron beam evaporation [69]. He showed that the grain size of the polycrystalline Al material depends on the evaporation rate as well as the substrate temperature. The observation that the grain size of thermally evaporated Al becomes larger as the deposition rate is increased is in good agreement with Graper's results.

Both samples were stored in air after the Al deposition for 24 hours, followed by the sputtering deposition of a 500 nm thick a-Si layer. The two samples were annealed together for 40 min at 425°C. The results presented are exemplary for investigations

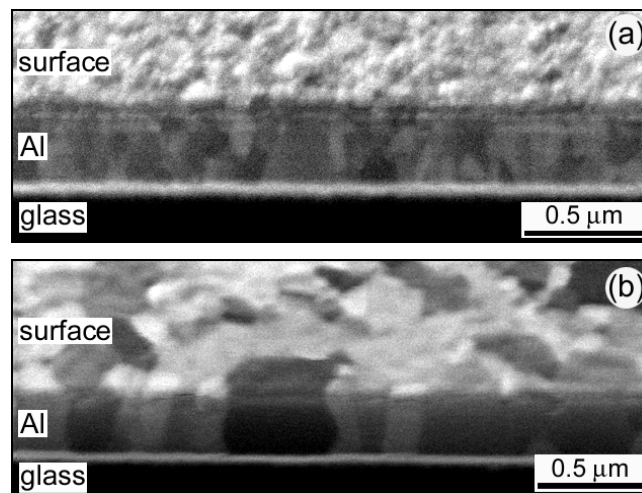


Fig. 17: Cross-sectional FIB micrographs of thermally evaporated Al on glass substrates deposited at rates of (a) 1-2 nm/s and (b) 7-8 nm/s; the samples are tilted by about 45°.

conducted at different temperatures ranging from 350°C to 500°C and varying annealing times. Fig. 18 shows optical micrographs of the glass/film interfaces after annealing. Due to the different reflective of Al and Si, the dark Si-grains are clearly visible in the highly reflecting Al matrix. The crystalline character of the Si grains was verified by Raman-spectroscopy showing the typical crystalline silicon response (see chapter 2.2). Since the Si grains grow within the Al layer and the thickness of this layer is small compared to evolving Si grain sizes of several microns, the present comparative study on how the polycrystalline Al structure influences the Si nucleation and grain growth can be reduced to a two-dimensional analysis. This reduction has already been applied in chapter 4.1. The analysis of Fig. 18a reveals that during the annealing process, crystalline Si grains have developed with a nucleation density of  $7 \times 10^3 \text{ mm}^{-2}$  occupying about 7% of the original small-grained Al layer. In contrast, Fig. 18b shows that the Si nucleation density in the large-grained Al layer is only  $2 \times 10^3 \text{ mm}^{-2}$  and the Si grains occupy 0.5% of the metal film. It should be noted that the imaging system used to study the nucleation density limits the resolution to about 1  $\mu\text{m}$ , consequently, all grains of sizes smaller than this limit are not considered in the analysis.

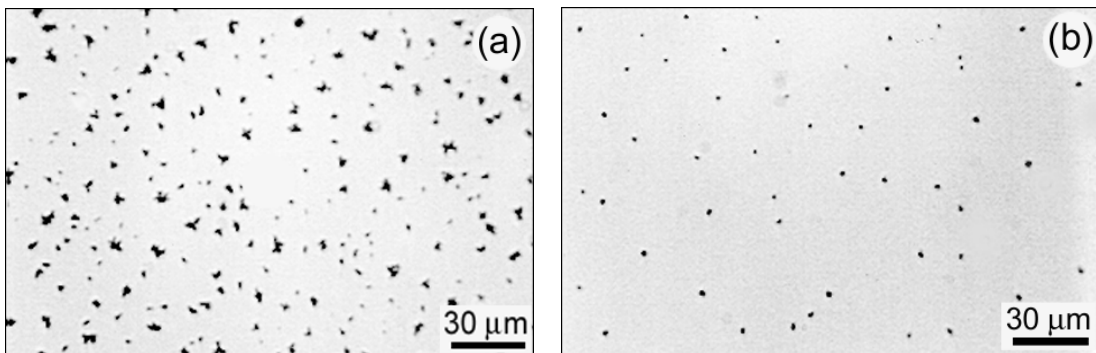


Fig. 18: Optical micrographs of the glass/Al interface of two samples after annealing at 425 °C for 40 min. The samples consisted of (a) a glass/small-grained Al/a-Si structure and (b) a glass/large-grained Al/a-Si structure. The dark areas are Si crystals in the reflective Al matrix.

In Fig. 18a the area covered by Si grains is about 10 times larger than the covered area in Fig. 18b. Additionally, at this stage of the crystallization process, the average size of the detectable Si grains of the sample with the small-grained Al structure is more than double the diameter of the Si grains formed in the large-grained Al film, according to the image analysis. However, the final poly-Si film consists of larger Si grains when grown within a large-grained Al film due to a low density of nuclei. The lower nucleation rate allows the grains to grow larger before impingement of neighbouring grains occurs. From the observations presented, it becomes apparent that the crystallization process is faster when

the polycrystalline Al film consists of material with smaller grains. This enhanced process velocity can be understood in terms of an increased diffusion of Si solute along Al grain boundaries [70]. The augmented nucleation rate will be discussed in chapter 6.3.

**Summary:** The size of the Al grains in the polycrystalline Al layer influences the speed of the crystallization process as well as the grain size of the final poly-Si film. The layer exchange process is faster the smaller the polycrystalline grain structure of the Al film. There is an increased nucleation rate in small-grained Al. Due to the higher density of nuclei, the grain growth is constrained sooner by neighbouring grains and the final Si grain sizes are smaller when the Al layer, which induces the crystallization, consists of smaller grains.

## 4.5 The Al/Si interface layer

In this study on the parameters of the aluminium-induced layer exchange process, the role of the Al/a-Si interface on the overall crystallization process has not yet been considered. Since the vacuum was broken between the Al and a-Si depositions, the interfaces initially consisted either of a naturally formed Al or Si oxide layer, depending on the layer sequence. The influence of this interface layer was investigated with microscopical techniques as well as x-ray photoelectron spectroscopy.

### 4.5.1 Microscopical investigations

The analysis of the influence of an oxide interface layer initially concentrates on the Al oxide interface layer of a substrate/Al/a-Si structure. The formation of this oxide is due to the high reactivity of aluminium with oxygen, and is inevitable during the sample transfer from the evaporator to the sputtering system. The thickness of this Al oxide interface can be easily influenced by varying the time that elapses between the deposition of the Al layer and the a-Si. The increase of the natural Al oxide layer on evaporated Al during extended exposure time to ambient air was verified using ellipsometry measurements. For example, the thickness of an Al oxide layer gradually increased by about 1 nm within 48 h when exposed to air after thermal evaporation. The first measurement was taken 3 min after unloading the Al film from the deposition chamber. However, the possibility that increased contamination during extended storage time between sequential depositions has an influence on the crystallization process in addition to the increased Al oxide layer cannot

be entirely excluded. The effect of the interface layer on Si grain growth and therefore grain size could be studied using optical microscopy in a similar way as in previous chapters. By taking advantage of the different reflectivities of Si and Al, the glass/film interface revealed the varying Si growth behaviour within the highly reflective Al matrix.

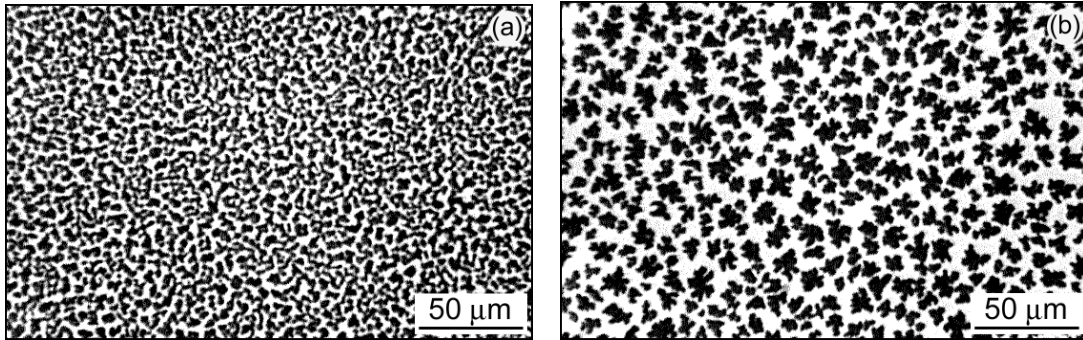


Fig. 19: Optical micrographs of the glass/Al interface of two samples after annealing at 475°C for 30 min. The initial structure was glass/Al/a-Si. The exposure time of the Al layer to air prior to the a-Si sputtering deposition was (a) 3 min and (b) 48 h.

Fig. 19 shows the optical images of two samples that were prepared under identical conditions and annealed at 475°C for 30 min. The only difference was that the sample shown in Fig. 19a was loaded into the sputtering system within 3 min after Al evaporation, whilst the one exhibited in Fig. 19b was exposed to air for 48 h prior to the sputtering deposition. The comparison of these two samples after annealing indicates that a thicker Al oxide interface layer, due to the time delay during the subsequent depositions, results in a lower number of Si grains per unit area, leading to the growth of large, still mainly isolated grains (Fig. 19b). On the other hand, a thinner Al oxide layer, due to immediate sample transfer between the depositions, results in a Si network formed by a greater number of small Si grains (Fig. 19a). Additionally, the Al oxide interface layer slowed down the crystallization process, since only 46 % of the film in Fig. 19b was crystallized compared to 61 % in Fig. 19a, as estimated from image processing analysis.

Other pieces of the same samples, of which parts had been annealed for the investigations shown in Fig. 19, were annealed at 475°C for 2 h to ensure the complete crystallization of the poly-Si film regardless of the Al-oxide layer at the interface. The SEM electron channelling investigations of the former glass/poly-Si interface of these pieces, shown in Fig. 20, revealed that the sample with the enhanced native Al oxide layer consisted of significantly larger grains than the sample immediately transferred to the sputtering system. These observations are expected from the optical micrographs of Fig. 19, since the reduced nucleation rate caused by the enhanced Al oxide interface layer

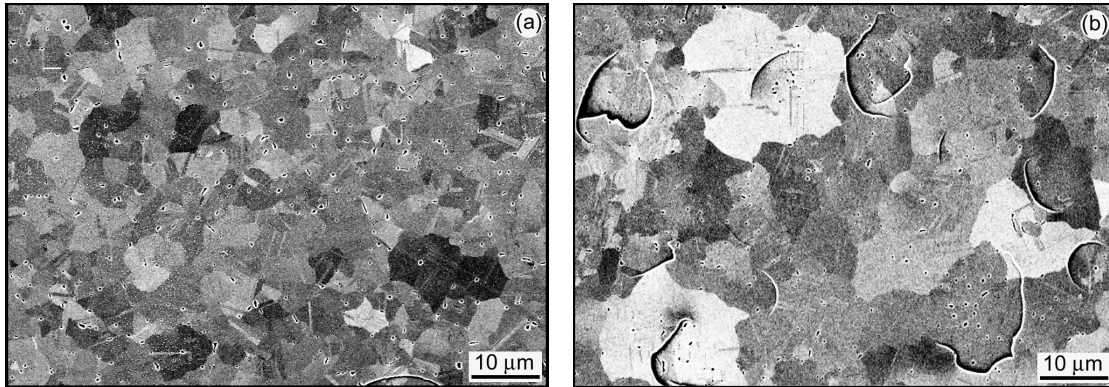


Fig. 20: Electron channelling SEM images of former glass/poly-Si interfaces of fully crystallized samples annealed at 475°C for 2 h. The initial structure was glass/Al/a-Si. The exposure time of the Al layer to air prior to the a-Si sputtering deposition was, as in Fig. 19, (a) 3 min and (b) 48 h.

enables the Si grains to grow to a larger size before impingement of neighbouring grains occurs. The micrographs of Fig. 20 show, besides the polycrystalline nature of the Si films, prominent dark lines in both samples. These lines are due to cracks in the film and have been mentioned previously during the discussion of Fig. 16 in chapter 4.3. Additional features in the form of small black dots of about 1 μm in diameter in the images are the subject of chapter 5.1.

The present investigation, thus far, has given evidence of the significance of the polycrystalline Al structure, as well as the important role of the naturally grown Al oxide interface layer that is inevitably formed during sample transfer. However, it has not yet been determined, which of the two parameters has greater dominance on the overall layer exchange when competing with each other. To investigate this issue, two samples were prepared with the following layer sequences: (i) Glass/large-grained-Al/a-Si/small-grained-Al and (ii) glass/small-grained-Al/a-Si/large-grained-Al as shown in Fig. 21a and b. The large-grained and small-grained structures of the polycrystalline Al layers were achieved by using different thermal evaporation rates according to the results presented in chapter 4.4. The lower Al/a-Si and the upper a-Si/Al interfaces contain an Al oxide and a Si oxide, respectively. Both structures were annealed at 475°C for 60 min to induce the crystallization process of the sandwiched amorphous Si layer. From the results discussed in chapter 4.4, one would expect that the poly-Si film forms within the small-grained Al layer (sg-Al), since the speed of the crystallization process is faster in sg-Al than in the large-grained Al layer (lg-Al). This hypothesis is valid for the sample shown in Fig. 21a and c before and after annealing, because the poly-Si layer has replaced the sg-Al. However, even in the case of the glass/sg-Al/a-Si/lg-Al structure the poly-Si layer has formed within

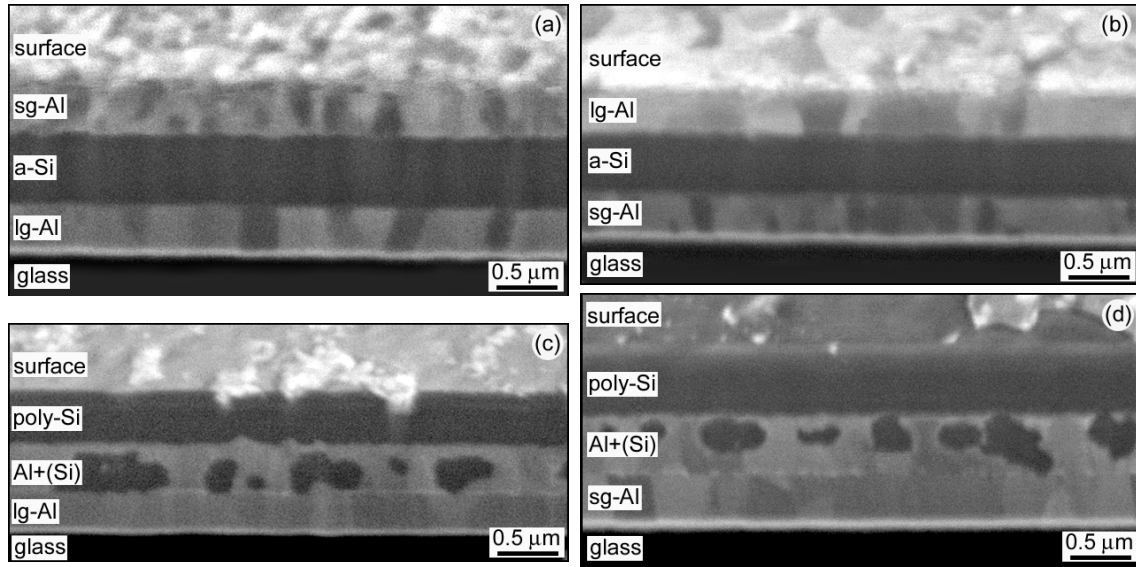


Fig. 21: Cross-sectional FIB micrographs of a glass/large-grained-Al/a-Si/small-grained-Al sample (a) before and (c) after annealing, and a glass/small-grained-Al/a-Si/large-grained-Al structure (b) before and (d) after annealing. The annealing process was carried out at 475°C for 60 min. The bright line between the poly-Si layer and the glass substrate is an FIB artefact. The samples are tilted by about 45°.

and replaced the top Al layer, which in this sample is the large-grained Al film. In both case, the Al and Si interdiffusion occurs through the a-Si/Al interface consisting of a Si oxide rather than through the Al oxide of the Al/a-Si interface. This observation indicates that the oxidisation state of the interface plays a dominating role in the overall crystallization when the two parameters are in competition, because the influence of the interface on the layer exchange process counteracts and overcompensates for the influence of the polycrystalline Al structure.

Before summarising the results presented in this chapter, it has to be mentioned that the top poly-Si layers in Fig. 21c and d are covered by a thin Al/Al oxide layer of which only patches are still visible in the images. The larger fraction of this thin surface layer is removed by the Ga<sup>+</sup> beam of the FIB during image recording.

**Summary:** The oxide interface controls the velocity of the crystallization process. The longer the first layer is exposed to air prior to the deposition of the second layer, the slower the layer exchange process. Differences in the composition of the initial interface oxide, i.e. initially Si oxide or Al oxide, dominate the layer exchange process when competing with the influence of the Al grain structure. The Si and Al interaction through a Si oxide interface seems to be facilitated compared to the interaction through an Al oxide interface.

## 4.5.2 XPS measurements

In the last chapter it was shown that an oxide interface layer between the Al and a-Si film has significant impact on the crystallization process. This chapter addresses what happens to this interface layer during the layer exchange process and what the interface consists of after the formation of the poly-Si film. To investigate these issues, glass/Al/a-Si and glass/a-Si/Al structures were prepared. The thickness of the Al and a-Si layers were 100 nm and 140 nm, respectively. The a-Si layer was chosen to be thicker to ensure that enough silicon was supplied to form a continuous poly-Si layer of equal thickness to the initial Al layer that was replaced (see chapter 4.2). The samples were analysed before and after annealing using x-ray photoelectron spectroscopy. The XPS depth profile analysis focused on the Al  $2p$ , the Si  $2p$  and O  $1s$  core level regions. The metallic Al  $2p$  peak and the Al bulk plasmon peak at binding energies of 73.0 eV and 88.4 eV binding energy, respectively, were used to charge correct the spectra [71]. No atomic compositional ratios of Si, Al, and O were extracted because of the difficulty in the depth profile analysis that arises from the different Ar<sup>+</sup> sputtering yield of Al and Si. The sputtering yield for Al is significantly higher than for silicon, e.g. more than double at an ion energy of 500 eV [72]. Since the Al layer contains clusters of crystallized Si, Ar<sup>+</sup> sputtering leads to an inhomogeneous removal of material. A layer by layer atomic compositional depth profile would therefore be strongly distorted. Consequently, the discussion concentrates on the qualitative analysis of XPS measurements in conjunction with FIB cross sectional micrographs.

Firstly, a glass/Al/Al oxide/a-Si structure before annealing was investigated. The Al oxide layer had inevitably formed during the exposure of the Al layer to air for 24 h. This initial structure is schematically sketched in Fig. 22a. To investigate the original structure, XPS depth profiles of the Al  $2p$ , the Si  $2p$  and O  $1s$  regions were taken from the sample. Only the Al  $2p$  region is shown in Fig. 22b. Each level displays the spectrum taken after sequential Ar<sup>+</sup> etching for 40 s. The levels exhibited represent the parts of the entire surface-to-glass depth profile that concern the chemistry of the interface between the Al and a-Si layer. The metallic Al  $2p$  peak at 73.0 eV (marked with Al<sup>m</sup>) exhibited a clear side peak at the higher binding energy of  $75.3 \pm 0.2$  eV (marked with Al<sup>ox</sup>) when the XPS spectra of the depth profile coincided with the interface. The measured chemical shift of 2.3 eV indicated the presence of an Al oxide layer [71]. The position of the interface could be determined from the sudden decrease of the Si intensity in conjunction with the steep

increase of the metallic Al at around level 62. At this level the oxygen depth profile reached an intensity maximum. The maximum of the oxygen signal combined with the increased  $\text{Al}^{\text{ox}}$  signal at the interface verified the existence of the naturally formed Al oxide layer at the Al/a-Si interface.

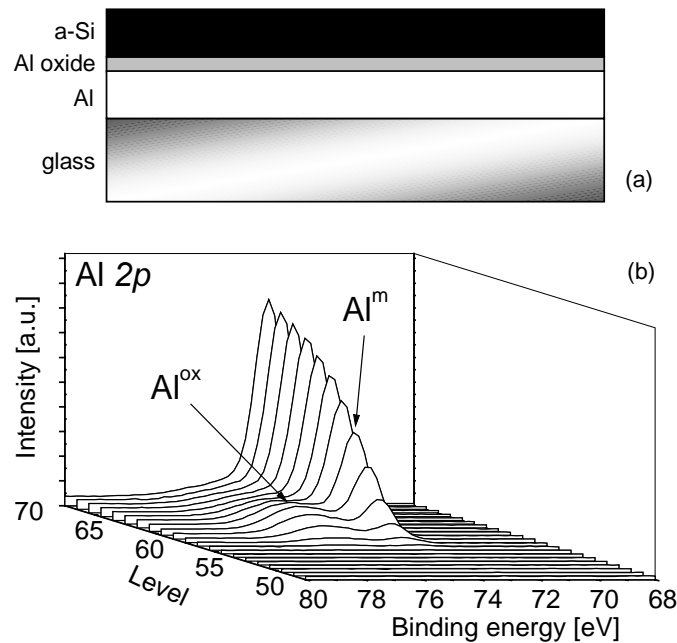


Fig. 22: Schematic diagram of the original glass/Al/Al oxide/a-Si structure (a) and (b) XPS depth profile of the Al 2p core level region.  $\text{Al}^{\text{ox}}$  and  $\text{Al}^{\text{m}}$  mark the binding energies of the oxygen-bonded and metallic aluminium, respectively. The levels displayed focus on the interface chemistry between the Al and a-Si layers.

This initial glass/Al/Al oxide/a-Si structure was subsequently annealed at 425°C for 3 h. During the annealing process the layers exchanged position and a continuous poly-Si layer was formed on the glass substrate whilst the Al segregated to the top as described in chapter 4.1. Fig. 23a shows a cross-sectional FIB image of the annealed sample. The residual Si not needed for the poly-Si layer formation is incorporated in the Al+(Si) layer as apparent from the dark areas within the bright Al matrix. The XPS depth profiles shown in Fig. 23b-d correspond to the sample of Fig. 23a. Following the analysis above, each level, i.e. set of spectra of the Al 2p, Si 2p, and O 1s binding energy regions, was taken after sequential  $\text{Ar}^+$  etching for 40 s. As in Fig. 22, the parts of the depth profiles displayed focus on the chemistry of the interface between the poly-Si film and the top Al+(Si) layer. In Fig. 23b the metallic Al peak at 73.0 eV and the oxygen-bonded Al at 75.3 eV are marked. Fig. 23c and d show the O 1s peak at  $532.6 \text{ eV} \pm 0.2 \text{ eV}$  and the Si 2p peak at  $99.4 \pm 0.1 \text{ eV}$ , respectively. Although the FIB image of Fig. 23a reveals a well-defined interface between the poly-Si and the Al+(Si) film, the XPS depth profiles exhibit a gradual

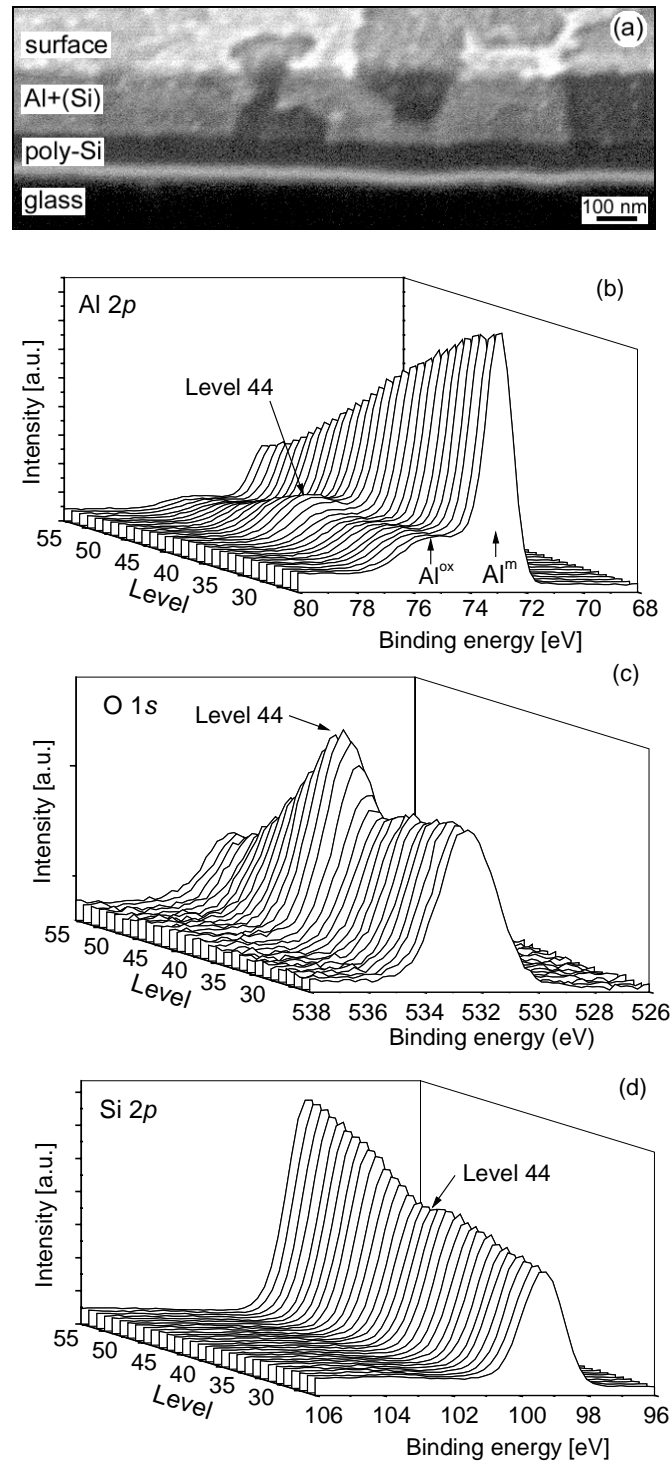


Fig. 23: Analysis of an initial glass/Al/a-Si structure after annealing and the layer exchange process: (a) Cross-sectional FIB micrograph and (b-d) depth profiles of the XPS spectra.

transition. This underlines the distortion effect inherent to the depth profile investigations due to the strong difference in sputtering yield of the materials as mentioned above.

Nevertheless, the comparative analysis of the three depth profiles reveals that the intensities of the Al<sup>ox</sup> and the O 1s peak have a local maximum at level 44, whilst the Si 2p peak has a local minimum at almost the same level (level 43). The coincidence of the three

extrema is a strong indication of the existence of an Al oxide interface layer between the poly-Si and Al+(Si) layer after crystallization. Additionally, the top Al layer was etched off the sample. The bar poly-Si film was again investigated using XPS. On the surface of the Si film, Al oxide was again detected by analysing the binding energy shift of oxygen-bonded aluminium. This means that the Al oxide remains on the surface of the poly-Si film even after Al etching.

To complement the measurements on samples before and after full crystallisation, XPS depth profile investigations were conducted on a glass/Al/a-Si sample that was only partially crystallized (75 % according to optical micrograph analysis). The results concerning the chemistry of the interface layer also revealed the existence of an Al oxide interface layer. Consequently, the XPS measurements give evidence that an Al oxide layer exists at the interface of the original, the partially annealed and the fully annealed layer structure. This means that the naturally formed Al oxide film between the initially deposited Al and a-Si layer sequence remains stable throughout the entire crystallization process. A stable interface oxide seems surprising considering that during the formation of the continuous poly-Si layer the Al and Si films exchange positions completely – not a single atom of either layer remains where it was. The Al oxide interface layer is most likely not an entirely stoichiometric  $\text{Al}_2\text{O}_3$  layer, because the Al  $2p$  binding energy shift is 2.3 eV compared to 2.7 eV in bulk  $\text{Al}_2\text{O}_3$ . This value resembles the data reported by Flodstrom et al. on their in-situ XPS observations of the initial growth of thin non-stoichiometric Al oxide layers on polycrystalline Al [71].

For the structure so far investigated using XPS, the Al was deposited prior to the a-Si, but in the previous chapter it was shown that a layer exchange also occurs when the a-Si is buried under an Al film. Initially the a-Si/Al interface of a glass/a-Si/Al structure consists of an naturally formed  $\text{SiO}_2$ , because the silicon is exposed to air prior to the Al deposition. The role of the interface oxide in this structure is also analysed using XPS. Fig. 24a shows the FIB cross-sectional micrograph of such an inverse layer sequence, compared to the one investigated previously, after annealing. During the 3 hour annealing process at  $425^\circ\text{C}$  a continuous poly-Si layer had formed replacing the top Al layer. The Al was repelled from the growing crystalline Si phase and segregated to the glass substrate. There, it formed an Al+(Si) layer with the residual Si that was not incorporated in the continuous poly-Si layer. The XPS depth profile analysis of this sample is shown in Fig. 24b-d. As discussed for Fig. 23 the levels presented do not constitute the entire surface-to-glass profile but concentrate on the chemistry of the Al/Si interface. From Fig. 24c it is apparent that the O  $1s$  peak

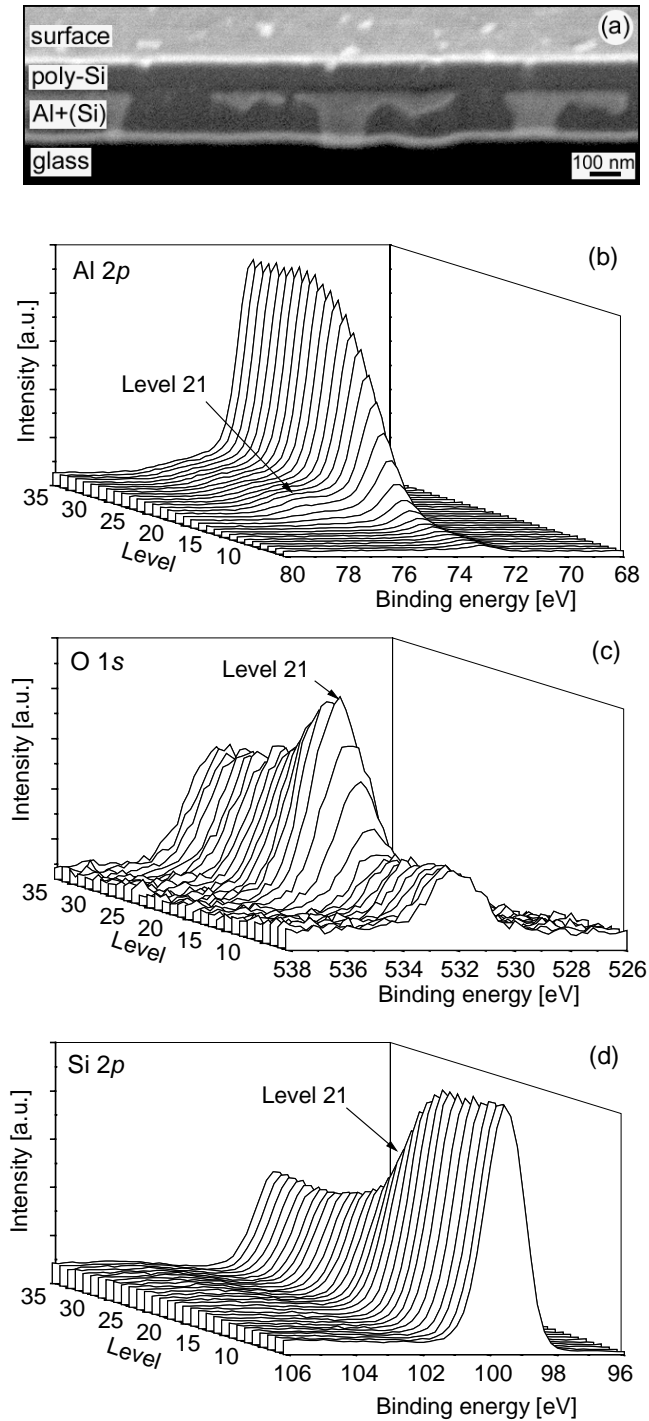


Fig. 24: Analysis of an initial glass/a-Si/Al structure after annealing and the layer exchange process: (a) Cross-sectional FIB micrograph and (b-d) depth profiles of the XPS spectra.

measured at  $532.3 \text{ eV} \pm 0.2 \text{ eV}$  has a maximum at level 21. At this level the corresponding  $\text{Al}^{\text{ox}}$  intensity at  $75.3 \text{ eV}$  has almost increased to its maximum, which is at level 25 (Fig. 24b). However in this sample the maximum of the  $\text{Al}^{\text{ox}}$  intensity is not as prevalent as in Fig. 23b and no local extremum could be detected on the Si depth profile.

It is worthwhile noting that neither of the Si  $2p$  depth profiles shown in Fig. 23d and Fig. 24d give any evidence for the formation of Si oxide, which would be manifested in the

form of a chemical shift of the Si  $2p$  core level to a binding energy in the region of  $103 \text{ eV} \pm 2 \text{ eV}$  [73]. Oxidised silicon was not found to reduce significantly under  $\text{Ar}^+$  ion bombardment. The increased oxygen content at the interface as apparent from Fig. 24c can therefore be attributed to an Al oxide layer. Thus, the glass/Al+(Si)/poly-Si structure of Fig. 24a also contains an Al oxide interface film between the two layers, very similar to the inverse structure analysed in Fig. 23.

The comparison of the O  $1s$  depth profiles shown in Fig. 23c and Fig. 24c indicates that in both cases the oxygen content is higher in the Al+(Si) film than in the pure poly-Si film. This is in contrast to the initial structures where a higher concentration of oxygen in the sputtered a-Si than in the evaporated Al layer was detected. In chapter 4.1 it was shown that the poly-Si grows within the Al whilst the Al is repelled from the growing crystalline Si phase and segregates into the initial a-Si film. The lower oxygen content in the poly-Si layer than in the Al+(Si) after crystallization can therefore be attributed to the gettering properties of Al when the a-Si film dissociates into the metal [74]. The ability of Al to bind oxygen can be seen as an additional advantage in the formation of continuous high-quality poly-Si using aluminium-induced crystallization. However, detailed investigations of the variations in oxygen concentration in the films using, for example, secondary ion mass spectroscopy have not been conducted in the work presented.

**Summary:** The oxide interface between the adjacent Al and Si layer seems to remain at the interface throughout the entire layer exchange process, although most of the Si and Al atoms change position from one side of the interface to the other. The interface consists of an overall stable Al oxide. However, this oxide layer should not be considered as a homogenous film but rather a film with local variations in the structure so that an exchange process can occur in the first place (see chapter 6.1).

### 4.5.3 No interface oxide

In the previous two chapters, the existence of a stable interface oxide between the Al and Si layer was shown. This interface oxide layer remains at its original position throughout the entire layer exchange. Is this oxidised interface mandatory for the exchange process? This question can be answered by studying the interaction of adjacent a-Si and Al films when deposited in the one vacuum system.

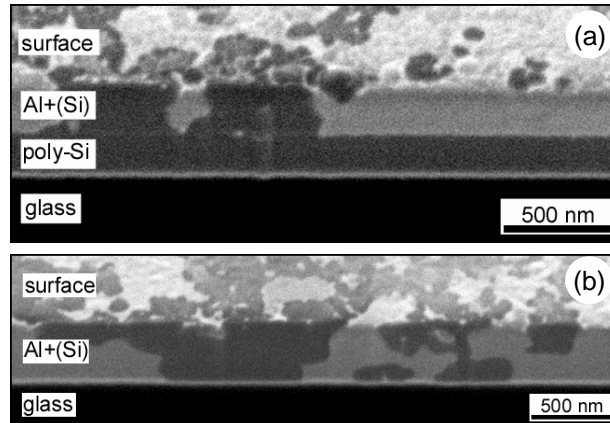


Fig. 25: FIB images of glass/Al/a-Si structure after annealing for 2 h at 450°C. (a) The sample was exposed to air for 2 h between the layer depositions and (b) the sample was transferred in vacuum from one deposition chamber to the next.

The vacuum system used was equipped with an electron beam evaporator and a dc magnetron sputtering chamber. The samples were loaded via a load lock system and transferred from one deposition chamber to the next using a transfer system at a pressure of  $2 \times 10^{-5}$  Pa within 2 min. In this combined system glass/Al (~200 nm)/a-Si (~250 nm) structures were prepared. For the use of comparison, another set of samples was fabricated under identical deposition conditions. However, these samples were exposed to air for 2 h between both depositions.

Fig. 25 shows FIB images of two samples prepared with and without any vacuum break between the depositions after annealing for 2 h at 450°C. The layers of the sample with an interface oxide have exchanged position and a continuous poly-Si film has formed on top

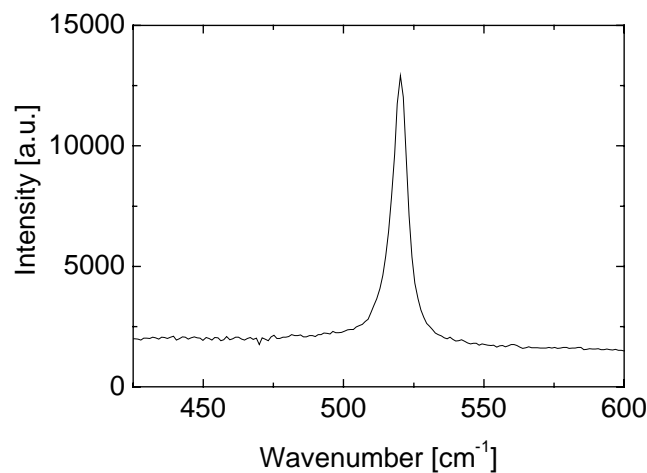


Fig. 26: Raman spectrum of the sample shown in Fig. 25b. The signal is noisy due to the surface consisting of Si grains and Al.

of the glass substrate as expected from the results presented in the previous chapters. However, in the sample where the Al layer was immediately transferred into the sputtering chamber without breaking the vacuum no such layer exchange has occurred. Although the Si has crystallized according to Raman spectroscopy shown in Fig. 26, it has not formed a continuous film. The Si network, the dark areas in Fig. 25b, is embedded in an Al matrix.

**Summary:** The interface oxide seems to be necessary for the layer exchange process. If this interface is free of any oxide, the Al still induces crystallization of the amorphous Si, but no continuous poly-Si layer is formed, and no exchange of the Al and Si films occurs.



# Chapter 5:

## Characterisation of the poly-Si films on glass

The previous chapters have shown that a continuous polycrystalline silicon layer can be formed on glass substrates by an aluminium-induced layer exchange process at low temperatures. However, this poly-Si material has, as yet, not been characterised in detail. Probably one of the first questions that comes to mind concerning the nature of the material is its Al content after crystallization seeing as the Si grains grow within the Al medium. The grain structure of the poly-Si film and its electrical properties are of similar importance for subsequent thin-film device fabrication as the metal content. All three characteristics of the polycrystalline material will be analysed in the following chapters.

### 5.1 The Al content

For the analysis of the Al content in the poly-Si, the Si film as well as the entire substrate/poly-Si structure is investigated after Al-induced crystallization. Aluminium is incorporated into the substrate/film system in various forms. The first form that will be discussed is Al clusters which can be detected at the glass/poly-Si interface, as apparent from the FIB image shown in Fig. 27. These clusters consist of Al, which cannot segregate to the top Al layer during the annealing process, because the continuous poly-Si film acts as a diffusion barrier.

The clusters can be found at the glass/Si grain interface and at the triple-junctions where Si grain boundaries intersect the substrate. These two types of clusters will be called intra- and inter-grain clusters, respectively. Inter-grain Al clusters at Si grain boundaries of fully crystallized films appear to develop when adjacent impinging grains grow faster along the Si/Al interface. Once two neighbouring grains have coalesced, they form a barrier before

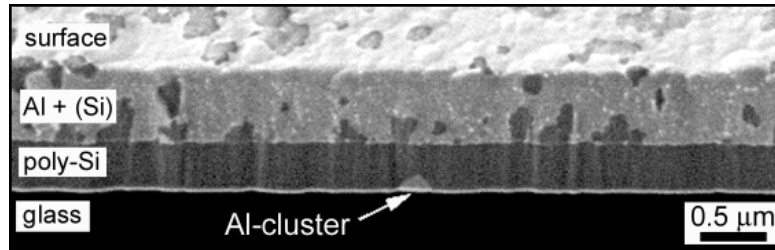


Fig. 27: Cross-section FIB micrograph of a glass/poly-Si/Al structure after full crystallization showing an Al cluster trapped at the glass/poly-Si film interface.

all Al can diffuse to the evolving top Al layer. The blocked Al remains as inter-grain Al clusters at Si grain boundaries between the poly-Si film and the glass substrate.

Intra-grain Al clusters occur predominantly in larger grains ( $> 5 \mu\text{m}$ ), due to their strong dendritic growth pattern, as shown in Fig. 12 of chapter 4.1. Whenever dendrites of one grain grow slightly faster in the vicinity of the metal/Si interface, and finally form a large crystalline Si grain, aluminium is trapped in the form of clusters at the substrate/Si grain interface. The crystalline structure of the grain prevents the Al atoms of the cluster from interdiffusing with the Si atoms of the a-Si top layer.

Fig. 28 shows a poly-Si film fully crystallized at  $500^\circ\text{C}$ , lifted off the glass substrate, and transferred onto a metal substrate so that the former glass/poly-Si interface could be investigated. During the HF lift-off, the Al clusters were etched away leaving holes in the film, which are depicted as small black dots with bright rims in the SEM images. In the

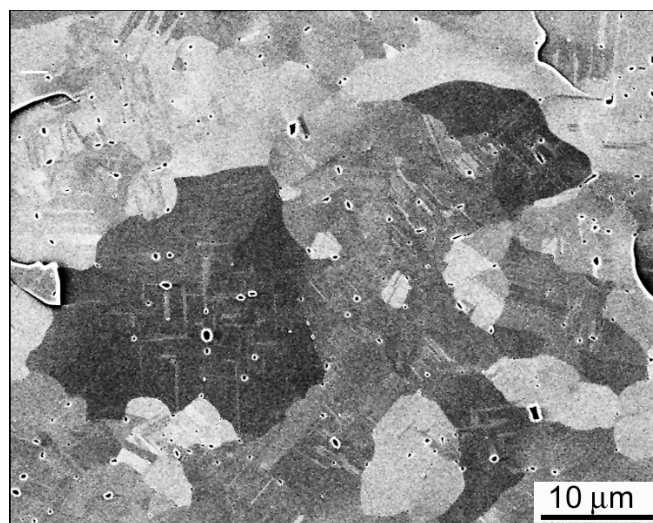


Fig. 28: Electron channelling SEM image of the former glass/poly-Si interface of a fully crystallized sample showing little holes in the film caused by inter- and intra-grain Al clusters, as discussed in the text. Four cracks due to the sample preparation are visible.

image shown, these voids account for less than 0.2 % of the total area. Due to the channelling contrast in Fig. 28, it is possible to distinguish between inter- and intra-grain Al clusters. It can be observed from the large dark grain in the left half of the micrograph that the intra-grain Al clusters are preferentially located at lighter streaks. These streaks are crystallographic faults inside the grain. Since crystallographic faults can be related to the dendritic growth, this observation supports the hypothesis that dendritic growth is responsible for the formation of intra-grain Al clusters trapped between Si grains and substrate during ALILE.

To elucidate the actual Al concentration within the poly-Si material, a fully crystallized film, annealed at 500°C, was lifted off the glass substrate, turned up-side down and transferred to a metal substrate. SIMS measurements were therefore conducted on bare Si films free of Al clusters. The depth profile of the 500 nm thick layer started at the smooth, clean surface of the former glass/poly-Si interface. For a quantitative analysis a c-Si wafer with  $10^{20} \text{ cm}^{-3}$  Al atoms ion-implanted served as a calibration standard. The measurement shown in Fig. 29 reveals that the poly-Si layer predominantly contained Al at a concentration of about  $3 \times 10^{19} \text{ cm}^{-3}$  (0.06 at.%).

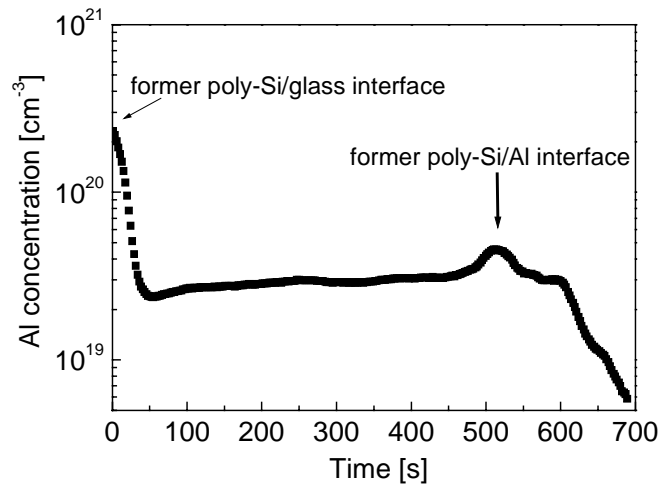


Fig. 29: SIMS measurement of a poly-Si film turned up-side down. The continuous poly-Si film is 500 nm in thickness.

The SIMS depth profile shows two areas of increased Al concentration. The local maximum after a sputtering time of 500 s can be attributed to the Al oxide layer at the former poly-Si/Al interface as discussed in chapter 4.5.2. The fact that the Al concentration does not decrease abruptly at depths beyond this maximum is due to residual Si crystals that were formerly embedded in the Al matrix and are connected to the continuous poly-Si layer. The second area is found at the former glass/poly-Si interface. The possibility that

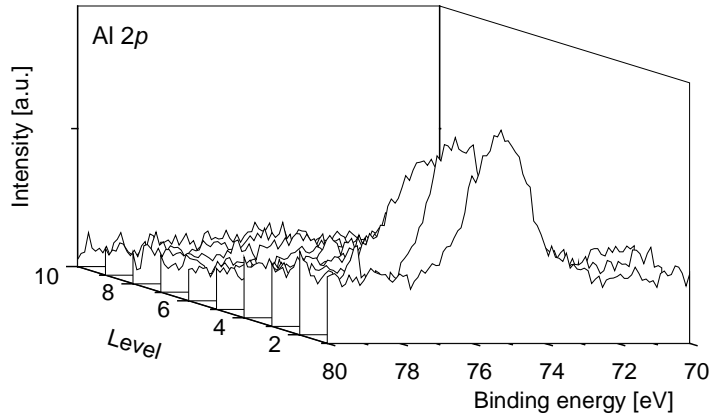


Fig. 30: Depth profile of XPS spectra in the region of the Al 2*p* response taken of the former glass/poly-Si interface.

the increased Al concentration measured at the beginning of the depth profile is an artefact of the SIMS measurement is ruled out by the XPS analysis shown in Fig. 30.

The depth profile shows only the first few spectra, thus, the first couple of nm, which depict the quick decrease of the Al concentration into the film. The Al atoms are bonded to oxygen as apparent from an Al<sup>ox</sup> binding energy of 75 eV, instead of 73 eV for metallic aluminium. The decrease of the Al<sup>ox</sup> peak intensity corresponds well with the decrease of the oxygen concentration also measured using XPS (spectra not shown). The enhanced concentration of an Al oxide phase at the glass/poly-Si interface can be understood when the interaction of the Al film and the glass substrate is considered. The Al oxide layer is formed due to the reduction of the glass Si oxide by the adjacent Al layer during the annealing process, as will be discussed in chapter 6.2.

To determine whether the Al concentration in the poly-Si material depends on the annealing temperature during the crystallization process, pieces of the same samples were processed at 425°C, 475°C and 500°C. SIMS measurements did not reveal a particular temperature dependent trend. The Al concentration within one Al depth profile varied more – between  $2.2$  and  $4.0 \times 10^{19} \text{ cm}^{-3}$  – than the average Al concentration. The question of how the incorporated Al atoms influence the nature of the poly-Si is investigated in chapter 5.3 by analysing the electrical properties of the material.

**Summary:** Aluminium atoms are incorporated into the substrate/Si film structure within the poly-Si material itself and in the form of clusters trapped at the glass/film interface. Two different types of clusters were identified: Inter-grain and intra-grain clusters. The Al concentration in the poly-Si film is about  $3 \times 10^{19} \text{ cm}^{-3}$ .

## 5.2 Grain structure and orientation

The main parameters of aluminium-induced crystallization of a-Si leading to the Al/Si layer exchange process were investigated in chapter 4. Their influences on the overall exchange process and the formation of continuous poly-Si films at low temperatures have already been discussed. Although Raman spectroscopy gave a preliminary indication for the good crystallographic quality of the polycrystalline material, no in-depth crystallographic analysis has been presented yet. From in-situ optical microscopy studies during annealing at a temperature of 475°C an average grain size exceeding 10 µm was extracted (chapter 4.1). However, electron channelling SEM investigations already revealed that the grains contain crystallographic faults and possible twin boundaries. In this chapter orientation imaging, transmission electron and scanning electron microscopy are used to elucidate the inner-grain structure, the grain boundaries, the grain orientation and the overall crystallographic quality of the polycrystalline Si film.

A common technique to investigate grain size as well as crystallographic grain quality of poly-Si is the use of an etching solution that preferentially etches grain boundaries and defects. Fig. 31 depicts a poly-Si film formed at 475°C where grain boundaries and crystallographic faults are visualised due to chemical etching in a HNO<sub>3</sub>/HF solution (100:1) for 30 sec. It is apparent from the figure that some grains exceed 10 µm in size. However, the micrograph also reveals that some of them appear to contain a subgrain-structure and numerous defects. The investigation of this substructure is important when the feasibility of the poly-Si material for subsequent device fabrication is studied. Minor fractions of areas of lower crystallographic quality have already a negative impact on the overall solar cell performance [75].

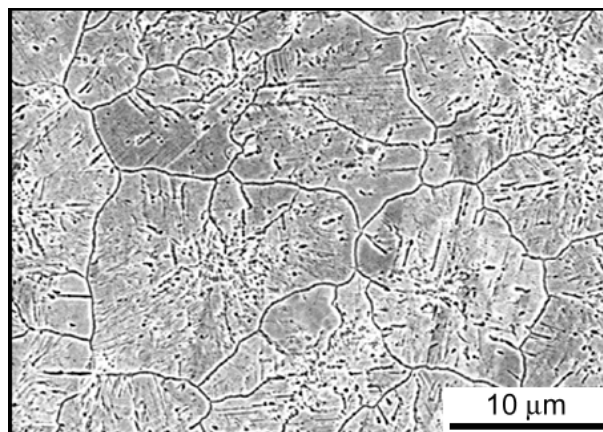


Fig. 31: SEM image of poly-Si film on glass after HNO<sub>3</sub>/HF etching.

The difficulty arising from an etching step to analyse the crystallographic structure of poly-Si is that grain boundaries (GBs) and inner-grain faults are accentuated in the same way. The distinction between them is therefore complicated. In this case an orientation imaging microscope (OIM) can serve as a powerful tool to investigate grain sizes and boundaries. Orientation imaging micrographs are the result of step-by-step analysis of the backscattered Kikuchi diffraction (BKD) with a step size of  $0.36\ \mu\text{m}$  in the following OIM study. BKD is also known as electron back-scattering diffraction pattern – EBSD [76]. The Kikuchi bands of the BKD reveal the crystallographic orientation of the analysed spot. When a grid-like pattern is scanned over a poly-Si film, areas of matching crystallography can be identified, and grain sizes as well as orientation can be extracted. Boundaries between areas of different crystallographic orientations are classified according to the coincident site lattice (CSL) theory. This theory is based on the hypothetical interpenetration of two neighbouring lattices. If a fraction of lattice sites of the two overlapping extended grains coincide a *superlattice* can be constructed consisting of the coincident sites. The ratio of the unit cell volumes of this coincident site lattice and of the original crystal structure of the grains defines the coincidence index  $\Sigma$ . For example, the unit cell of the coincident site lattice of two neighbouring grains separated by a  $\Sigma 3$  GB is three times as large as the unit cell of the crystallographic structure of the individual grains. For a more detailed discussion of the CSL theory see Ref. [77].

Fig. 32 shows an orientation imaging micrograph of a poly-Si film formed at  $425^\circ\text{C}$ . To stop rough surface features on top of the Si layer from disturbing the analysis, the film was etched off the glass substrate and transferred up-side down onto a metal substrate. This enabled the investigation of the smooth glass/poly-Si interface. The grey variation in the image is determined by the *image quality factor* (IQ). The IQ represents the contrast of the Kikuchi bands in the BKD pattern at each step. The dark area in the top half to the very right of the image is, for example, a crack in the Si film that occurred during the lift-off and transfer procedure. In this defect area no BKD with analysable contrast is detected. Consequently, the IQ is low and the crack appears dark. The white and black lines in Fig. 32 are boundaries between regions of different crystallographic orientations as extracted from the BKDs. As apparent from the micrograph, the poly-Si material consists of grains whose sizes exceed  $10\ \mu\text{m}$ , but there are also areas where the grain sizes are only a couple of  $\mu\text{m}$ . The average grain size of the particular area analysed in Fig. 32 is therefore reduced to  $6.2\ \mu\text{m}$ .

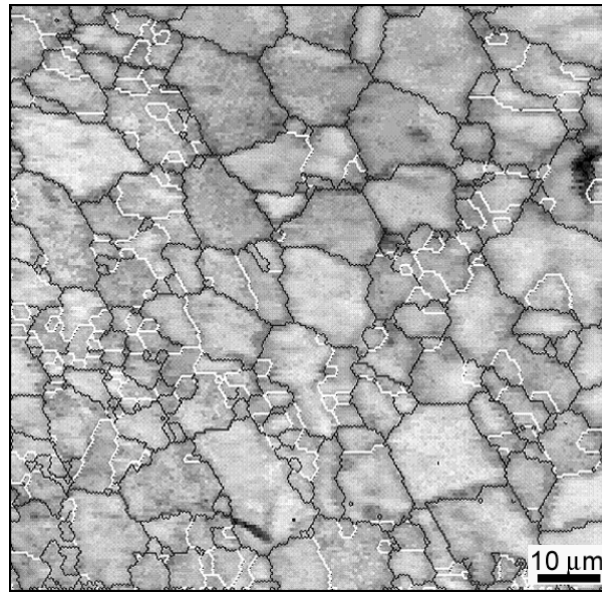


Fig. 32: Orientation imaging micrograph of the former glass/poly-Si interface of a sample annealed at 450°C. Grain sizes and grain boundaries are depicted; the white lines are  $\Sigma 3$  and  $\Sigma 9$  boundaries, the black lines represent all the other grain boundaries.

The existence of small grains seems to be in contradiction to the results presented in chapter 4.1. According to the in-situ optical microscopy investigations, the formation of new nuclei is suppressed at an early stage of the crystallization process. This suppression of further nucleation enables the growth of large grains. It will be discussed later that the suppression of nucleus formation is due to the interference of already existing and growing grains at an early stage of ALILE (see chapter 6.4). Therefore, if large grains are formed, only very few small grains should be present. In this case *large* and *small* means above 10  $\mu\text{m}$  and below 5  $\mu\text{m}$  in diameter, respectively. The apparent contradiction between the OIM results and the optical microscopy investigations will be analysed in the following paragraphs.

The grain boundaries of the poly-Si material analysed in Fig. 32 can be distinguished into two groups: (a) Coincident site lattice grain boundaries, CSL GBs, with coincidence index  $\Sigma 3$  and  $\Sigma 9$  (white lines) and (b) all other types of GBs (black lines). The ratio of  $\Sigma 3$  to  $\Sigma 9$  GBs amongst the white lines is about unity. It is apparent from the micrograph that the grains in the small-grained areas are predominantly separated by  $\Sigma 3$  and  $\Sigma 9$  grain boundaries. Both types of CSL GBs have low atomic distortions [78]. The low distortion is evident from Fig. 33, which shows a schematical presentation of a grain boundary with a coincidence index  $\Sigma 3$ . This type of twin boundary can be theoretically constructed by dividing a Si crystal along the  $\{111\}$  plane, rotating one half by  $180^\circ$  around the  $\langle 111 \rangle$

axis, and rejoining the two halves again. The resulting crystallographic structure locally resembles a Wurtzite lattice at the grain boundary. Theoretically, no bond bending occurs and the formation of dangling bonds is prevented. The other half of the CSL grain boundaries have the index  $\Sigma 9$ . GBs of this type can be constructed by splitting a Si crystal along the twin plane  $\{221\}$  followed by a rotation of  $38.9^\circ$  around the  $\langle 110 \rangle$  axis. Fedotov et al. showed that  $\Sigma 3$  and  $\Sigma 9$  GBs in silicon are electrically inactive grain boundaries in as grown crystals [79,80]. However, in the discussion of orientation imaging microscopy it has to be mentioned that the grain boundary classification is determined by the orientation of neighbouring crystal areas and that the actual structure of the grain boundary remains unknown. It is an assumption that the grain boundary plane itself resembles the theoretical CSL GB structure. Only high resolution TEM studies would allow the direct investigation of the crystallographic nature of the grain boundary.

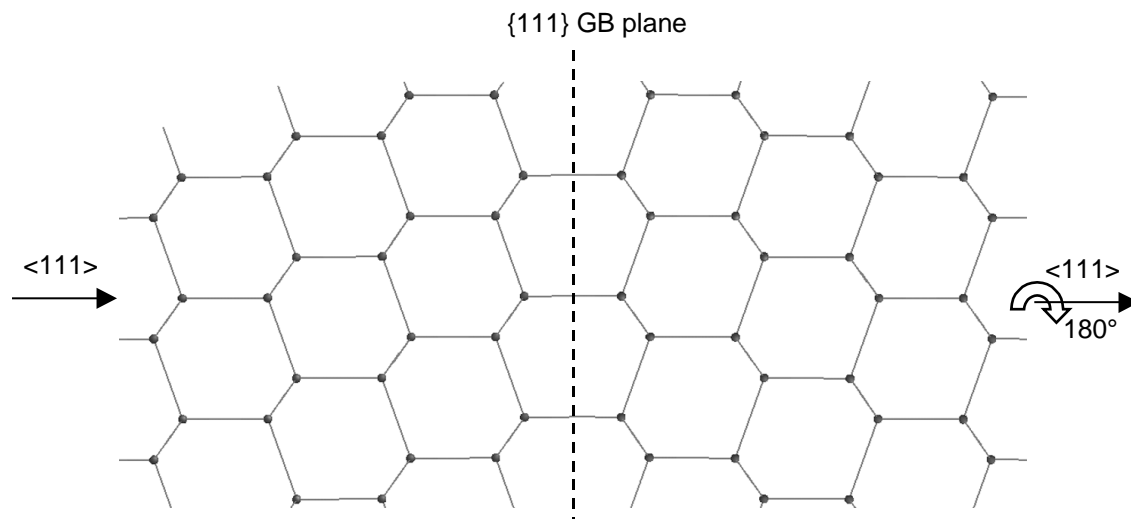


Fig. 33: Schematical presentation of the  $\Sigma 3$  grain boundary, which is a symmetric boundary with the  $\{111\}$  plane as GB plane. The small balls represent the Si atoms and the sticks the Si-Si bonds. The crystal structure drawn is a plane view onto the  $\{110\}$  plane. The two Si crystal structures are rotated by  $180^\circ$  to one another around the  $\langle 111 \rangle$  axis.

The question remaining is where the small-grained regions in Fig. 32 stem from if they are not expected from the nucleation and growth pattern of the Si grains according to the optical microscopy studies. To investigate this question large isolated grains were grown using the set of parameters investigated in chapter 4. Low annealing temperatures ( $\sim 425^\circ\text{C}$ ), large grain size of the polycrystalline Al layer and an interface oxide grown over an extended period of time ( $\sim 24$  h) in ambient air, lead to slow grain growth during which the crystallization process was stopped after 75 min. The successful formation of isolated grains was verified by investigating the film/glass interface using optical microscopy. In

the optical micrographs, the Si grains could be clearly distinguished from the surrounding highly reflective Al matrix. The images were similar to the one shown in Fig. 12 of chapter 4.1. Since the grains were formed within the Al film between the top a-Si layer and the glass substrate, the grains had to be detached from the glass as a prerequisite for OIM measurements. To support the isolated grains, the a-Si film of the layer structure as deposited was chosen to be three times as thick as the Al layer. Consequently, the Si grains formed within the Al layer were connected to a Si network similar to the one shown in Fig. 13 of chapter 4.2. This Si network supported the isolated Si grains whilst the entire film was lifted off the glass and transferred up-side down on to a metal substrate. During the lift-off process using concentrated HF, the aluminium was etched away leaving the Si grains protruding from the Si network film. Fig. 34 depicts the distribution of isolated Si grains. The grains are of the same thickness as the original Al layer (~400 nm). The strong dendritic growth shown in the SEM images is especially prevalent when the process parameters are set to encourage slow and large grain growth. The dendritic growth pattern is typical for metal-induced crystallization of a-Si [24].

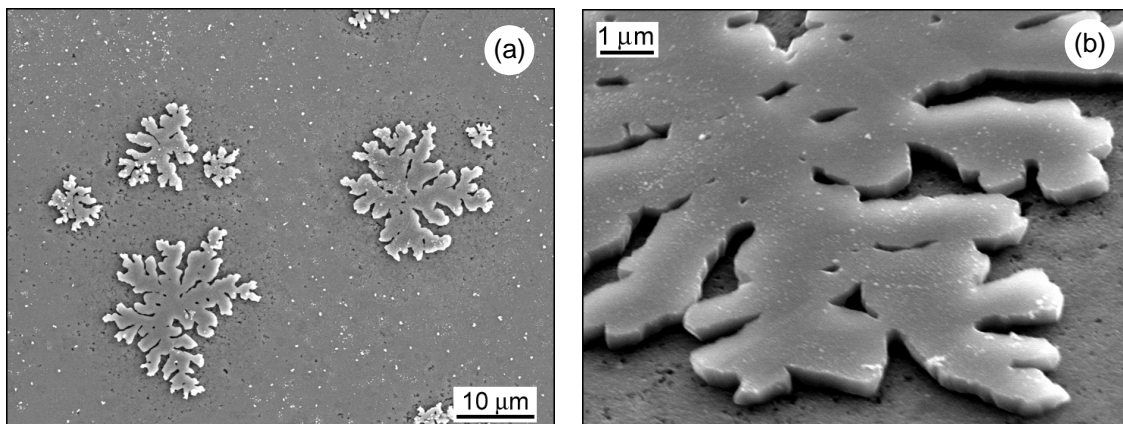


Fig. 34: SEM images of isolated Si grains on a Si network film as a supporting layer showing (a) the distribution of isolated grains and (b) a close-up of a protruding Si grain.

Raman investigations of the whole Si system (Si network and Si grains) are exhibited in Fig. 35. One of the two Raman spectra shown was taken with the laser spot focused on an isolated grain. It depicts the typical crystalline silicon spectrum with the peak maximum at  $520\text{ cm}^{-1}$ . The other measurement was taken from the supporting Si network. The spectrum is composed of amorphous and crystalline fractions. The deviation of the crystalline peak at  $517\text{ cm}^{-1}$  from  $520\text{ cm}^{-1}$  indicates that the crystalline phase in the Si network is exposed to internal strain. The existence of a crystalline phase in the amorphous Si supporting layer can be attributed to the Al material that was extruded by the growing Si grains within the metal film. This Al partially induced crystallization in the thick a-Si film.

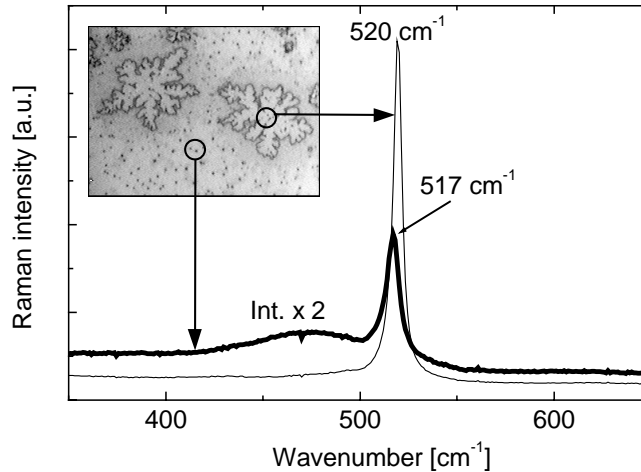


Fig. 35: Raman spectra taken from an isolated grain and from the supporting Si-network. The signal of the supporting film is multiplied by 2 for better visualisation of the spectrum. The optical micrograph of the area analysed is also shown.

The purpose of processing isolated grains was to investigate at what stage the CSL grain boundaries are formed. There are two possibilities: (i) The  $\Sigma 3$  and  $\Sigma 9$  GBs develop during the grain growth process, meaning that one grain grown from one nucleus contains subgrains of different crystallographic orientations separated by CSL GBs, or (ii) these types of GBs evolve when adjacent grains coalesce, which involves two grains grown from two different nuclei. Fig. 36 shows an OIM image of a Si network layer with protruding isolated Si grains visible as light grey areas (IQ high). The supporting Si network appears dark (IQ low). The white and black lines again represent grain boundaries. Whilst the lines drawn over the region of the supporting film can be ignored as noise, the grain boundaries exhibited on the isolated grains have to be discussed. It is apparent from the micrograph

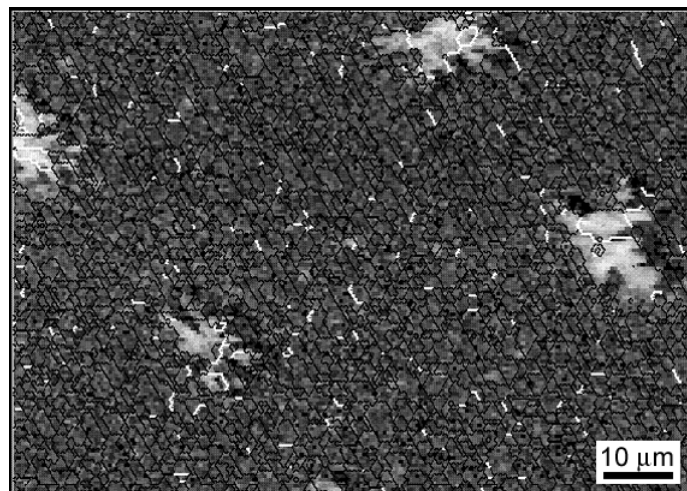


Fig. 36: Orientation imaging micrograph showing the analysis of isolated Si grains protruding from a Si network. The sample investigated is identical to the one used in Fig. 34 and Fig. 35. The white lines represent  $\Sigma 3$  and  $\Sigma 9$  grain boundaries.

that the grains predominantly contain  $\Sigma 3$  and  $\Sigma 9$  GBs represented by the white lines. Since the isolated grains analysed have grown from individual nuclei, Fig. 36 gives an indication that the twin boundaries indexed  $\Sigma 3$  and  $\Sigma 9$  are formed during the growth process of individual grains. It is therefore the first of the two possibilities listed above that seems to be more coherent with the observations presented.

The OIM measurement on isolated grains allows to resolve the contradiction between the grain size revealed from optical microscopy (OM) investigations and the grain size depicted by the OIM studies. In the OM analysis a grain is classified as a crystalline Si area grown from one nucleus. Crystallographic faults, like the development of a twin grain boundary, are not observable. This is different in OIM investigations where a grain is detected as an area of identical crystallographic orientation. From the combination of results of both methods, the polycrystalline Si layer can be seen as large-grained material with some grains containing a subgrain structure. This structure consists of areas of different crystallographic orientations separated by CSL grain boundaries with indices  $\Sigma 3$  and  $\Sigma 9$ .

Besides the grain size and boundary analysis, the OIM reveals the crystallographic orientation of the Si crystals extracted from the BKD pattern. Fig. 37 shows two OIM images taken from samples that were annealed at 450°C and 525°C. Fig. 37a is the same

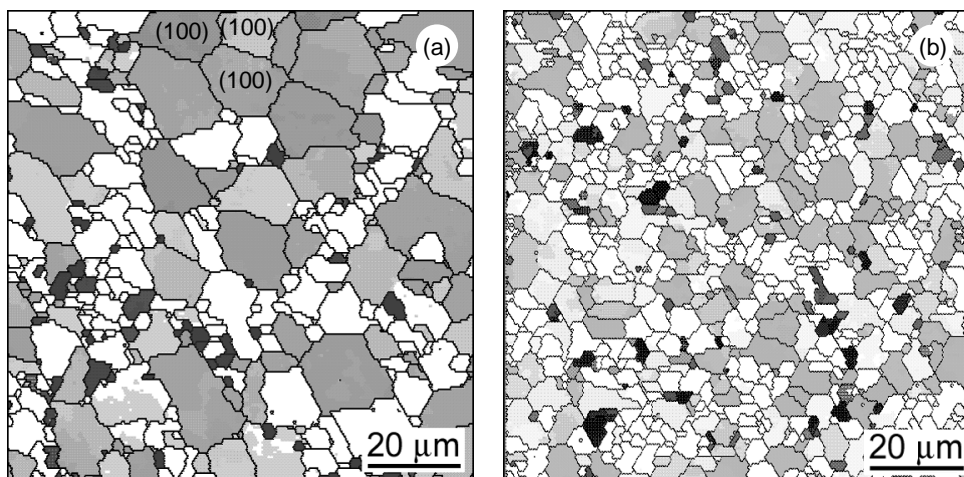


Fig. 37: Orientation imaging micrographs of samples annealed at (a) 450°C and (b) 525°C. The black lines represent grain boundaries. The dark grey areas are grains with (111) orientation except for 6 grains in (a) and 13 grains in (b) with (110) orientation. All light grey areas are orientated within a 15° cone along the (100) direction. The lighter the grey, the stronger is the deviation from the exact (100) direction. Three grains with (100) orientation are indexed in (a) as examples. All white areas are orientated in directions that do not fall in any of the three categories.

measurement as Fig. 32, but this time the grain orientation is displayed instead of the IQ. The dark grey areas represent (111) and (110) orientation combined, while the light grey shading represents grains orientated in the (100) direction. All other grains (white) are not orientated in any of these three directions. Amongst the dark grey grains there are only a small fraction orientated in the (110) direction (9 and 16 grains in (a) and (b), respectively). The images reveal two aspects of special interest: (i) the grains are larger when the poly-Si film is formed at lower temperatures and (ii) there seems to be a preferential (100) orientation predominantly of the larger grains. The (100) orientation is prevalent in the middle area of the upper half of the image shown in Fig. 37a containing large grains ( $>15\ \mu\text{m}$ ).

The finding of the OIM investigation that the grain sizes increase with decreasing annealing temperature clearly supports the results presented in chapter 4.3. The preferential (100) orientation, as extracted from OIM investigation analysing an area of  $100\times 100\ \mu\text{m}^2$ , was verified using XRD measurements. Diffractograms of four Si reflections of the poly-Si samples within  $25^\circ < 2\theta < 85^\circ$  were recorded with a position sensitive detector, having Miller indices (111), (220), (311) and (400). The recorded Bragg reflections could be fitted well by appropriate line shape functions like splitted Lorentzians from which the integrated intensities were derived. Intensity values were corrected for finite absorption with a thickness-dependent absorption factor  $A = (1 - \exp(-2\mu d/\sin\theta))$  [81], where  $d$  accounts for the film thickness and  $\mu = 148\text{cm}^{-1}$  denotes the X-ray absorption coefficient for Si and  $\text{CuK}\alpha$  radiation. The analysed spectra shown in Fig. 38 are taken from a sample area of many  $\text{mm}^2$ . The four reflections of a 250 nm thick sample displayed have been corrected by dividing the measured intensities with the thickness-dependent absorption factor  $A$ . The intensities are normalised with respect to the (111) Bragg reflection, which is set to 100 %. The figure also shows the integral intensities of a silicon powder according to JCPDS card 27-1402 [82] with a random orientation of grains.

Two interesting facts can be determined from the comparison of both intensity sets in Fig. 38. Firstly, the (220) reflection in the poly-Si film formed using ALILE (ALILE film) is found to be negligibly small in comparison to a random orientation. It can be concluded that the growth of silicon grains with (110) crystallographic lattice planes parallel to the substrate is insignificant for films formed by ALILE. Secondly, the (400) reflection is enhanced by a factor of 7.5 in comparison to a randomly orientated ensemble of Si grains. This effect of enhanced (100) orientation has also been observed for ALILE films formed at other temperatures ( $425^\circ\text{C}$ ,  $450^\circ\text{C}$  and  $475^\circ\text{C}$ ) and corroborates the result of the OIM

investigation. Thus, it can also be concluded that ALILE films exhibit a (100) texturing that contrasts to poly-Si processed by solid phase or laser crystallization, which is of preferred (111) orientation [83,84]. This effect qualifies ALILE films as seeding layers for epitaxial thin-film silicon growth, since successful epitaxial growth was observed to occur preferentially on (100) orientated Si substrates [85]. For potential use as seeding layers more convenient layer sequences such as poly-Si/back contact/substrate structures can easily be formed employing the Al-induced layer exchange process (see chapter 7.1). The origin of the preferential (100) orientation might lie in the fact that the Si crystallization occurs at the Al oxide interface. ALILE can be interpreted as Si growth on an Al oxide surface from a solid Al solution. However, this is a mere speculation and further investigations are needed to gain more insight into the reason of the (100) texturing.

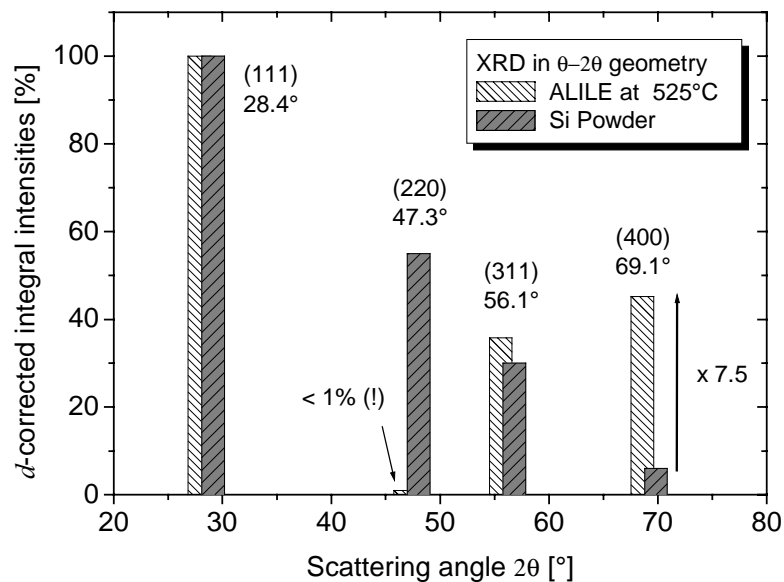


Fig. 38: XRD measurements presenting the integral intensities of poly-Si film formed at 525°C (ALILE at 525°C) compared to a standard Si powder. The film thickness ( $d = 250$  nm) has been taken into consideration.

The structural analysis of the poly-Si films in this chapter has so far focussed on the determination of the grain size, boundaries and orientation of the material. To investigate the inner grain structure of the polycrystalline films, TEM investigations were conducted. Two TEM images are shown in Fig. 39 taken from a sample annealed at 450°C. Both images exhibit black areas that are a few 100 nm in size. These areas are holes in the thinned TEM specimens. They originate from Al clusters that had been trapped between the continuous poly-Si film and the glass substrate. The appearance of these Al clusters was discussed in detail in chapter 5.1. Fig. 39a reveals typical bend contours in the form of white wavy lines, which indicate monocrystalline material of high crystallographic quality

in this area. Fig. 39b taken at higher magnification shows the primary intragrain twin defects that can be found in the material. Comparing these images to TEM investigations on SPC poly-Si [86], it seems that the poly-Si material formed by an Al-induced layer exchange process is of superior crystallographic quality. This difference can be attributed to the fact that during the layer exchange, no atom remains where it was, but a complete dissolution and restructuring process of the Si phase takes place. Beside the TEM results concerning the crystallographic quality, it is worthwhile mentioning that, according to electron dispersive x-ray spectroscopy, no evidence of an enhanced Al concentration at Si grain boundaries could be found.

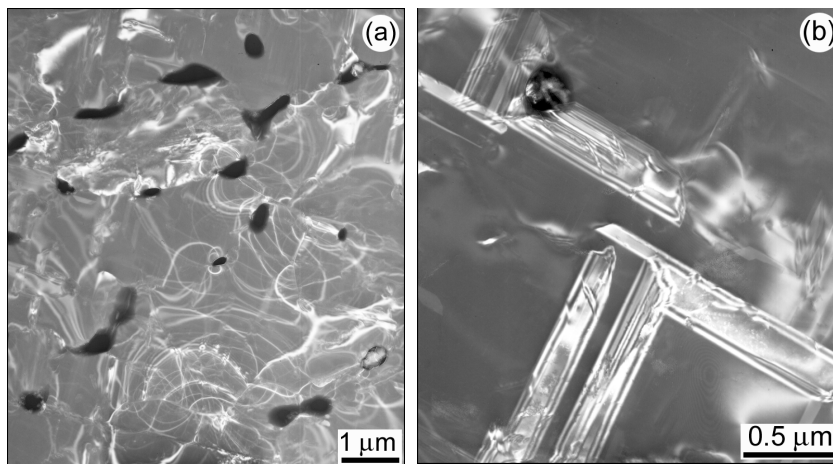


Fig. 39: Bright-field TEM images taken from a sample annealed at 450°C at different location and magnification.

**Summary:** The poly-Si films consist of grains with a lateral extension of many  $\mu\text{m}$ . Some of these grains contain a subgrain structure that manifests itself in areas of different crystallographic orientation. These areas seem to be separated by coincident site lattice grain boundaries with coincidence index  $\Sigma 3$  and  $\Sigma 9$ . Due to this subgrain structure, a Si grain grown from one nucleus is not necessarily of identical crystallographic orientation. The grains of the poly-Si films have a preferential (100) orientation. Furthermore, the inner crystallographic grain quality in terms of defects seems to be superior to conventionally solid phase crystallized poly-Si material.

## 5.3 Electrical properties

Chapter 5.1 revealed that the poly-Si material formed by an aluminium-induced layer exchange process contains  $3 \times 10^{19} \text{ cm}^{-3}$  Al atoms after full crystallization. The incorporated Al atoms influence the electrical properties of the polycrystalline Si film. The investigation of the electrical characteristics of the material is a mandatory task, if any subsequent device fabrication, e.g. solar cells, is considered. The resistivity, the free carrier concentration and their mobility are important properties, which are the subject of this chapter. The measurements were conducted on poly-Si films on glass where the Al that had segregated to the top of the film during the crystallization process was etched off to expose the bare polycrystalline material. The following chapter is divided into three sections. The first section comprises the investigation of the basic electrical nature of ALILE poly-Si by exemplary measurements of a Si film annealed at  $500^\circ\text{C}$ . The second section analyses how some of the electrical properties vary depending on the temperature of the ALILE process. The third section discusses the ratio of electrically active to non-active Al atoms incorporated in the polycrystalline silicon. The results are only summarised at the very end of this chapter.

### 5.3.1 Hall effect measurements

In order to determine the basic electrical properties of a poly-Si layer formed at  $500^\circ\text{C}$ , Hall effect measurements were performed between 13 and 470 K. At room temperature the measured values of resistivity  $\rho$ , hole concentration  $p$ , and Hall mobility  $\mu_{\text{H}}$  were  $0.041 \text{ }\Omega\text{cm}$ ,  $2.6 \times 10^{18} \text{ cm}^{-3}$ , and  $56.3 \text{ cm}^2/\text{Vs}$ , respectively. However, by investigating four sample pieces from the same specimen, slight variations could be detected. The lowest result of the Hall mobility ( $54.0 \text{ cm}^2/\text{Vs}$ ) was correlated to the highest hole concentration ( $2.86 \times 10^{18} \text{ cm}^{-3}$ ). Therefore higher carrier concentrations are connected to lower mobilities indicating that impurity scattering is the dominant scattering process [87] rather than variations of the crystal quality or of the influence of grain boundaries. The high carrier concentration is due to the incorporation of Al atoms on substitutional lattice sites of poly-Si. The substitutional point defect  $\text{Al}_{\text{Si}}$  is a well known shallow acceptor in Si, having an activation energy of 68 meV [88]. The values of the Hall mobility  $\mu_{\text{H,p}}$  are in the vicinity of

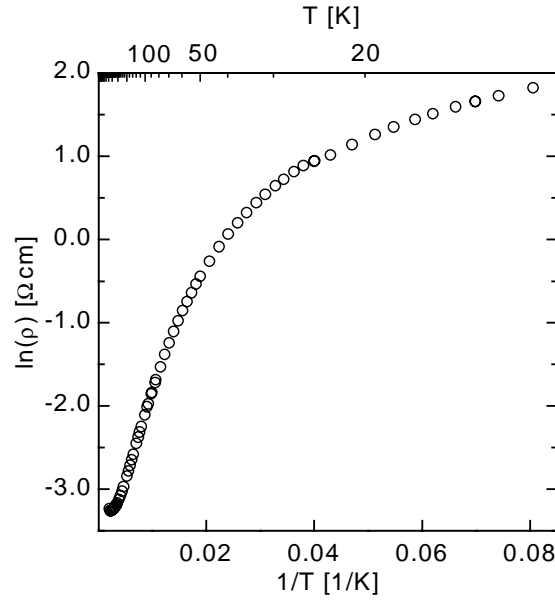


Fig. 40: Temperature dependence of the resistivity of the poly-Si material.

the theoretical maximum for monocrystalline p-Si at this doping level ( $\mu_{c-Si} \approx 100 \text{ cm}^2/\text{Vs}$  [89]).

The temperature dependent behaviour of the resistivity  $\rho(T)$  is shown in Fig. 40. With the exception of temperatures near room temperature,  $\rho(T)$  always increases with decreasing temperature. However, below 50 K the slope of the curve decreases. The change of curvature can be discussed in terms of defect band (DB) conduction. The presence of a defect band is expected in a semiconductor so highly doped. This means that there is a transition temperature range in which both normal valence band (VB) conduction and DB conduction contribute to the electrical transport (two-band conduction). Although two-band conduction is theoretically well understood [90] it is difficult to separate the contributions of VB and DB.

To calculate the hole concentration  $p$  and Hall mobility  $\mu_H$  obtained from the experimentally determined Hall coefficient  $R_H$ , we applied the conventional formulae

$$p = 1/qR_H \text{ and} \quad (1)$$

$$\mu_{H,p} = R_H/\rho, \quad (2)$$

setting the Hall scattering factor  $r_H = 1$ . However, at low temperatures the electrical characteristics are strongly influenced by the DB conduction, leading to an anomalous behaviour of the Hall effect [90].

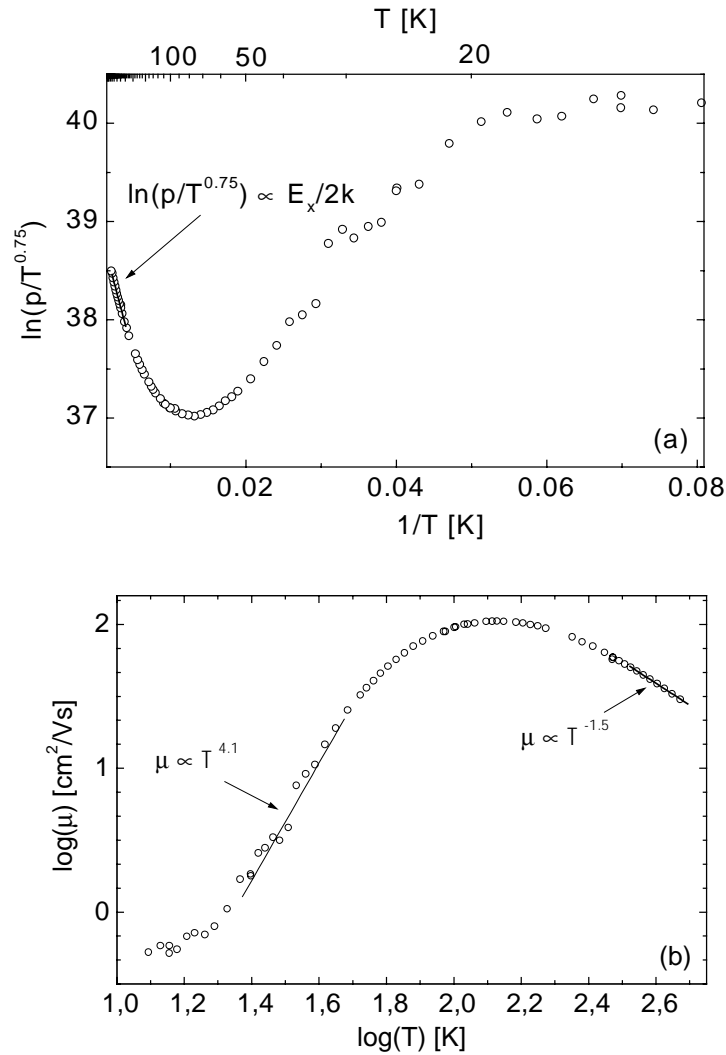


Fig. 41: Results of Hall effect measurements; (a) apparent hole concentration, the  $\ln(p/T^{0.75}) \sim E_x/2k$  relation ( $E_x = 54$  meV and  $k$  is the Boltzmann constant) was obtained by a linear fit in the temperature range 300 K – 450 K, and (b) apparent Hall mobility. The  $\mu \sim T^{4.1}$  and  $\mu \sim T^{-1.5}$  relations were obtained by linear fitting procedures in the temperature range 25 K - 45 K and 335 K – 468 K, respectively.

Fig. 41a shows that  $p(T)$  decreases with decreasing temperature, from 470 K down to below 100 K. At the high temperature range ( $T > 300$  K) the plot of  $\ln(p/T^{0.75})$  versus  $1/T$ , taking into account that the effective density of states is proportional to  $T^{1.5}$ , reveals a straight line. The slope equals  $E_x/2k$ , where  $E_x = 54$  meV and  $k$  is the Boltzmann constant. As  $E_x$  is in the vicinity of the activation energy  $E_A$  of Al-impurities, the suggestion is that the hole concentration is in the “freezing out range” at these temperatures. Screening of the electrical potential of impurities due to high doping levels can explain why  $E_x$  is smaller than  $E_A$  [91]. In this analysis counter-doping by donor-like impurities, e.g. oxygen, are neglected because of the high Al doping concentration. At about 70 K there is a minimum value of  $p(T)$ , marking the transition to DB conduction. At even lower temperatures the

apparent hole concentration rises, indicating that the Hall effect signal is increasingly influenced by DB and therefore shows anomalous behaviour. The rapid freezing of the free holes at low temperatures leads to further deionisation of the Al with even greater importance on conduction through the DB. Below 20 K the determined values for  $p$  fluctuate around a constant value. The suggestion is that at this temperature range the transport process is dominated by DB conduction.

In Fig. 41b the  $\mu_{H,p}(T)$  curve, complementing the results shown in Fig. 41a, is presented. It has a maximum of  $105 \text{ cm}^2/\text{Vs}$  at 135 K. Below this temperature,  $\mu_{H,p}$  decreases rapidly. Between 30 K and 45 K,  $\mu_{H,p}$  is proportional to  $T^{4.1}$ . The value of the exponent is much higher than the value of 1.5, which is theoretically expected for impurity scattering [92]. However, the anomalous behaviour of the Hall mobility can be explained qualitatively within the framework of the two-band conduction model. The strong temperature dependence of  $\mu_{H,p}$  results from the presence of holes with high mobility in the VB and holes with low mobility in the DB, as well as the temperature dependence of the concentration ratio of VB holes to DB holes. As expected for DB conduction, the mobility below 20 K is very low ( $\mu_{H,p} \approx 0.5 \text{ cm}^2/\text{Vs}$ ). Thus, at temperatures below 135 K, defect band conduction begins to dominate the electrical characteristics. The results presented are very similar to the ones on highly doped single crystal germanium published by Hung and Gliessman [90]. They also discussed their findings in terms of defect band conduction.

Above the temperature of 135 K, the mobility is proportional to  $T^{-1.5}$  in the linear fit range of the double-logarithmic scales, shown in Fig. 41b. This relationship can be interpreted in a way that the mobility in the temperature range of 330 K and above follows the classically predicted temperature dependence of semiconductors when phonon scattering is the dominant scattering mechanism [92]. The fact that the mobility decreases with increasing temperature is understandable in terms of enhanced phonon scattering within the crystallites but in contradiction to conduction governed by thermionic emission or tunneling across grain boundaries. In the latter cases the mobility is expected to increase with rising temperature. In large-grained material with high doping concentration, such as the poly-Si formed using Al-induced layer exchange, the electrical properties are dominated by the properties within the crystalline grains [93].

### 5.3.2 Influence of the annealing temperature

So far, the poly-Si films, whose electrical properties were investigated, were processed at an annealing temperature of 500°C. To determine whether and how these electrical properties depend on the processing temperature, a set of samples was annealed at different temperatures ranging from 350°C to 500°C.

Fig. 42a shows that the free carrier concentration  $p$  is dependent on the temperature of the aluminium-induced layer exchange process. The dashed straight line is a linear fit to the filled triangle data points to emphasize the increasing concentration with increasing annealing temperatures. The hole concentration is based on the number of Al atoms located on substitutional lattice sites of the polycrystalline Si. This increasing Al-dopant concentration is accompanied by a decreasing Hall mobility as revealed in Fig. 42b. Again, the dashed line is a linear fit to the filled triangles showing the general trend of decreasing

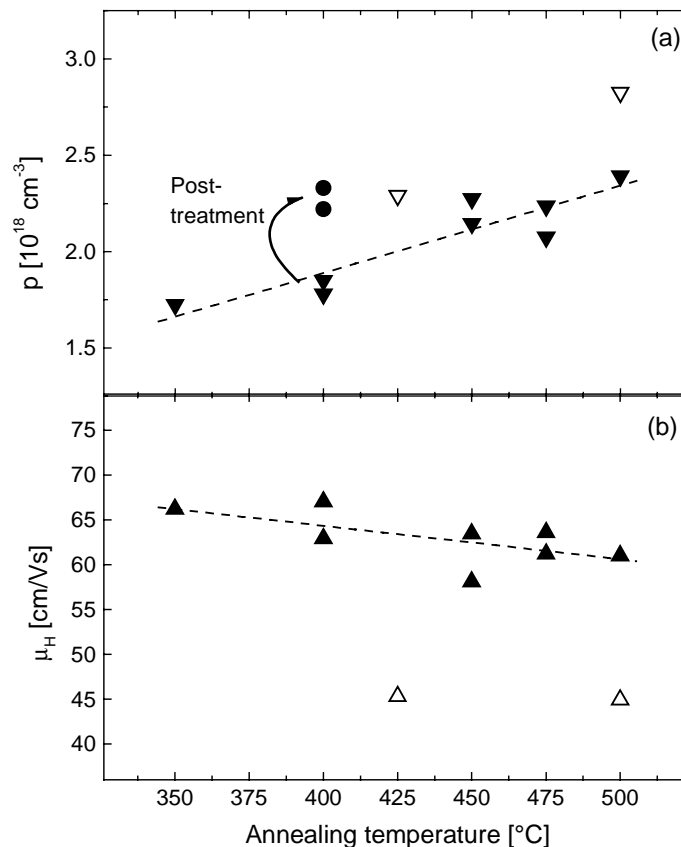


Fig. 42: Hall effect measurements at room temperature of poly-Si layers on glass formed by ALILE at different temperatures, (a) hole concentration  $p$  and (b) Hall mobility  $\mu_H$ ; the Hall scattering factor was set to unity. The dashed lines are linear fits to the filled triangles. The open triangles are believed to be exceptions. The bowed arrow in (a) indicates the change of  $p$  due to an additional heat treatment at 500°C for 30 min of the bare poly-Si layers, originally crystallized at 400°C.

mobility. This means that at higher concentrations of substitutional Al atoms, impurity scattering leads to a lower hole mobility in the poly-Si material. Nevertheless, Hall mobilities were measured to be between 60 and 70 cm<sup>2</sup>/Vs for all but two samples. It is unclear why two samples, one annealed at 425°C and the other at 500°C (open triangles in Fig. 42a and b), showed results, which did not follow the trends.

It is interesting to note that the lower carrier concentration of poly-Si films annealed at lower temperatures could be increased by additional heat treatment of the bare films after the metallic Al was etched off. This behaviour is indicated in Fig. 42a by the bowed arrow for two samples originally annealed at 400°C. After Al etching, the samples were again heated, though at a higher temperature of 500°C for 30 min. This post-treatment increased the carrier concentration from approximately  $1.8 \times 10^{18} \text{ cm}^{-3}$  to  $2.3 \times 10^{18} \text{ cm}^{-3}$ , a similar value to the concentration of the samples which were annealed at 500°C during ALILE. To understand this behaviour it is necessary to distinguish between three types of Al atoms: (i) Electrically active Al on substitutional sites ( $\text{Al}_{\text{sub}}^-$ ), (ii) electrically non-active Al on substitutional sites ( $\text{Al}_{\text{sub}}^0$ ) and (iii) Al on non-substitutional sites, such as on interstitial sites and at grain boundaries ( $\text{Al}_x$ ). In addition to these three types of incorporated Al, the Al clusters trapped at the glass/poly-Si interface (see chapter 5.1) have to be taken into account. The observation that the carrier concentration increases after the post-treatment indicates that  $\text{Al}_x$  atoms and/or Al atoms from Al clusters could be activated by additional heat-treatment at 500°C to occupy lattice sites. The additional Al atoms on substitutional sites contribute to the measured hole concentration. Remarks on the quantitative relationship between  $\text{Al}_{\text{sub}}^0$ ,  $\text{Al}_{\text{sub}}^-$  and  $\text{Al}_x$  are given in the next section.

### 5.3.3 Substitutional and non-substitutional Al concentration

Whilst the measured hole concentration is equal to the ionised Al atoms on substitutional sites,  $\text{Al}_{\text{sub}}^-$ , the SIMS results presented in chapter 5.1 give the total amount of Al in the poly-Si material  $\text{Al}_{\text{tot}}$ . To compare the Hall-effect measurements with the SIMS result it is necessary to calculate the total concentration of Al atoms on substitutional sites,  $\text{Al}_{\text{sub}}$ . To estimate the ratio of Al atoms on substitutional sites to the ones on non-substitutional sites it is firstly necessary to extract the Fermi energy using the following relationship [94]:

$$p = \int_{-\infty}^0 \rho_v(E)[1 - f(E)]dE \quad (3)$$

$\rho_v(E)$  is the density of states in the valence band and  $f(E)$  the Fermi distribution. The valence band edge is set equal to zero. Assuming a parabolic band structure of the valence band, equation (3) transforms into

$$p = \frac{1}{2\pi^2} \left( \frac{2m_{dv}}{\hbar} \right)^{1.5} \int_{-\infty}^0 \frac{\sqrt{-E}}{e^{(E_F - E)/kT} + 1} dE \quad (4)$$

with  $m_{dv}$  being the valence-band density-of-states effective mass,  $E_F$  the Fermi level,  $\hbar$  the reduced Planck constant and  $k$  the Boltzmann constant. Since the free carrier concentration revealed in section 5.3.1 is high, the following analysis refrains from approximating the Fermi distribution by the Boltzmann distribution to avoid inconsistencies due to degeneration effects of the highly doped poly-Si material. Defining the Fermi integral as

$$F_{1/2}(\eta) = \frac{2}{\sqrt{\pi}} \int_0^{\infty} \frac{\sqrt{x}}{e^{(x-\eta)} + 1} dx \quad (5)$$

and substituting

$$x = -\frac{E}{kT} \quad \text{and} \quad \eta = -\frac{E_F}{kT} \quad (6)$$

equation (4) can be written as

$$p = N_v \cdot F_{1/2}[-E_F / kT] \quad (7)$$

with

$$N_v = 2 \left( \frac{m_{dv} kT}{2\pi\hbar^2} \right)^{1.5} \quad (8)$$

Green gave for the effective density of states the value [95]

$$N_v = 3.10 \times 10^{19} \text{ cm}^{-3} \quad (9)$$

by using his reassessed value for the valence-band density-of-states effective mass at  $T = 300$  K. Measuring the free carrier concentration and using Fermi integral tables, equation (7) allows to extract the Fermi energy [96]. In the specific case analysed, the value of the free carrier concentration  $p$  is set to  $2.5 \times 10^{18} \text{ cm}^{-3}$  according to the Hall effect measurements of the poly-Si material formed at  $500^\circ\text{C}$  (see chapters 5.3.1 and 5.3.2), and it follows that  $E_F$  equals  $65 \pm 2$  meV. The error stems from variations in the determined hole concentration.

The free carrier concentration is equal to the negatively ionised Al atoms on substitutional Si lattice site. For the time being, counter-doping due to impurity incorporation such as oxygen is neglected. The ratio  $x$  of the substitutional, ionised Al atoms  $\text{Al}_{\text{sub}}^-$  to the total amount of substitutional Al atoms  $\text{Al}_{\text{sub}}$  is determined by the following relationship [57]

$$x = \frac{\text{Al}_{\text{sub}}^-}{\text{Al}_{\text{sub}}} = \frac{1}{g \cdot e^{(E_A - E_F)/kT} + 1}. \quad (10)$$

$E_A$  is the activation energy and  $g$  is the ground-state degeneracy factor, which equals 4 for acceptor levels in Si. Using the value determined in chapter 5.3.1 ( $E_A = E_x = 54 \text{ meV}$ ) as the activation energy and a Fermi level of 65 meV, the ratio  $x$  can be calculated to be 0.28. Consequently, only about 30% of the Al atoms on substitutional sites are ionised and therefore contribute to the free carrier concentration of the poly-Si at room temperature. Using equation (10) the total amount of Al atoms on lattice sites can be determined:  $\text{Al}_{\text{sub}} = (1.0 \pm 0.5) \times 10^{19} \text{ cm}^{-3}$ . The large error is based on calculations using the upper and lower limit for the activation energy. The upper limit is calculated with the value of the activation energy of Al in only lightly doped silicon, which is 67 meV [57]. The lower limit is determined by assuming compensation from incorporated oxygen. Furthermore, it is likely that an Al impurity band is formed in the energy band structure of the highly doped poly-Si material. It is unknown whether influences of this Al band can be entirely neglected even at room temperature. Nevertheless, the comparison of the total amount of Al as revealed by SIMS with the concentration of Al on substitutional sites as extract from Hall effect measurements shows that both results are of the same order of magnitude.

The discussion above shows the importance of distinguishing between ionised, neutral and non-substitutional Al incorporated in the poly-Si material. In the literature are numerous examples that omit this distinction. For example Gudmundsen and Maserjian determined the solid solubility of Al in silicon at temperatures between 600 and 1000°C by assuming that all aluminium acceptors are completely ionised [97]. Trumbore pointed out that their data were too low by a factor of 2 or 3 compared to his measurements [56]. He resolved this discrepancy by reinterpreting their resistivity measurements using a different set of mobility data. However, as shown above, in highly doped semiconductors the assumption that all acceptor atoms are ionised is not valid anymore. Taking this into account, Gudmundsen and Maserjian's results can be adjusted within the framework of

their measurements. Another study related to the issue of setting the  $Al_{sub}^-$  concentration equal to the total amount of Al atoms in the crystallized poly-Si material is by Tsauro et al. [53]. Their investigation on the process of aluminium-induced solid-phase epitaxy of a-Si on top of an n-type Si wafer revealed the growth technique of highly doped p-type emitter layers for solar cell fabrication. The hole concentration of these layers was measured to be  $2 \times 10^{18} \text{ cm}^{-3}$  when the film was formed at  $500^\circ\text{C}$ . This value is in good agreement with the results presented above. A post-annealing treatment at  $900^\circ\text{C}$  increased the free carrier concentration to  $2 \times 10^{19} \text{ cm}^{-3}$ . Tsauro et al. set this value equal to the solid solubility of Al in silicon. The validity of this step has not been discussed.

**Summary:** The polycrystalline Si films are p-type with a doping concentration of about  $2 \times 10^{18} \text{ cm}^{-3}$  due to the incorporation of Al atoms as acceptors on substitutional lattice sites. Keeping the doping concentration in mind the hole mobility with values exceeding  $54 \text{ cm}^2/\text{Vs}$  can be considered as high. It seems that grain boundaries do not have a major influence on the electrical properties of the majority carriers. The doping concentration decreases slightly with lower crystallization temperatures. To achieve doping concentration as high as in the poly-Si material investigated, about three times as many Al atoms have to occupy lattice sites since only 30% are ionised even at room temperatures.



# Chapter 6:

## Model of the layer exchange process

The study so far concentrated on the process parameters that influence the aluminium-induced layer exchange and the characterisation of the continuous high-quality polycrystalline silicon films formed during the process. In this chapter a model will be developed, which is based on the results of the previous investigations. The layer exchange process is driven by aluminium-induced crystallization (AIC) of amorphous silicon. AIC can be sequentially analysed by initially discussing the dissociation and diffusion of the a-Si material at low temperatures when in contact with Al, followed by the nucleation and grain growth of the polycrystalline Si. This general process description is supported by the results presented in this work but is also in agreement with numerous other studies in this field [41,46,47,50,51,98-100]. However, the individual sub-steps of aluminium-induced crystallization have been discussed controversially in the literature, and no model for the Al-induced layer exchange has been given as yet. The discussion in this chapter begins with an analytical view of the overall layer exchange process, which can be seen as an introduction to the following analysis. This introduction gives the reasoning as to why particular process steps are discussed in more detail in the subsequent chapters. These subchapters deal with the Al/a-Si interface interaction, the question of why a-Si dissolves and yet poly-Si is formed, and finally the interference process of growing Si grains that leads to large-grained poly-Si formation. A discussion of the model presented will close this chapter.

### 6.1 The overall layer exchange

The first insight into the layer exchange process can be gained when extracting the total thermal activation energy from optical microscopy investigations. This in-situ study enabled the observation of the formation process of the poly-Si film in real-time due to the lower reflectivity of Si grains within the highly reflective Al matrix. The time dependent

increase of the crystallized fraction with the annealing temperature as the varying process parameter is shown in Fig. 43a. The time needed for the formation of 50 % ( $t_{1/2}$ ) of the poly-Si film was analysed in an Arrhenius-plot, as shown in Fig. 43b. The plot revealed that the overall activation energy of the aluminium-induced layer exchange is  $1.3 \pm 0.1$  eV. This value was independent whether the time needed for 20, 50 or 90 % completion of the poly-Si film was used for the analysis.

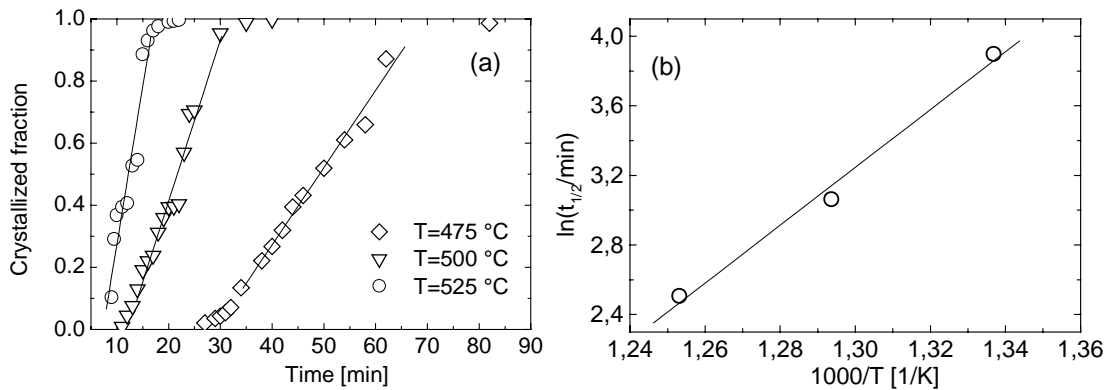


Fig. 43: Analysis of in-situ optical micrographs taken during isothermal annealing at different temperatures, (a) fraction of crystallization with linear fits to data points of crystallization between 10 % and about 90 %, (b) Arrhenius-plot of the temperature dependence of the time needed for 50 % crystallization ( $t_{1/2}$ ).

It has to be taken into account that the activation energy extracted stems from measurements of identical pieces of a "standard sample". This means that 0.4  $\mu\text{m}$  Al was evaporated directly onto glass at a rate of 2-3 nm/s, and the Al was exposed to air for 24 h prior the deposition of 0.5  $\mu\text{m}$  a-Si. It was shown in the previous chapters that a whole set of process parameters influences the layer exchange. Nevertheless, the activation energy as extracted for the standard sample is in good agreement with an activation energy of 1.2 eV stated by Konno and Sinclair in their study on aluminium-induced crystallization [47]. The comparison of the value extracted in this study with the activation energy of solid phase crystallization (SPC) of pure a-Si, which is about 3-4 eV [101], shows that aluminium-induced crystallization is of a significantly different nature than SPC. This difference is apparent from the simple comparison of the activation energies without going into the details of the actual crystallization process. Possible explanations as to why the activation energy for the transformation of the amorphous to the crystalline Si phase is reduced due to Al will be given in the following chapters.

The thermal activation energy of ALILE lies within the range for Si diffusion in Al. McCaldin and Sankur stated activation energies of 0.79 eV - 1.36 eV for Si diffusion in

evaporated and wrought Al [102]. It therefore seems to be a reasonable assumption that the Si diffusion within the Al is a dominant step in the overall layer exchange process. However, possible differences in the structure of the polycrystalline Al and the Al/Si interface have to be taken into account when comparing the values of the activation energies. McCaldin and Sankur did not give any details concerning the Al deposition or its polycrystalline structure.

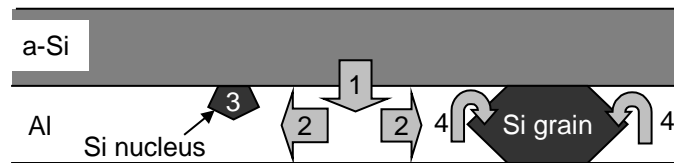


Fig. 44: Schematic diagram of the dissociation, diffusion and crystallization processes that lead to the layer exchange and formation of the poly-Si material. The steps 1 to 4 are explained in the text.

To facilitate the analysis of the aluminium-induced layer exchange, the overall process can be separated into 4 steps as shown in Fig. 44. Step 1 involves the interaction of amorphous silicon with Al and the dissociation of the amorphous phase through the Al/Si interface. This part of the process will be discussed in chapter 6.2. Once Si is dissolved in the metal, the Si atoms can diffuse rapidly within the evaporated Al (step 2). Since the evaporated Al films are of polycrystalline nature, there are four different diffusion paths available: (a) Diffusion inside the Al grains, (b) diffusion along Al grain boundaries, (c) diffusion along the Al/a-Si interface, and (d) diffusion along the glass/Al interface. Diffusion paths (b) and (c) are highly dependent on the deposition parameters and only a net diffusion rate can be observed [103]. McCaldin showed that the diffusivity of Si in Al is about of  $10^{-8} \text{ cm}^2\text{s}^{-1}$  when dealing with temperatures between  $400^\circ\text{C}$  and  $500^\circ\text{C}$  [104]. Step 3 in Fig. 44 represents the nucleation of Si atoms. It will be suggested in chapter 6.3 that this nucleation occurs, because the Al film undergoes a supersaturated state during the layer exchange process. The Si grains continue to grow due to continuous dissolution of a-Si, diffusion of Si solute and incorporation of dissolved Si atoms (step 4). The Si grain growth process will be discussed in chapter 6.4 with an emphasis on the interference of neighbouring grains at an early stage of the poly-Si formation process.

**Summary:** The Al-induced layer exchange is a thermally activated process with an activation energy of  $1.3 \pm 0.1 \text{ eV}$ . This activation energy is very low compared to common solid phase crystallization and indicates that the process mechanisms of ALILE are different from the ones of SPC. The overall layer exchange process was subdivided into 4 basic steps, which were (i) the

dissociation of a-Si by the Al, (ii) the diffusion of the Si solute within the metal, (iii) the nucleation of the Si within the Al, and (iv) the Si grain growth through continuous incorporation of the diffusing Si atoms.

## 6.2 Interface interaction

The interface of the layered Al/a-Si structures consists of an oxide layer that remains at the interface throughout the layer exchange process as revealed by the XPS investigations of chapter 4.5.2. This oxide layer has to be dealt with, before any discussion of the metal/a-Si interaction can follow. The Si/Si-oxide/Al structure has been extensively investigated due to its application in metal-insulator-semiconductor devices. The Al is known to reduce Si-oxide to form Al-oxide due to the stronger Al-O bond compared to Si-O bond [105-107]. The formation enthalpies of  $\text{SiO}_2$  and  $\text{Al}_2\text{O}_3$  are  $-0.9$  MJ/mol and  $-1.7$  MJ/mol, respectively [108]. The reduction process, for example, gives rise to the problem of "Al spike"-formation in Al/ $\text{SiO}_x$ /p-Si tunnel diodes. Bierhals et al. concluded from their infrared spectroscopy investigation of MIS structures that the formation of Al spikes involves three different processes [109]: (i) the reduction of the tunnel oxide by the Al film, (ii) the diffusion of Al through the insulator, and (iii) the formation of conducting paths (Al spikes) through the tunnel insulator. The instability of the oxide layer leads to the degradation of the device performance. The overall degradation process is summarised in Fig. 45.

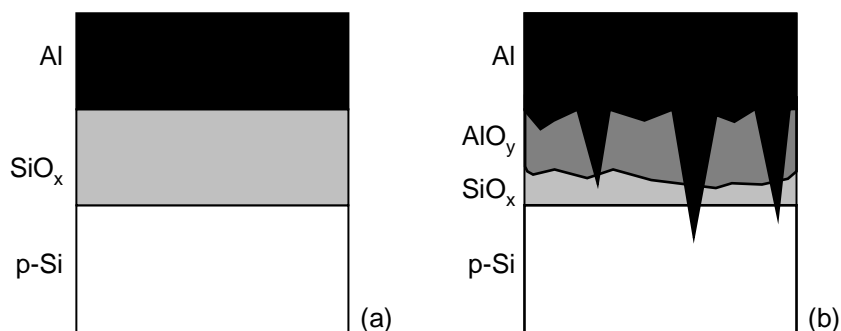


Fig. 45: Schematic representation of the formation of Al spikes in Al/Si oxide/c-Si structures according to the model proposed by Bierhals et al. [109]; (a) the initial structure and (b) the structural changes after annealing at elevated temperatures ( $\sim 300^\circ\text{C}$ ).

Kim and Lee conducted cross-section TEM investigations of glass/a-Si/ $\text{SiO}_2$ /Al structures to analyse the process mechanism at an oxidised interface during aluminium-induced crystallization [98]. They revealed that the oxide is locally dissociated by Al and

proposed that, on one hand,  $\text{Al}_2\text{O}_3$  was formed, and, on the other hand, Si-Al intermixed phases developed at these local sites. The interface oxide can therefore not be treated as a continuous and homogenous layer. It acts rather like a membrane that allows the local interaction of the metal and the amorphous silicon due to the reduction of the oxide and the formation of Al spikes. The oxide itself is known to be a successful diffusion barrier [110]. Although the discussion, so far, concerns glass/a-Si/Al structures, where a Si oxide layer initially separates the two films, the hypothesis of an inhomogeneous oxide layer can be extended to glass/Al/a-Si structures with an Al oxide at the interface. The fact that in both types of structures a layer exchange occurs proves that an interaction of the Al and a-Si layers is possible independent of the initial type of interface oxide.

Ottaviani and Majni studied the influence of an Al oxide layer on solid phase epitaxy of amorphous silicon onto crystalline Si wafers [111]. They suggested that the oxide layer acted as a diffusion barrier on the Al atoms, but allowed the Si atoms to diffuse into the metal layer with subsequent crystallization. However, they did not investigate where the Al oxide layer is located after the SPE process. Their model of a one-way diffusion barrier is not in agreement with the results presented in this study. Based on the XPS measurements in chapter 4.5.2, strong evidence is given that the Al oxide remains at the interface and that a migration of Al and Si material in opposite directions is possible in spite of the interface oxide. Consequently, the oxide layer ought to consist of a structure that allows this material transport to happen. An inhomogeneous membrane-like structure is therefore suggested for the Al oxide interface layer.

As mentioned previously, the diffusion of the Si atoms through the metal of a simple eutectic metal/Si system and subsequent crystallization have widely been accepted as the basic processes of metal-induced crystallization. Nevertheless, little is known about the actual dissociation mechanism of the amorphous silicon by the metal. The overall driving force behind the crystallization process is the reduction of Gibbs energy by the transformation of amorphous to crystalline silicon ( $\sim 0.1$  eV/atom [19]). However, the covalent Si-Si bond is relatively strong with about 2 eV per bond. The overall activation energy of solid phase crystallization (SPC) of pure a-Si material is therefore high with about 3-4 eV [101]. This causes the formation of poly-Si by SPC to be slow even at temperatures above 600°C [86]. In contrast, the crystallization of a-Si when in contact with Al occurs at much lower temperatures, is faster, and has a lower activation energy. The reported activation energy for Al-induced crystallization varies between 0.8 eV and 1.2 eV as stated by Qingheng et al. according to their measurement on solid phase epitaxy [112]

and Konno and Sinclair in their study on Al/a-Si multilayer interaction [47], respectively. The activation energy for the aluminium-induced layer exchange process is 1.3 eV as determined in the previous chapter.

The question is therefore, how the metal reduces the energy required to break the Si-Si bonds prior to any diffusion process. There are two main models that propose a dissociation mechanism of the amorphous silicon in spite of the covalent Si bonding: (i) Tu's "interstitial model" [113] and (ii) Hiraki's "screening model" [114]. Tu's model is based on an initial intermixing of the metal and the Si atoms at the interface. It is proposed that the metal atoms *jump* into the Si, forming metal interstitials. These interstitial defects in the Si structure are expected to considerably change the nature of the neighbouring Si-Si bonds. The covalent bonds will no longer remain in their localised state. The metal interstitial therefore induces the conversion from the covalent Si-Si bond of the neighbouring Si atoms to a non-covalent bond. This altered bond is weaker than a saturated covalent bond. Tu argues that the Si atoms can dissociate themselves from the lattice at a reduced activation energy and diffuse into the metal. However, the initial formation of the metal interstitials is not specified as such. Although Tu suggested his model for silicide forming metal/Si interfaces (Ni-Si, Pd-Si and Pt-Si), the interstitial model was also adapted to explain studies on metal/a-Si interfaces of simple eutectic systems, e.g. the Au/Si [36] and the Al/Si-system [115].

Hiraki's screening model, on the other hand, does not rely on unspecified initial jumping of metal atoms into the Si structure. He postulates that the weakening of the covalent Si-Si bonds at the metal/Si interface is due to the ability of the metal to screen the Coulomb interaction by its mobile free electrons. This screening effect results in a transition of non-metal to metal-like bonding of the adjacent semiconductor material over the region of a few monolayers at the interface [116]. This region is characterised by the formation of a nearly uniform electron gas. The valence electrons of the Si in this region are not associated with specific atoms anymore. Hiraki's model is based on calculations by Inkson and Anderson on the band closure of the energy band gap of covalent semiconductors applying many-body techniques to interface calculations [117,118]. The arguments of the band closure are also supported by the analysis of Okiji et al. [119], who concluded that the covalent non-metallic state of an insulator became metallic due to band gap closure at the insulator/metal interface.

The atomic mobility in a covalent semiconductor is low compared to the mobility in metals. The resistance against atomic motion in metals is predominantly due to atomic size effects and the crystallographic structure of the films (defects, grain boundaries and so on). The electron gas of a metallic-like compound does not restrict the atomic motion as strongly as the electron configuration of a covalent semiconductor material. The atoms of a metallic-like, transformed semiconductor region near the metal interface are therefore more mobile than atoms of the bulk area.

Hiraki's screening model is strongly supported by the analysis of monolayer by monolayer growth of Au onto clean silicon surfaces. The results reveal that a critical Au layer thickness (4 monolayers) has to be deposited, before any interface reaction between Si and the metal occurs [114,116]. If the Au layer is thinner than the critical thickness, it acts rather like a non-metal than a metal. Even during the heating of 1-2 monolayer thick Au films up to 800°C, the metal does not react with the adjacent Si material. However, an Au layer thicker than the critical thickness already reacts at room temperature with Si. The first couple of metal layers on the Si surface are bonded in a covalent rather than a metallic way [120]. In thicker Au layers (>3 monolayers) the metallic free electron system can establish and, consequently, induce instability of the covalent Si-Si bonding mentioned above. Evidence for a critical metal layer thickness to induce crystallization was also given by Radnoczi et al. [121]. They showed that a minimal Al layer thickness (3 or more monolayers) is mandatory to cause crystallization of a-Si at a temperature of about 170°C.

Once the dissociation process of the amorphous silicon material is facilitated, an exothermic intermixing process can take place. Walser and Bené suggested that at the immediate interface a *metallic glass* is formed [122], which reduces the energy of the interface system faster [123]. The metallic glass is seen as a transition phase before any silicide formation occurs. Even for simple eutectic systems such as the Al/Si and Au/Si some evidence has been given that a metastable metal silicide is formed near the interface prior to any nucleation of crystalline Si [36,41,124,125]. Ashtikar and Sharma showed that the metastable Al silicide decomposes completely at temperatures above 300°C [41]. However, Konno and Sinclair did not find any evidence of silicide or liquid phase formation prior to the diffusion of the Si atoms into the Al and subsequent crystallization [47]. They conducted in-situ TEM-investigations of the crystallization of silicon in Al/a-Si multilayer systems at 200°C. Thus, the initial reaction between metal and a-Si at the interface is still controversially discussed.

**Summary:** Any model describing the interaction of Al and a-Si has to account for the dissociation of the a-Si through the interface oxide layer and the reduction of activation energy compared to SPC. It is suggested that the oxide is of an inhomogeneous, membrane-like structure, through which a dissociation process is still possible. The fact that the Al greatly facilitates the a-Si dissociation has been discussed according to Hiraki's screening model. The atomic mechanisms of the direct interaction between the Al and the a-Si at the interface, however, remain unknown and ought to be subject to future investigations.

### 6.3 Crystallization

In the last chapter, possible dissociation processes of the a-Si were discussed. Once the Si atoms are dissociated from the amorphous phase, the Si diffuses rapidly into and within the Al layer [104]. According to the binary phase diagram of the Al/Si system, shown in Fig. 46, up to 1.5 at.% Si atoms can dissolve in Al at temperatures below the eutectic temperature of 577°C [40]. The solid solubility of Si in evaporated Al is 0.2 at.% and 0.8 at.% at 400°C and 500°C, respectively [102]. Consequently, the pure Al in contact with a-Si is not a system in a state of thermal equilibrium. During the annealing process a solid Al solution with Si solute develops. The question is: Why does amorphous Si dissolve and

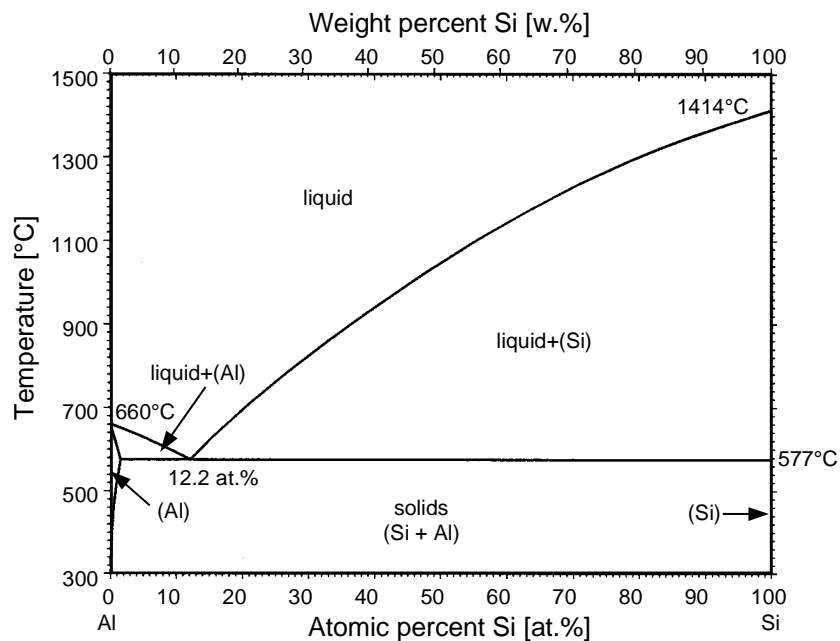


Fig. 46: Phase diagram of silicon and aluminium [40].

yet stable crystalline silicon grow from this solution? The reason for this one-way action of taking the amorphous phase completely apart and putting it back together in a crystalline form could be that the Al undergoes a state of Si supersaturation during the crystallization process. The possibility of this explanation is analysed in the following discussion, which is an extension of Konno and Sinclair's analysis of multilayer systems consisting of stacked, 6 nm thin Al and a-Si films [47].

The reason for a supersaturated Al solution lies in the difference in Gibbs energy,  $G$ , of the stable crystalline compared to the metastable amorphous silicon phase. To elaborate in more detail on the circumstances of this supersaturation, the partial molar Gibbs energy,  $g_i$ , of a component  $i$  will be used.  $g_i$  is also known as the chemical potential,  $\mu_i$ , and is defined as [126]:

$$g_i = \left( \frac{\partial G}{\partial n_i} \right)_{T,p,n_j} \quad (11)$$

where  $n_j$  is the number of moles of component  $j \neq i$ ,  $T$  the temperature and  $p$  the pressure. In this discussion Si is the only component of interest, the index  $i$  will therefore be dropped from now on. The difference of the amorphous to the crystalline Si phase can be expressed in terms of excess Gibbs energy:

$$g^E = g^{a-Si} - g^{c-Si} = h^E - Ts^E \quad (12)$$

with  $g^{a-Si}$  and  $g^{c-Si}$  being the molar Gibbs energies of the amorphous and the crystalline phase, respectively.  $h^E$  is the molar excess enthalpy and  $s^E$  the molar excess entropy. The excess Gibbs energy is related to the activity,  $a$ , as follows [126]:

$$g^E = RT \ln a \quad (13)$$

where  $R$  is the molar gas constant. Using equations (12) and (13) the activity can be calculated when  $h^E$  and  $s^E$  are known quantities. The molar excess enthalpy of a-Si in relation to c-Si can be taken as the enthalpy of crystallization, measured by Dononvan et al. to be 11.9 kJ/mol [127]. The excess entropy was determined by Spaepen to be 1.66 J/(mol K) [128]. Using these values, the activity of a-Si relative to crystalline silicon as the standard state can be calculated to be 6 at 475°C. The activity can now be used to estimate a possible supersaturation of Al with Si solute when in contact with a-Si. For this, the Al/a-Si system is hypothetically regarded to be in thermal equilibrium omitting any Si nucleation.

When a system is in thermal equilibrium, the chemical potential - the partial molar Gibbs energy - of one component is the same in all phases. For the following discussion, each of the Al/a-Si and Al/c-Si systems are assumed to be in thermal equilibrium. The chemical potentials of the Si atoms in each phase of the individual systems are therefore equal:

$$g^{c-Si} = g^{Al/c-Si} \quad \text{and} \quad g^{a-Si} = g^{Al/a-Si} \quad (14)$$

where  $g^{Al/c-Si}$  and  $g^{Al/a-Si}$  denotes the chemical potential of Si in Al when in contact with crystalline and amorphous silicon, respectively. The difference between the chemical potential of c-Si and a-Si is the excess molar Gibbs energy  $g^E$  according to equation (12). Because of equation (14) the difference between  $g^{Al/c-Si}$  and  $g^{Al/a-Si}$  is of the same value,

$$g^{Al/a-Si} = g^{Al/c-Si} + g^E. \quad (15)$$

Fig. 47 shows a schematical diagram of the partial Gibbs energies at the a-Si/Al interface in relation to the Al/c-Si interface when both are hypothetically in thermal equilibrium. During the Al-induced layer exchange the entire a-Si/Al/c-Si system with the dissociation of Si at the a-Si/Al interface and the crystallization at the Al/c-Si interface has to be considered. Because the partial Gibbs energy, i.e. the chemical potential of silicon, is not equal throughout the system, the entire system is in a non-equilibrium state. The system will therefore try to level the chemical potentials of the Si. It will be discussed in the next chapter that this is done via Si diffusion from the a-Si/Al to the Al/c-Si interface.

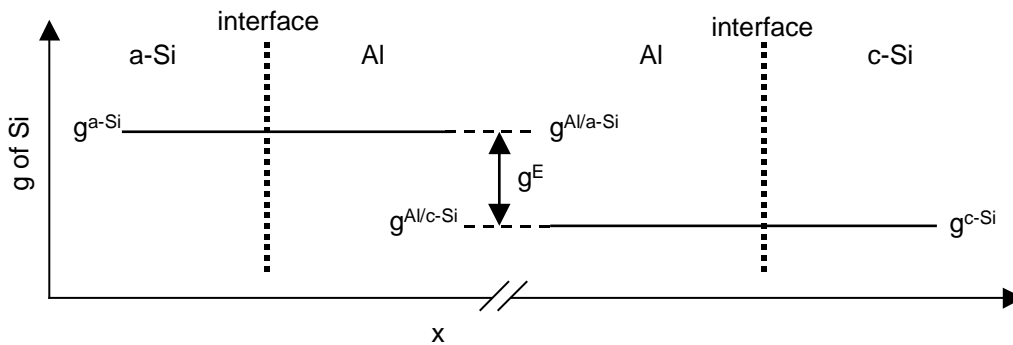


Fig. 47: Partial Gibbs energy of Si at the a-Si/Al and the Al/c-Si interface versus position  $x$ . Both interfaces are set to thermal equilibrium. The difference between the chemical potentials of the two systems is the excess Gibbs energy  $g^E$ .

The chemical potential of a dissolved component is related to its concentration in the solvent. The assumption is made that the Al regions with a low concentration of Si solute near the interfaces behave like ideal-dilute solutions. In an ideal-dilute solution the chemical potentials of a dissolved component  $i$  is [129]:

$$g_i = g_i^* + RT \ln X_i \quad (16)$$

where  $g_i^*$  is a standard chemical potential and  $X_i$  is the relative concentration of the solute. Using equations (15) and (16), the following relationship for Si solute in a dilute Al solution is obtained:

$$g^* + RT \ln X^{Al/c-Si} + g^E = g^* + RT \ln X^{Al/a-Si} \quad (17)$$

where  $X^{Al/c-Si}$  and  $X^{Al/a-Si}$  are the Si concentrations in Al when in contact with c-Si and a-Si, respectively. From this equation in combination with equation (13) the two concentrations can be related by the activity:

$$X^{Al/c-Si} a = X^{Al/a-Si} \quad (18)$$

When the Al/c-Si system is in thermal equilibrium, the phase diagram determines the Si concentration in the Al. The solid solubility of Si in Al at 475°C is about 0.5 at.% [130]. Since an activity of 6 has been calculated above, it can be determined that  $X^{Al/a-Si}$  equals 3 at.% when using equation (18).

The conclusion from the above analysis is that if Al was not subject to a solid solubility limit, meaning no nucleation could occur, the Si concentration of Al in contact with a-Si would be 3 at.% when brought into thermal equilibrium at 475°C. This Si concentration exceeds the maximal solid solubility of Si in Al as apparent from Fig. 46. Considering the Al/c-Si system, the Al with such high Si concentration is in a supersaturated state. In reality this supersaturation is released by nucleation and growth of crystalline silicon grains within the Al. It is unknown whether a concentration of 3 at.% at 475°C, as an upper limit, is reached or whether crystallization already takes place at a state of lower concentration. Nevertheless, throughout the crystallization process the amorphous Si phase adds Si atoms to the Al solution to increase the chemical potential of the Si solute, whilst the growing crystalline Si phase is extracting Si to decrease this chemical potential. The aluminium is therefore in a state of undersaturation in relation to the a-Si and a state of supersaturation in relation to the c-Si. This difference serves as an explanation for the one-way action of dissociation of a-Si and yet formation of c-Si.

Evidence was given in earlier chapters (e.g. Fig. 12 of chapter 4.1 and Fig. 34 of chapter 5.2) that at lower temperatures dendritic growth behaviour of the Si grains is prevalent. In general, dendritic growth occurs when a system is in an unstable supersaturated state. In this case the system does not necessarily transform to reach the state of lowest Gibbs energy directly but it changes along the path that allows the fastest reduction in Gibbs

energy [123]. This is the reason why snowflakes are formed instead of small balls of ice. Regarding the Al/a-Si system, it follows from equation (13) that the lower the annealing temperature, the higher the activity of the Si atoms. Using equations (12) and (13), the activity of Si at 400°C, for example, is 7. According to the analysis presented, the lower the temperature the higher the supersaturation of the Al solution with Si solute. This state of higher supersaturation only implies that the ratio of  $X^{\text{Al/a-Si}}$  to  $X^{\text{Al/c-Si}}$  is higher. Quantitatively,  $X^{\text{Al/a-Si}}$  is lower at 400°C (1.4 at.%) than at 475°C, since  $X^{\text{Al/c-Si}}$  is only 0.2 at.% at the lower temperature [102]. This consequence of stronger supersaturation with decreasing temperature is in agreement with the observation of enhanced dendritic growth at lower temperatures and supports the model of a supersaturated transition state of the solid Al solution during the aluminium-induced layer exchange.

The nucleation of Si from the supersaturated Al solution does not occur homogeneously since the evaporated Al is of polycrystalline nature. The Al grain boundaries and the triple junctions of grain boundaries with the Al/a-Si interface are sites of lower critical energy for the nucleus formation than bulk Al. At these sites preferential Si nucleation occurs. Evidence for the preferential nucleation was given in Fig. 7b of chapter 4.1, where a Si nucleus at a Al grain boundary/a-Si interface was shown. Additionally, chapter 4.4 revealed the dependence of the Si nucleation rate on the Al grain size. The smaller the grain size, thus, the higher the grain boundary density, the higher the Si nucleation rate. The relationship between nucleation rate and grain boundary density is in agreement with the standard theory on grain formation and growth [68].

**Summary:** The dissociation of a-Si and the formation of crystalline Si grains are driven by the difference between the chemical potentials of the two states. The metastable state of a-Si when in contact with Al leads to a supersaturation of the metal with Si atoms. Considering the Al as a solid solution, an upper limit of Si concentration in the supersaturated state was calculated to be 3 at.% at 475°C. The supersaturation is released by the nucleation and growth of crystalline Si. The difference between the chemical potentials at the a-Si/Al and the Al/c-Si interfaces provides a constant driving force for the dissociation, diffusion and crystallization process.

## 6.4 Si grain growth

The discussion presented so far addressed how Si atoms dissociate from a-Si into aluminium and why Si atoms are transferred from the amorphous to the growing crystalline Si phase. This chapter analyses the growth behaviour of large-grained poly-Si material during the aluminium-induced layer exchange process.

When amorphous silicon is crystallized using solid phase crystallization, individual grains grow until they impinge. Prior to the impingement the growing grains increase their size independently from each other. The growth behaviour and the nucleation are not affected by already existing grains. The same characteristics are valid for the crystallization of Si from a liquid phase formed by laser crystallization. This is one of the fundamental differences in the formation of poly-Si material via an aluminium-induced layer exchange process. In chapter 4.1 (see Fig. 9 and Fig. 10) evidence was given that at an early stage of the crystallization process, existing grains suppress the formation of new nuclei. This suppression can be interpreted as an interference of growing grains with the Al matrix, as will be explained in the following discussion.

To form crystalline Si thin-films, the ideal process would be the nucleation of one grain that grows until the entire amorphous phase is transformed. Based on this idealisation, the following general rule for the formation of large-grained poly-Si films can be derived: The fewer nuclei are formed, the larger the grains can grow before impingement occurs.

The initial state of the Si solute in the Al solvent prior to any nucleation has to be analysed, before the interference of Si grains at an early stage of the Al-induced layer exchange can be discussed. It was argued in chapter 6.3 that, when Al is in contact with a-Si at a temperature of 475°C, Si atoms can dissolve up to the supersaturation concentration  $c_s$  of about 3 at.% at the Al/a-Si interface according to thermodynamic considerations. The dissolved Si atoms diffuse quickly into the Al matrix. The concentration profile  $c(x,t)$  of the Si solute from the interface into the aluminium, dependent on the position  $x$  and the time  $t$ , is determined by the diffusivity  $D$  as follows [68]:

$$c(x, t) = c_s - (c_s - c_0) \cdot \operatorname{erf}\left(\frac{x}{2\sqrt{D \cdot t}}\right) \quad (19)$$

with  $c_0$  the Si concentration far away from the interface, and 'erf' stands for error function. Equation (19) is the analytical solution of Fick's second law assuming that the diffusivity is

independent of the concentration and setting the boundary conditions  $c(0,t) = c_s$  and  $c(\infty,t) = c_0$ . Fig. 48 shows how the concentration profile from the a-Si/Al interface into the adjacent Al matrix changes according to equation (19) with elapsing time. The Si diffusivity is set to  $10^{-8} \text{ cm}^2/\text{s}$  as given by McCaldin and Sankur for Al in the temperature range discussed in this work. The concentrations  $c_0$  and  $c_s$  equal 0 and 3 at.%, respectively.

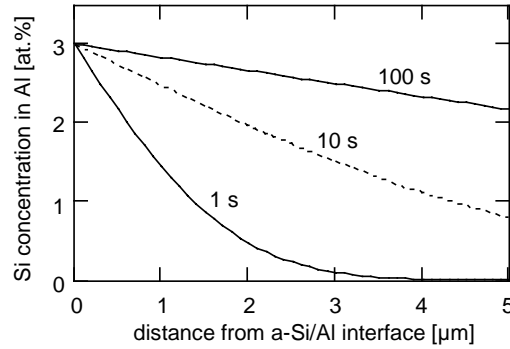


Fig. 48: Si solute concentration profile from the a-Si/Al interface into the Al solvent after 1 s, 10 s and 100 s calculated using equation (19). The Al matrix is assumed to be a semi-infinite volume and the interface concentration is kept constant at the supersaturation concentration of 3 at.%.

Considering that the default sample structure prepared for this study of ALILE consisted of  $0.4 \mu\text{m}$  thick Al films, it becomes apparent from Fig. 48 that the dissolved Si atoms are almost homogeneously distributed over the entire Al matrix at a very early stage of the process. The homogeneous Si distribution is disrupted as soon as the supersaturation of the Al with Si solute is released by Si nuclei formation. The crystalline Si phase depletes the surrounding Al of Si solute.

The interference of neighbouring Si grains can be understood when ALILE is regarded as a diffusion-controlled process, as will be shown in the following discussion. The discussion focuses on the development of the Si concentration in the Al solvent between two neighbouring grains. The entire analysis is reduced to two dimensions, since the Si grain sizes exceed the Al layer thickness many times as documented by the results presented throughout the previous chapters. The first assumption made is that the Si concentration in the Al matrix far away from any crystalline Si grains is kept constant at the supersaturation concentration  $c_s$  due to the continuous supply of Si atoms from the amorphous Si film in contact with the Al layer. At the supersaturated state, Si nucleation will occur. The following Si grain growth is confined between the Al/a-Si interface and the glass substrate (see chapter 4.1). The Si grains are regarded as cylinders with their rotation axis vertical to the interface. The radius  $r$  of these cylinders increases with time, since Si

atoms near growing grains are incorporated into the advancing crystalline Si structure to decrease their Gibbs energy. The incorporation is assumed to be fast in comparison to the diffusion processes because of the incoherent interface between the Al matrix and the Si crystal [131]. In the vicinity of the grains, the Si solute is therefore depleted and the concentration  $c_i$  of Si atoms at the Si grain/Al interface is lower than  $c_s$ . Consequently, a concentration gradient establishes from the c-Si/Al interface extending into the Al matrix. This gradient induces the diffusion of Si solute towards the Si grains. The Si diffusion within the Al matrix is the process mechanism that aims to equalise the chemical potentials of the Si solute at the c-Si/Al and the Al/a-Si interfaces, presented in chapter 6.3.

Fig. 49 describes the development of the concentration profile between two neighbouring grains that are growing towards each other with velocity  $v$ . The diagram of Fig. 49a shows the situation at an early stage of the crystallization process. The grains are still far apart, and if no additional nucleation occurs, the concentration between grain 1 and 2 is constant  $c_s$ , except in the Si depletion regions near the interfaces. The concentration profiles in these regions can be simplified using Zener's one-dimensional linear gradient approximation [132]. The concentration profile between grain 1 and 2, drawn as a solid line in Fig. 49a, is based on this approximation. The Si solute concentration decreases from  $c_s$  to  $c_i$  over a distance of the effective diffusion length  $L$ . Whilst the Si grains are growing, the depletion regions are pushed further into the Al matrix (Fig. 49b). When the distance between adjacent grains is finally smaller than twice the effective diffusion length, the depletion regions begin to overlap (Fig. 49c). At this stage of the crystallization process the concentration of Si solute between the adjacent grains decreases below  $c_s$ , and the possibility of further nuclei formation drops.

Thus, the Si grains growing within the Al matrix interfere via their Si depletion regions before actual impingement of neighbouring grains occurs. This interference of isolated grains at an early stage of ALILE leads to the suppression of new Si nuclei formation. The fewer grains nucleate, the better for the growth of large-grained poly-Si, according to the general rule of formation of large-grained material as stated above.

Since the Si concentration outside the depletion region is kept constant at  $c_s$  due to the continuous supply of Si atoms from the amorphous phase, it seems reasonable to assume that a steady-state diffusion establishes between  $c_i$  and  $c_s$ . Under these conditions, in conjunction with the assumption that the Al matrix is an isotropic medium, the Si

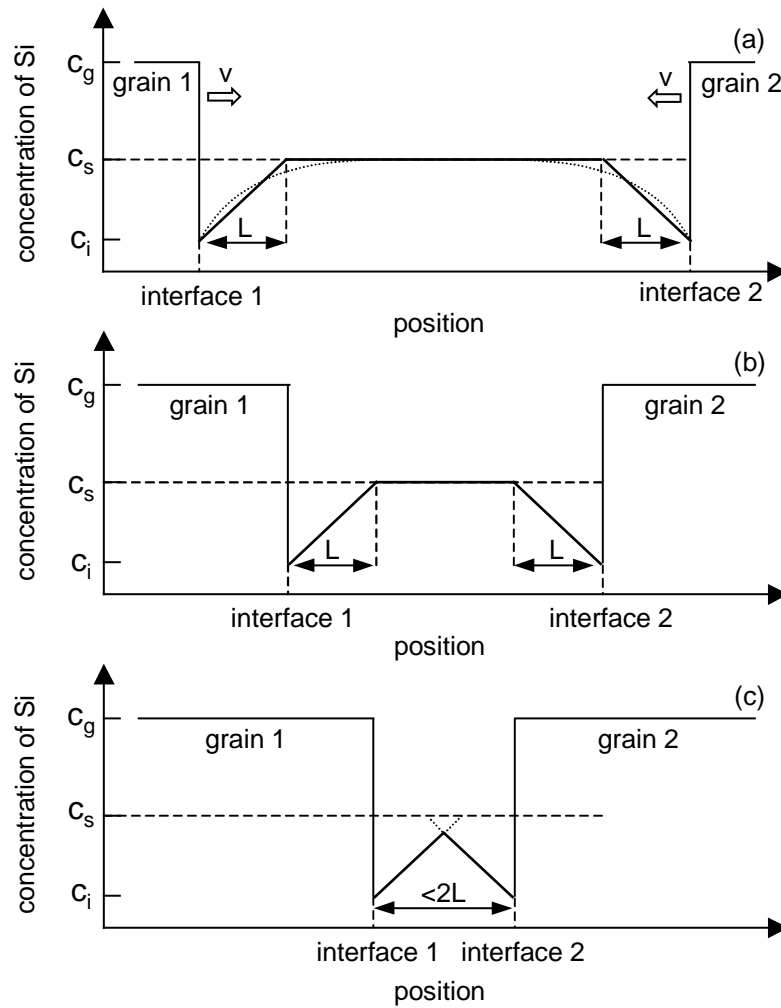


Fig. 49: Schematic diagram of the simplified concentration profile between two growing grains. (a) The grains are still far apart and grow with velocity  $v$  towards each other, (b) grain 1 and 2 are approaching each other, pushing the Si depletion areas with the effective diffusion length  $L$  further into the surrounding Al matrix, and (c) the distance between the grains is shorter than twice the effective diffusion length and the two depletion regions overlap.  $c_g$ ,  $c_s$  and  $c_i$  are the atomic Si density of a grain, the supersaturated Si concentration of the Al matrix when nucleation could occur, and the Si concentration of the Al solvent at the Si grain/Al matrix interface, respectively. The dotted curve between the grains in (a) resembles a realistic concentration profile, whilst the solid line represents the simplification.

concentration is related to the flux  $J$  of Si atoms toward the growing grain according to Fick's first law [133]:

$$J = -D \cdot \frac{dc}{dx} \quad (20)$$

As mentioned above, the concentration profile can be simplified using Zener's linear gradient approximation. Equation (21) can therefore be written as follows:

$$J = -D \cdot \frac{c_s - c_i}{L} \quad (21)$$

On the other hand the flux of Si solute is related to the advancing c-Si/Al growth front due to the conservation of Si atoms according to

$$J = c_g \cdot v \quad (22)$$

with  $c_g$  being the atomic density of crystalline silicon and  $v$  the growth velocity of the radius of the Si grain. Using equations (21) and (22) the effective diffusion length  $L$  can be calculated for a sample annealed at 475°C, analysed in chapter 4.1. The concentration  $c_i$  at the Al/c-Si interface is set equal to the solid solubility of Si in Al considering an Al/c-Si system at 475°C ( $c_i = 0.5$  at.% [130]). The kinetic barrier between the growing crystalline Si grain and the surrounding Al matrix is neglected because of the incoherent nature of the interface.  $c_s$  is the supersaturation concentration of Si in Al as determined for an Al/a-Si system in the previous chapter and represents the upper limit. The atomic densities of Al and Si are  $6 \times 10^{22} \text{ cm}^{-3}$  and  $5 \times 10^{22} \text{ cm}^{-3}$ , respectively. The velocity  $v$  of the crystallization front was determined in chapter 4.1 to be about 4.7 nm/s. Again using a diffusivity of  $10^{-8} \text{ cm}^2/\text{s}$ , the effective diffusion length  $L$  is calculated to be about 6  $\mu\text{m}$ . This means that the depletion regions of two neighbouring grains begin to overlap when the distance between their growth fronts is less than 12  $\mu\text{m}$ .

According to the above model the formation of new Si nuclei is reduced when overlapping of Si depletion regions commences. The nucleation rate should therefore significantly decrease at this stage of the crystallization process. The nucleation rate is the increase of the number of grains and can be extracted from the in-situ optical investigations presented in chapter 4.1. The crystallization analysis was carried out using optical micrographs before impingement of neighbouring grains occurred. Fig. 50 shows the development of the grain density (filled squares) as extracted from the in-situ investigation of a sample annealed at 475°C (see also Fig. 9 and Fig. 10, which are extracted from the same set of data). Two time periods can be clearly distinguished. During the first period, at times shorter than 35 min, the grain density increases rapidly. In the second period, at times longer than 35 min, the grain density increases much more slowly and eventually seems to saturate, although no impingement has yet occurred, and less than 40 % of the poly-Si film has formed (see Fig. 10). The linear fits in both regions serve as guides to the eye to highlight when the change of nucleation rate occurs. At this stage of the discussion,

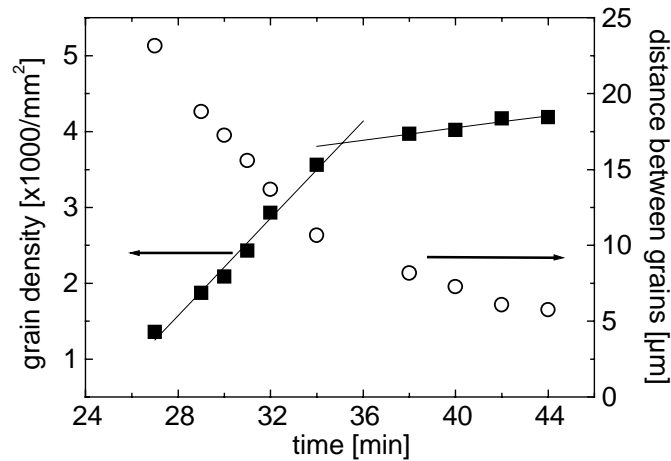


Fig. 50: Time dependence of the Si grain density (filled square) and the average distance between the crystallization fronts of neighbouring grains (open circles). The data is extracted from in-situ optical microscopy investigation of an Al-induced layer exchange process at 475°C.

it is of interest to determine the distance between neighbouring grains at the time of this qualitative change.

The time dependence of the average distance between the growing grains can be extracted using the Si grain density. To do so, it is assumed that the Si grains are homogeneously spread over the Al matrix and have an identical average size as determined from the grain size distributions, partially shown in Fig. 9 of chapter 4.1. The resulting time dependence of the average distance between neighbouring grains is also shown in Fig. 50 (open circles). From this data the distance between grains, at the time when the nucleation rate changes significantly, can be estimated. The data point closest to 35 min reveals that the average distance between neighbouring grains at this stage of the crystallization process is about 11  $\mu\text{m}$ . This distance is in good agreement with the calculated value of 12  $\mu\text{m}$  for the separation of neighbouring grains when their Si depletion regions begin to overlap according to the model presented. The model predicts that with the overlapping of the depletion regions the formation of new nuclei decreases significantly. This is exactly the result depicted in Fig. 50. The in-situ optical microscopy investigations therefore support the model presented.

**Summary:** The growing crystalline Si grains induce a Si depletion region extending from the advancing c-Si/Al growth front into the Al matrix. According to a simplified model based on a linear concentration gradient approximation, the depletion regions reach several microns into the Al in the temperature range investigated. Once the depletion regions of neighbouring grains begin to

overlap, the model predicts a significant change in the nucleation rate. This change was found in the analysis of in-situ optical investigations. It occurs when the average distance between neighbouring grains is about 11  $\mu\text{m}$  for a sample annealed at 475°C. This value is in good agreement with the predicted value of 12  $\mu\text{m}$ . The interference of grains via their Si depletion regions leads to the suppression of new nuclei formation at an early stage of the layer exchange process, the prerequisite for the growth of large-grained poly-Si films. Thus, the model presented successfully explains why the Al-induced layer exchange process can lead to the formation of poly-Si films with grain sizes exceeding 10  $\mu\text{m}$ .

## 6.5 Discussion

In the last chapters, a model of the aluminium-induced layer exchange was developed by analysing the individual process steps of the a-Si dissociation, the crystallization and the Si grain growth. In this chapter, the model will be critically discussed taking some of the results presented in chapters 4 and 5 into consideration. Table 5 lists some of the process parameters that influence the grain size of the poly-Si films formed during ALILE as well as the overall crystallization velocity. These parameters will be related to the model of ALILE. Additionally, the thermodynamic reasoning for the one-way process of a-Si dissociation and yet c-Si formation, presented in chapter 6.3, will be discussed.

process parameters	Si grain size	crystallization velocity	chapter
Annealing temperature $\uparrow$	$\downarrow$	$\uparrow$	4.3
Al grain size $\uparrow$	$\uparrow$	$\downarrow$	4.4
interface oxide $\uparrow$	$\uparrow$	$\downarrow$	4.5.1

Table 5: List of process parameters that influence the grain size and the crystallization velocity. The arrow  $\uparrow$  indicates an increase in annealing temperature, grain size of the polycrystalline Al or the thickness of the interface oxide, as well as an increase in grain size of the poly-Si and the crystallization process velocity. The arrow  $\downarrow$  indicates the opposite.

In chapter 4.5.3 it is shown that no Al/Si layer exchange occurs without an interface oxide, although crystallization is induced by the Al. This highlights the point that an oxide layer between the Al and a-Si layers is a mandatory requirement for the successful layer exchange. However, little is still known about the role of the interface oxide. To achieve a

better insight, the structure of this interface layer has to be investigated using cross-section high resolution TEM, for example. To study the role of Al and/or Si oxide interfaces efficiently, the Al, the oxide and the a-Si layers should be deposited under well-defined conditions in an integrated deposition system. Such an experimental set-up could provide important details concerning the interface oxide as process parameter and regulator of ALILE.

In chapter 4.5.1 it was shown that the thicker the interface oxide, the larger the Si grains, but the slower the crystallization process. The oxide influences the initial interaction of the Al and the a-Si. Before any interaction can occur, diffusion paths through the interface oxide have to develop. A thicker oxide therefore decelerates the overall crystallization process. When a-Si dissociation through the membrane-like oxide occurs, followed by Si diffusion, grains can finally form within the Al. These grains deplete the surrounding Al solvent of Si solute. In the model presented, the Si concentration outside the effective diffusion regions is kept constant due to the continuous supply of Si from the a-Si. It is assumed that a steady-state diffusion between  $c_s$  and  $c_i$  establishes. However, if a thicker interface oxide hampers the Si supply, this steady state condition might not develop, and the effective diffusion length  $L$  of the Si grains keeps on increasing until neighbouring depletion regions begin to overlap. In this case, a time dependent description of  $L$  ought to be incorporated into the model.

In chapter 6.3, the difference of chemical potentials at the a-Si/Al and the Al/c-Si interfaces was suggested as the driving force for the one-way process of a-Si dissociation and crystallization of Si grains. However, even crystalline Si wafer are partially dissolved when in contact with Al [109]. Si is dissolved up to the solid solubility limit of the Al/c-Si system. Magee and Peng's study on the interaction of polycrystalline Al in contact with crystalline silicon showed that the dissolved silicon crystallized at the Al grain boundaries [134]. It has already been mentioned that Al grain boundaries are preferential nucleation sites. The grain boundaries could be regarded as sites where Si supersaturation locally occurs within the polycrystalline Al structure, although the Al grains themselves are not supersaturated. The thermodynamic description presented in chapter 6.3 for an a-Si/Al/c-Si system seems to be unsuited to discuss the interaction of Al with crystalline Si. A description would have to be developed that took the inhomogeneous crystallographic structure of evaporated Al into consideration. This description could then be extended and incorporated into a model of ALILE.

The model of the formation of large-grained poly-Si is based on the simplified, one-dimensional linear gradient profile of the Si concentration in Al. The assumption is made that there is a steady-state diffusion between the supersaturation concentration  $c_s$  and the Al/Si grain interface concentration  $c_i$ .  $c_s$  is the upper limit of the Si solute in Al. This concentration was extracted using the activity differences of Si atoms in the Al/a-Si and the Al/c-Si systems. For the particular set of samples analysed in chapter 6.4,  $c_s$  was determined to be 6 times as large as the Si concentration in Al when in thermal equilibrium with c-Si. However, Si crystallization becomes likely to occur as soon as the solid solubility limit of Al is exceeded, which is below  $c_s$ . The model therefore implies that the a-Si dissociation and Si diffusion is fast compared to the nucleation, and the high activity of Si in the a-Si/Al system practically *presses* the Si atoms into the Al up to a supersaturation concentration  $c_s$  as the upper limit.  $c_i$ , on the other hand, is taken as the solid solubility concentration of the Al/c-Si system. It represents the lower Si concentration limit at the interface, since the time needed for the incorporation process of the Si atoms from the Al solution into the crystalline Si phase is neglected. Under these circumstances the growth process is entirely diffusion controlled [68]. However, if the interface kinetics cannot be neglected, the process is mixed controlled by diffusion and interface reactions, and the concentration at the interface would be higher. Directly measured values for both concentrations,  $c_s$  and  $c_i$ , would consequently allow a more detailed analysis of the overall aluminium-induced layer exchange. The difficulty is that the measurements would have to be time-dependent, in-situ and with high spatial resolution.

In chapter 6.4, the formation of large-grain poly-Si is related to the interference of the Si depletion regions surrounding neighbouring grains. It is proposed that this interference leads to the suppression of further Si nucleation. The quantitative analysis of this interference process is dependent on the Si concentration profile within the Al matrix. The model presented uses the approximation of a linear gradient profile of the Si concentration inside the Si depletion regions. The model could therefore be improved by applying a more sophisticated description of the concentration profile. Allen et al. have investigated the interaction of microcrystalline Si in contact with a thin-film of Au [49]. They developed a model for the concentration profile that was based on the continuity equation, relating the dissolution of Si to the diffusion and growth of stable Si grains within the metal layer. The effective diffusion length  $L$  in their model was set equal to  $\sqrt{d \cdot D/B}$ , with  $d$  being the metal layer thickness,  $D$  the diffusivity and  $B$  the dissolution rate of the microcrystalline Si in contact with Au. Scranton and McCaldin conducted studies on the dissolution rate of

amorphous silicon in contact with evaporated Al [103], however, their published values scatter significantly. It seems that there are no more reliable values of the dissolution rate of amorphous Si into Al available, as yet. The adaptation of Allen and co-workers' more sophisticated Si concentration profile to ALILE does therefore not improve the model in a way that it could be related to experimental results in a non-ambiguous way.

In chapter 4.3 it was shown that the grain size of the poly-Si films is temperature dependent: The lower the annealing temperature, the larger the grain size. The grain size of polycrystalline material is determined by the competing processes of nucleation and grain growth, as discussed chapter 6.4. From the analysis of ALILE, it seems that the nucleation rate decreases more strongly than the Si grain growth velocity with decreasing temperature, which explains the reciprocal dependence of grain size and annealing temperature. In chapter 6.1, the activation energy of the thermally activated Al-induced layer exchange process was determined to be 1.3 eV. To discuss the temperature dependence of the Si grain size quantitatively, it would be necessary to separate this overall activation energy into the activation energies of nucleation and grain growth. The requirement for that is the independent observation of both processes. However, existing grains suppress the formation of new Si nuclei at an early stage of the crystallization process, as was shown in chapter 4.1. Extracting an independent activation energy for the nucleation rate is therefore difficult. A better in-situ optical microscopy system, than the system available in this study, would be required. The system used only had a magnification of 100. With a higher magnification, the Si grain growth process could be observed at a stage before significant interference of neighbouring grains occurred.

**Summary:** The model developed in this work for the Al-induced layer exchange process is separated into process steps concerning the dissociation of the a-Si, the Si diffusion within the Al, the Si nucleation and the Si grain growth. Several ways to refine this model have been highlighted in this chapter. The comprehensive description of the overall layer exchange including its main sub-processes in the previous chapters can be seen as the basis for further investigations focusing on individual process mechanisms of ALILE.

## Chapter 7:

# Al-induced layer exchange for thin-film solar cells

The aluminium-induced layer exchange process enables the fabrication of large-grained continuous poly-Si thin-films (ALILE poly-Si) on glass substrates at low temperatures as shown throughout the previous chapters. In this chapter, it will be discussed how these poly-Si layers can be incorporated into Si thin-film solar cell fabrication. The concepts that will be presented point in various directions. This reflects that the use of ALILE for solar cells is in the beginning stage, and there is enormous room for improvement. The default structure investigated in this work led to poly-Si thin-films with a thickness of less than 0.5  $\mu\text{m}$ . This chapter will therefore begin with the discussion of using these very thin films as seeding layers for subsequent epitaxial growth. Since the large Si grains are of good crystallographic quality, the possibility of using ALILE poly-Si as absorber layers is addressed in the second part. All the investigations in this chapter rely completely on experience and results of studies presented and discussed in the previous chapters. It is the first step to applying ALILE in solar cell preparation.

## 7.1 ALILE engineering for seeding layers

The seeding layer concept is based on the idea that a very thin large-grained poly-Si film induces epitaxial growth when a thicker absorber layer of several  $\mu\text{m}$  in thickness is deposited. Large-grained seeding layers are formed by transforming a-Si or  $\mu\text{c-Si}$  material on foreign substrates to poly-Si utilising crystallization techniques. In the high-temperature approach ( $T > 550^\circ\text{C}$ ), zone melting recrystallization processes are common techniques [17]. The epitaxial thickening can be carried out using liquid phase epitaxy [135], ion-assisted deposition (IAD) [136] or chemical vapour deposition (CVD) [17], for example. Efficiencies as high as 9.4 % have been reported [137].

In the low-temperature approach, solid phase crystallization and laser crystallization are the most commonly applied methods for processing seeding layers. The subsequent thickening layer is deposited using CVD or IAD. For example, the company Kaneka investigated laser crystallized poly-Si thin-films as seeding layers using plasma-enhanced CVD for the subsequent deposition of the absorber layers [138,139]. In more recent publications, it seems, however, that the seeding layer concept was dropped. Cross-section TEM investigations indicated that Kaneka's laser crystallized poly-Si films did not induce epitaxial growth [138]. The absorber layers are now grown onto an unspecified back reflector [14,140]. One of the main obstacles of the seeding layer concept is that epitaxial Si growth preferentially occurs on crystalline silicon with (100) orientation [85]. However, SPC and LC lead to poly-Si thin-films with no texturing or preferred (111) orientation [83,84]. In contrast, poly-Si formed by aluminium-induced layer exchange exhibits a (100) texturing as shown in chapter 5.2. This effect in conjunction with large grain sizes makes ALILE poly-Si films an interesting candidate for seeding layers.

The seeding layer concept is applicable for either superstrate or substrate cell configurations. In a superstrate solar cell, the actual diode is illuminated through the glass. Consequently, a front contact on the glass is needed prior to any film deposition. Thin conducting oxides (TCO) commonly serve this purpose. Since the TCO is the first layer deposited, all following processing steps have to be compatible with the maximum temperature this layer can be exposed to.

The Al-induced layer exchange of a glass/Al/a-Si structure leads to the formation of a poly-Si film directly on glass (see Fig. 3c of chapter 2.2). If the glass was initially covered with a TCO, the structure could be used for subsequent superstrate cell fabrication. Since the poly-Si films are highly Al doped, the solar cell structures deposited could either be superstrate/TCO/p<sup>+</sup>-Si/i-Si/n-Si/back contact or superstrate/TCO/p<sup>+</sup>-Si/n-Si/back contact. In both cases the main concern would be how much the TCO is effected by annealing temperatures of 400°C to 500°C and/or whether interaction with the Al occurs, which is initially adjacent to the TCO. These difficulties can be avoided when a substrate configuration is utilised. In this configuration the solar cell is illuminated from the top and the glass substrate serves as a mere carrier. The front contact TCO is the last layer deposited. The temperature sensitivity of this film does therefore not hamper the previous layer depositions. Nevertheless, a back contact has to be incorporated between the glass substrate and the ALILE poly-Si film.

A glass/back contact/poly-Si structure for the substrate/seeding layer configuration can be realised in a couple of ways using the aluminium-induced layer exchange process. Fig. 51 shows a glass/Al 1/Al 2/a-Si layer structure. Al 1 and Al 2 were thermally evaporated at a high (7-10 nm/s) and a low (1-2 nm/s) deposition rate, which leads to the formation of large-grained and small-grained polycrystalline Al, respectively (see chapter 4.4). Grey variations in the Al films due to ion channelling contrast give an indication for the different grain sizes. After the deposition of Al 1 the sample was exposed to air for a short period of time (~2 min). A thin Al oxide layer therefore separates the two metal films. The double Al structure was also exposed to air prior to the a-Si sputtering deposition (a few hours). A second Al oxide layer was therefore located at the Al/a-Si interface. Fig. 51b shows that only the small-grained Al layer participated in the layer exchange process. This finding can be explained considering that ALILE is faster in small-grained Al. As soon as a continuous poly-Si film has formed in the AL 2 layer, the Al 1 layer is separated from the amorphous Si and the diffusion of Si atoms from the amorphous phase is blocked. Only few Si grains

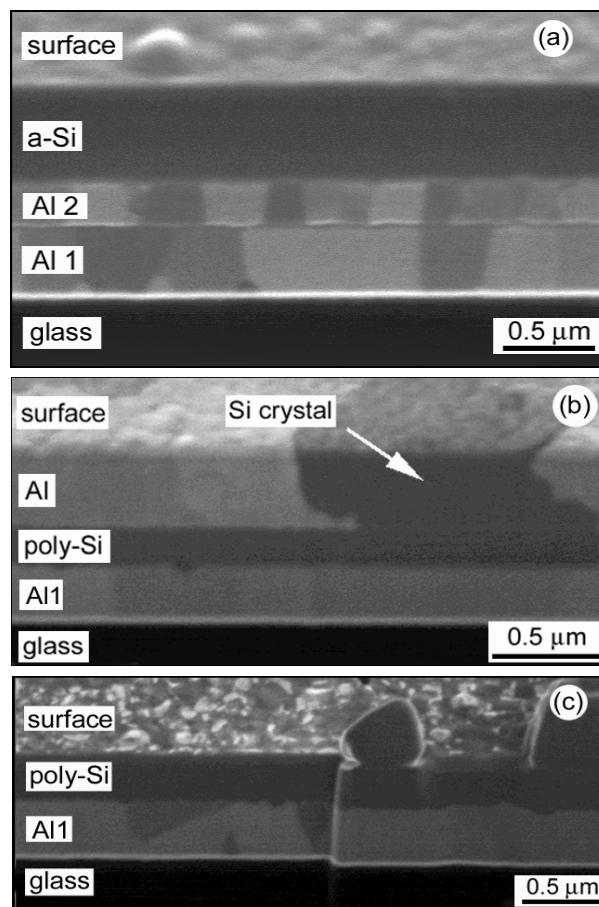


Fig. 51: FIB cross section micrographs of a glass/Al 1/Al 2/a-Si layer system. Al 1 and Al 2 are large-grained and small-grained layers, respectively. The layer structure is shown (a) before annealing, (b) after annealing at 475°C for one hour, and (c) after Al etching. The samples are tilted by 45°.

sporadically formed within Al 1. The role of the two Al oxide interface layers in this selective aluminium-induced layer exchange process is, as yet, subject to speculations. After Al etching, the poly-Si film on the substrate/Al structure is accessible. Raman spectroscopy measurements revealed spectra identical to the spectrum shown in Fig. 5 of chapter 2.2.

One of the most challenging problems concerning the seeding layer concept is the surface conditioning for subsequent epitaxial growth. The Si atoms during the thickening process have to be deposited onto a clean, pure Si surface of high crystallographic quality. Large-grained poly-Si films do not induce epitaxy when lower quality and/or oxide layers cover the surface. Unfortunately, both are the case in poly-Si films formed by ALILE using the layer structure investigated in Fig. 51. In chapter 4.2 it was discussed that it is beneficial to have a Si oversupply in relation to the Al film to ensure the formation of a continuous poly-Si film. The surplus of silicon manifests itself in form of Si crystallites within the Al that has segregated to the former position of the a-Si layer. Fig. 52a shows an especially "bad" sample in terms of potential use as seeding layer. An additional problem is the existence of an Al oxide layer on top of the poly-Si film, which was confirmed by XPS measurements similar to the investigations presented in chapter 4.5.2. To the best of the author's knowledge, there is no chemical etching solution that selectively attacks Al oxide without significantly removing Si, too.

The approach tested to remove the Si crystals as well as the Al oxide was Ar plasma etching. Various plasma powers, Ar pressures and etching times were studied (0.5-1,0 W/cm<sup>2</sup>, 5-30 Pa, 5-90 min). The success was limited as apparent from Fig. 52b. A large portion of the Si crystals and the Al oxide could be removed, but some of the larger or

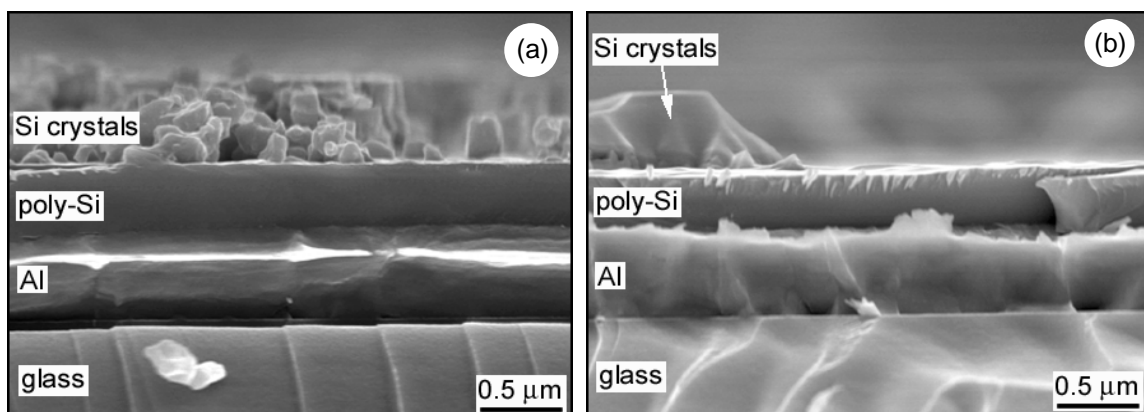


Fig. 52: Cross-section SEM images of an annealed glass/Al/poly-Si structure, (a) after Al etching and (b) after additional Ar plasma etching.

coalesced Si crystals were only slowly destroyed by the Ar bombardment. The processing has, however, not been optimised. The possibility remains that choosing the process parameters of the Al-induced layer exchange carefully and adapting the Ar plasma etching appropriately, smooth, Al oxide free surfaces could be prepared. However, Ar plasma etching causes defects in the surface region during etching. This problem can be solved, since wet chemical etching solutions exist, which preferentially remove defect-rich silicon in regards to crystalline Si, e.g.  $\text{HNO}_3/\text{HF}$  mixtures.

The challenges that arise from the occurrence of Si crystals on top of the continuous poly-Si film can be circumvented when starting off with a different layer structure than presented in Fig. 51a. First investigations using ALILE for the formation of seeding layers were conducted by annealing a glass/Al(300 nm)/a-Si (300 nm)/Al(150 nm) structure at 475°C for 120 min. Both interfaces were oxidised during sample transfer. Layer thicknesses, annealing time and annealing temperature have by no means been optimised. The growing poly-Si film replaced the top 150 nm thick Al layer during ALILE, as discussed in chapter 4.5.1. The a-Si layer was chosen to be twice as thick as the participating Al layer to ensure that a continuous poly-Si film was formed at the top. The surplus of Si and the repelled Al from the initial top Al film formed an Al+(Si) layer, sandwiched between the bottom Al and newly grown top poly-Si films. Fig. 21 of chapter 4.5.1 shows what a final glass/Al/Al+(Si)/poly-Si layer structure looks like. When the poly-Si film is formed at the top, the surface is much smoother than compared to the sample shown in Fig. 52a. However, this surface is also covered by patches of Al and Al oxide (some patches are visible in Fig. 21c and d). As mentioned above, a wet chemical etching step to remove this Si-Al-O phase at the surface does not seem applicable. Since this mixed phase would hamper the following epitaxial growth, it has to be removed prior to the deposition. One possible way is again Ar plasma etching. An alternative way is shown in Fig. 53. The poly-Si layer at the top is initially covered by the Si-Al-O phase. The thickness of this phase in relation to the poly-Si film is exaggerated in the figure. Its thickness seems to be only a few nm according cross section FIB and Auger electron spectroscopy investigations, which will be discussed later. The first step to clean the surface is an oxidation process that leads to the formation of Si oxide in the top region of the poly-Si film. The Si-Al-O phase is now separated from the poly-Si material by a  $\text{SiO}_2$  intermediate layer. This Si oxide layer can be selectively removed using dilute HF solution without damaging the underlying poly-Si material. After this final etching step a clean and bare poly-Si surface is exposed to subsequent Si deposition.

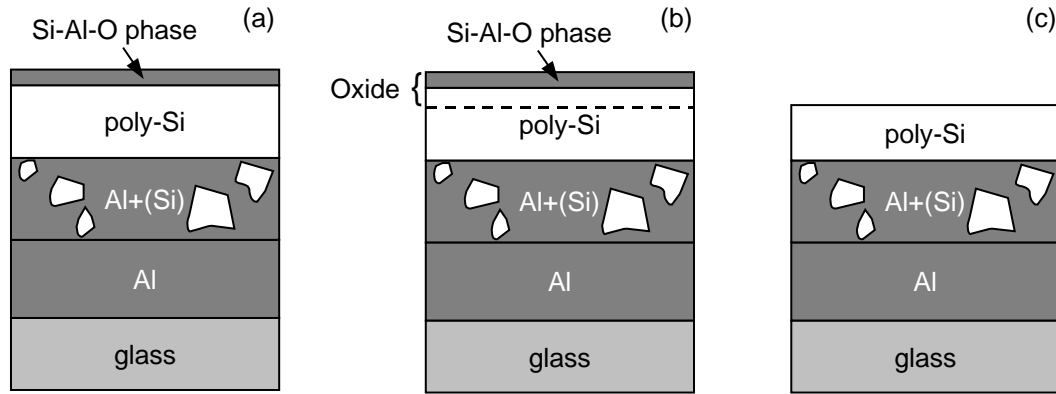


Fig. 53: Schematic diagram of an oxidation and etching procedure to remove the Si-Al-O phase from the poly-Si film of a glass/Al/Al+(Si)/poly-Si layer structure. The structure is sketched (a) after ALILE, (b) after Si oxide formation and (c) after selective removal of the SiO<sub>2</sub> surface layer together with the Si-Al-O phase.

Electrochemical oxidation seems to be a favourable method to oxidise the top fraction of the poly-Si layer in a very controlled and self-regulating manner. For the first investigation on using ALILE poly-Si as seeding layers, a SiO<sub>2</sub> film with a thickness of about 15 nm was formed in ethylene-glycol containing H<sub>2</sub>O using the technique developed by Lust et al. [141]. The remaining organic solvent on the surface after the oxidation was eliminated in a H<sub>2</sub>SO<sub>4</sub>/H<sub>2</sub>O cleaning step for 5 s. The Si oxide layer including the Si-Al-O phase was etched off in a 2% HF solution for 30 s. The success of this surface conditioning procedure was verified using Auger electron spectroscopy investigation (AES). Fig. 54 shows three AES depth profiles of the top poly-Si layer before the surface preparation, after oxidation and after oxide removal. To compare the sets of depth profiles, the front and the steep decreases of the Si response indicating the Al+(Si)/poly-Si interface are used as markers. Initially, the poly-Si film is covered by an Al oxide phase as apparent from the increased intensities of the oxygen and aluminium signals at the front (Fig. 54a). Both intensities decrease quickly according to the AES profiles. After the electrochemical oxidation the front oxide layer extends into the poly-Si film. The non-oxidised Si response (Si bonded silicon) does not increase until the oxygen level decreases. The oxidised poly-Si area is much thicker than the Al oxide phase at the surface (Fig. 54b). After the HF etching step the thick Si oxide region has been removed, and traces of an Al oxide phase have vanished. The onset of the depth profile shown in Fig. 54c is shifted to the decrease of the oxide signal in Fig. 54b to demonstrate that the top Si oxide region was etched off. It is worthwhile mentioning that the poly-Si film and the Al form a good ohmic contact according to current-voltage measurements despite the initially oxidised interfaces.

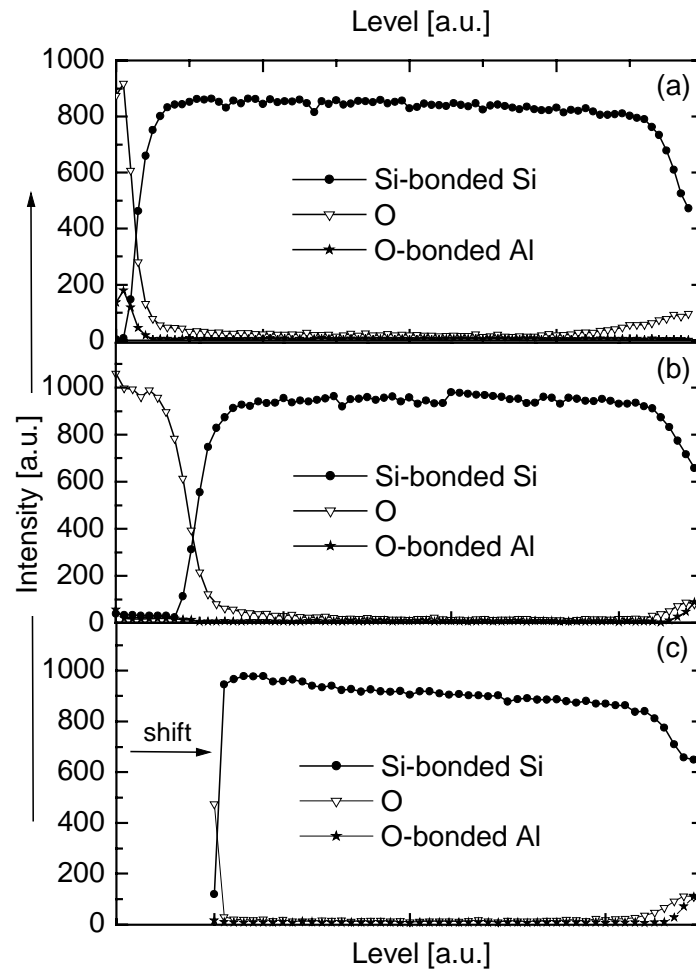


Fig. 54: Auger electron spectroscopy depth profiles taken (a) before the surface conditioning, (b) after electrochemical oxidation, and (c) after HF etching. The spectra in (c) were shifted so that the depth profile coincides with the end of the oxidised region in (b).

Once the surface conditioning procedure has been conducted, the poly-Si film is only covered by a natural Si oxide that forms on HF-etched, hydrogenated Si when the poly-Si surface is exposed to air. This native Si oxide is apparent from the increased oxygen signal at the very beginning of the depth profile in Fig. 54c. A major difficulty in ex-situ surface preparation of seeding layers is that the surface has to be free of any contamination or oxide, when the sample is loaded into the vacuum deposition system. An initial study on using ALILE for the preparation of seeding layers did not lead to epitaxial growth of the subsequently deposited Si film [142]. The deposition was carried out using electron cyclotron resonance CVD at a very low temperature (325°C). Nevertheless, with the deposition of Si on ALILE poly-Si layers the formation of the incubation phase of a-Si prior to the growth of  $\mu\text{c-Si}$  could be avoided. This amorphous incubation phase is typical for  $\mu\text{c-Si}$  deposition on foreign substrates. Consequently, the following process changes could lead to epitaxial growth of Si using CVD: (i) Higher deposition temperatures, but

below the Al/Si eutectic temperature of 577°C, and (ii) wet chemical etching steps (HF etching) in a N<sub>2</sub> ambient connected to the vacuum system to avoid surface oxidation and contamination prior to the deposition. Alternatively, in-situ surface conditioning could be developed.

In studies, where epitaxial growth was successfully induced by poly-Si layers, the Si surfaces were often either prebaked inside the deposition chamber or the deposition was carried out at high temperatures of about 1000°C [143]. The prebaking step comprises an annealing step at temperatures above 850°C prior to any deposition [144]. The benefit of a high temperature step is the removal of contamination and oxides from the surface. However, these high temperatures are not compatible with a true low-temperature approach with the aim of processing Si thin-film solar cells on glass substrates. The optimisation of the surface preparation is therefore probably one of the biggest experimental challenges. If this could be satisfactorily solved, poly-Si layers formed by the aluminium-induced layer exchange process seem to be ideal in terms of grain size, grain orientation and crystallographic quality plus the advantages of low-temperature processing using simple, industrially relevant deposition techniques.

**Summary:** The crystallographic and electrical qualities of ALILE poly-Si make the material a promising candidate for the seeding layer concept. Before successful implantation in solar cell fabrication is possible, the main obstacle to overcome is the surface conditioning due to harmful surface roughness and the inevitable surface Al oxide. The feasibility of different layer structures and surface conditioning techniques were discussed.

## 7.2 ALILE poly-Si absorber layers

In chapter 5.3 it was shown that poly-Si films formed using ALILE have a hole concentration is about  $2 \times 10^{18} \text{ cm}^{-3}$ . The high Al doping concentration is inherent to the aluminium-induced crystallization process. The Hall-mobilities of the holes are in the range of 55 to 70  $\text{cm}^2/\text{Vs}$  (see Fig. 42 of chapter 5.3). The electrical behaviour of the majority carriers is determined by the bulk properties of the crystalline Si grains. In monocrystalline silicon with doping concentration in this range the minority carrier lifetime is dominated by band-to-band Auger recombination [145]. The electron lifetime in

ALILE poly-Si p-type	50 nm emitter n-type	front surface recombination	rear side recombination	minority carrier lifetime
$2 \times 10^{18} \text{ cm}^{-3}$	$1 \times 10^{20} \text{ cm}^{-3}$	100 cm/s	10 cm/s	0.1 $\mu\text{s}$

Table 4: PC1D simulation parameters

p-type silicon with a doping concentration between  $10^{18}$  and  $10^{19} \text{ cm}^{-3}$  is between 1  $\mu\text{s}$  and 0.1  $\mu\text{s}$ , respectively [146].

Simulating Si thin-film solar cells with ALILE poly-Si as an absorber layer is difficult whilst no data on the minority carrier lifetime is available. Nevertheless, the device simulation program PC1D [147] can give an idea of the efficiency potential of pn solar cells based on poly-Si thin-films formed by the aluminium-induced layer exchange, even if crude assumptions have to be made concerning some cell parameters. The parameters used for the simulation are listed in table 4, whilst the ALILE poly-Si thickness is the simulation variable.

Values used for the rear and front side recombination are according to Bergmann et al. [144], who simulated 5  $\mu\text{m}$  thick Si thin-film solar cells grown onto laser crystallized seeding layers. Light trapping is incorporated by setting the internal reflectance at the rear surface to 100 % diffused and at the front surface to 50 % diffused. Fig. 55 shows the variation of the efficiency, the open circuit voltage and the short circuit current with increasing absorber layer thickness. It becomes apparent from the simulation that the efficiency achieves a maximum when the absorber layer is several  $\mu\text{m}$  in thickness and then decreases with increasing thickness again.

The general tendency of the efficiency probably stays the same, even if more accurate cell parameters are used. However, it has to be pointed out that interface recombination is neglected in the simulation. The highly doped n-type emitter could be regarded as an epitaxially grown Si film on the p-type ALILE poly-Si absorber layer. Furthermore, tunnelling recombination across the depletion region is not taken into account when using PC1D. The depletion layer width in the absorber of the simulated cell structure is about 20 nm.

If ALILE poly-Si is to serve as the absorber material, layer thicknesses of several  $\mu\text{m}$  are mandatory to achieve reasonable efficiencies ( $\sim 10\%$ ) according to the Si thin-film solar cell simulation. The aluminium-induced layer exchange studied in this work is based on an isothermal annealing step. So far, the poly-Si films prepared had a thickness of 0.5  $\mu\text{m}$  or less. Using the same procedure to prepare thicker films seems to be difficult.

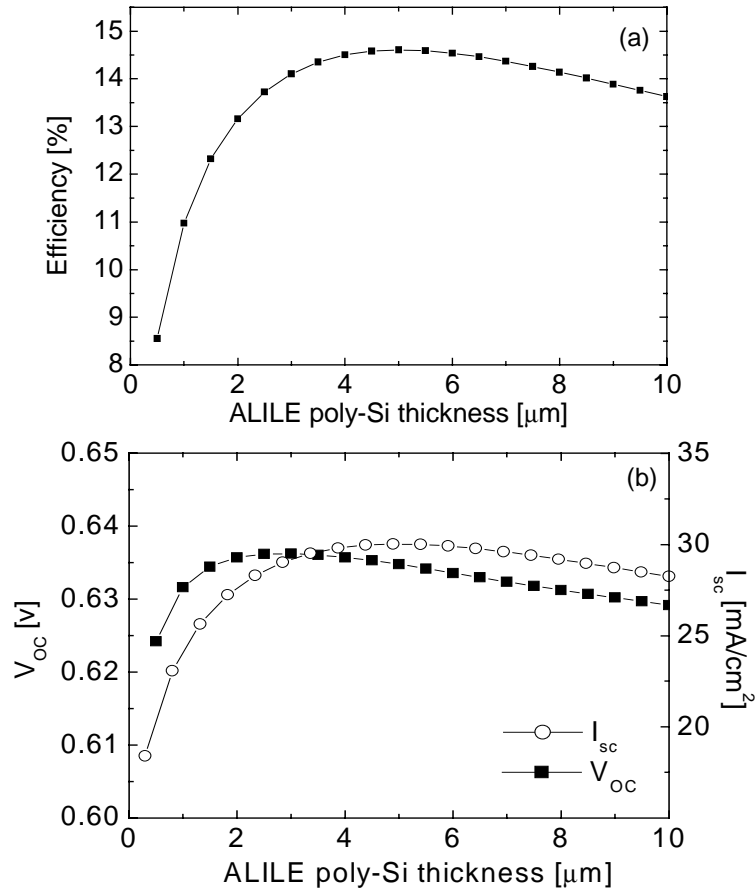


Fig. 55: Si thin-film solar cell simulation using PC1D. The cell parameters are documented in table 4.

The reason is rooted in the existence of inter- and intra-grain Al clusters as discussed in chapter 5.1. These Al clusters occur when the Si grains have impinged and form a continuous layer along the Al/a-Si interface before all Al has been repelled from its original position. Consequently, some Al can still be found near the substrate.

Fig. 56 reveals the problem when thicker Al/a-Si layer structures are isothermally annealed. The structure depicted initially consisted of a glass substrate with 4 μm Al and 4 μm a-Si deposited. Although a poly-Si film has formed, it did not replace the thick Al layer entirely. A large fraction of the Al remains at the substrate. The continuous poly-Si film along the interface blocks the diffusion of the Si atoms from the amorphous phase into the Al film and therefore further Si crystallization. The layer exchange process terminates at this stage. Even extended annealing (>50 h) does not seem to have any effect on this final state. The top layer is a mixture of segregated Al and partially crystallized Si according to Raman spectroscopy. Throughout chapter 4, a whole set of process parameters of ALILE was discussed. There might be a possibility of choosing these parameters appropriately, so an entire layer exchange can be achieved even with layers of a couple of μm in thickness. The general direction for choosing the parameters would be to

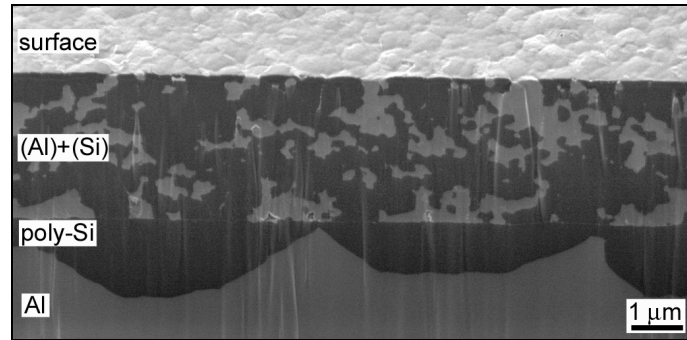


Fig. 56: Cross section FIB micrograph of an annealed sample with an initial layer structure of 4  $\mu\text{m}$  Al and 4  $\mu\text{m}$  a-Si. The sample was annealed at 425°C for 60 h.

aim for a low nucleation rate. The fewer grains form, the larger they can grow before impingement occurs. The grain sizes ought to exceed the Al layer thickness many times even if this thickness is several  $\mu\text{m}$ . The Al that induces the crystallization process has to be repelled from its original position before a continuous poly-Si film forms.

Substituting the isothermal annealing step might be a possible way to form ALILE poly-Si films with several  $\mu\text{m}$  in thickness. Temperature gradient and locally varying temperature profile annealing processes are currently under investigation. The research direction, which might lead to successful preparation of thick ALILE poly-Si films, is still open. The a-Si/Al structures investigated in this work were chosen to enable the detailed study of the aluminium-induced layer exchange process. The rudimentary process can be extended in many directions; varying the layer structure, the annealing procedure, the deposition parameters, even the crystallization inducing metal provides a wide range of possibilities. It is likely that one of these paths will lead to the formation of poly-Si films based on the metal-induced layer exchange process, which is feasible for Si thin-film solar cell fabrication.

**Summary:** Using ALILE poly-Si films as absorber material in Si thin-film solar cells is an entirely new field. The main concern is the process inherent high doping concentration. Due to the high crystallographic quality of the poly-Si films there is a chance that the minority carrier lifetime is only limited by Auger recombination and not by grain boundary or inner-grain defects. If this is the case, it is likely that solar cell efficiencies of over 10 % could be achieved. The most difficult obstacle that has to be overcome is to process poly-Si films of several  $\mu\text{m}$  in thickness using ALILE. It seems that a significantly different annealing concept than isothermal annealing will have to be applied. If the

aluminium-induced layer exchange process can be extended in this direction maintaining its simplicity, it will be a promising candidate to form large-grained polycrystalline silicon films on foreign-substrates at low temperatures using industrially relevant techniques.

# Chapter 8:

## Conclusions

In this work, the aluminium-induced layer exchange process (ALILE) is investigated. ALILE is based on aluminium-induced crystallization, which is the phenomenon of the transformation of amorphous to crystalline silicon when in contact with Al at temperatures well below the Al/Si eutectic temperature of 577°C. Throughout this study, it is shown for the first time that aluminium-induced crystallization of a-Si can instigate a complete layer exchange of adjacent a-Si and Al films on foreign substrates. During this exchange process a continuous poly-Si film is formed.

ALILE is influenced by a list of process parameters: (i) The annealing time, (ii) the ratio of the a-Si and Al layer thicknesses, (iii) the annealing temperature, (iv) the structure of the polycrystalline Al, (v) the interface oxide layer and (vi) the layer sequence. In this work the aluminium-induced layer exchange process as well as the material properties of the poly-Si film on glass are studied. From these investigations the following results are extracted:

- The a-Si is dissociated by the adjacent Al layer. The dissolved Si atoms crystallize within the polycrystalline aluminium. The Si grain growth is vertically confined by the substrate and the a-Si/Al interface. Laterally the grains can grow within the Al matrix to sizes of several  $\mu\text{m}$  in diameter before impingement of neighbouring grains occurs. The Al is repelled from the advancing crystallization front of the Si grains and occupies the space of the former a-Si layer. The overall reaction is therefore the layer exchange.
- The annealing temperature influences the grain size of the poly-Si film in a way that the lower the temperature, the larger the Si grains. However, the overall layer exchange process is significantly slowed down at lower temperatures. Processing times needed might then exceed one hour. It is also shown that the lower the temperature, the more prevalent the dendritic Si growth within the Al matrix.
- Because the grain boundaries of the polycrystalline Al are preferential nucleation sites for the Si solute, it is found that the higher the density of Al grain boundaries, the

higher the Si nucleation rate, and the faster the exchange process, but the smaller the grains of the continuous poly-Si film.

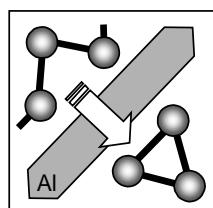
- The interface oxide between the Al and a-Si layers is a mandatory requirement for the successful layer exchange. The interface consists of a stable Al oxide. If Si oxide initially separates the two layers, the SiO<sub>2</sub> is reduced to Al oxide. The oxide layer remains between the two films, although practically all Al and Si atoms exchange sides with respect to the interface. The oxide interface also enables the selective layer exchange in a stacked layer system, e.g. a glass/Al/a-Si/Al structure transforms to glass/Al/Al/poly-Si during ALILE.
- The continuous poly-Si films have an Al concentration of about  $3 \times 10^{19} \text{ cm}^{-3}$ . Besides these Al atoms incorporated within the poly-Si film, the poly-Si/substrate system additionally contains intra- and inter-grain Al clusters, which are sporadically trapped between the glass and the Si film.
- The poly-Si films can consist of grains, whose lateral diameter exceed 10  $\mu\text{m}$ . Some of the larger grains exhibit a subgrain structure where coincident site lattice grain boundaries with coincidence index  $\Sigma 3$  and  $\Sigma 9$  separate areas of different crystallographic orientation. These twin boundaries develop during the growth of individual Si grains. The grains have a preferential (100) orientation.
- A large share of the incorporated Al occupies substitutional Si lattice sites. The Al atoms introduce acceptor levels in the Si band structure and give rise to a hole concentration of about  $2 \times 10^{18} \text{ cm}^{-3}$ . The Hall mobility of the majority carriers is in the range of 55-70 cm/Vs. The hole concentration as well as the hole mobility vary little with annealing temperature.

The attempt is made to give a comprehensive model of the aluminium-induced layer exchange, although little is still known about some of the sub-steps of the process. It is suggested that the driving force for the dissociation of a-Si and yet the formation of c-Si is the chemical potential difference of Si atoms at the a-Si/Al and the Al/c-Si interfaces. The description of the formation process of large-grained poly-Si during ALILE is based on the model of interfering Si grains at an early stage of the crystallization process. It is proposed that existing grains deplete the adjacent Al matrix. The Si depletion regions therefore extend from the advancing Si crystallization front into the Al solvent. When the Si depletion regions of neighbouring grains begin to overlap, the formation of new Si nuclei is suppressed. Since the grain density is kept low because of this interference mechanism,

the individual grains can grow to large sizes before a continuous poly-film is formed. It is pointed out that the main open question is the particular role of the interface oxide. Different types of investigations are suggested to elucidate in more detail this interface oxide layer.

The aluminium-induced layer exchange process investigated in this work fits well within the low-temperature approach to fabricate poly-Si thin-film solar cells. The main advantages of the layer exchange process are: (i) Low processing temperature ( $<550^{\circ}\text{C}$ ), (ii) cost-efficient substrates (glass), (iii) industrially relevant deposition techniques (thermal evaporation and sputtering deposition), (iii) relatively short crystallization time ( $\sim 30$  min) and (iv) simple. For the time being, ALILE is the only true low-temperature process that can combine all these characteristics. Especially in comparison with solid phase and laser crystallization, the aluminium-induced layer exchange process seems to be a very promising candidate for processing of large-grained poly-Si films on foreign substrates within the framework of the low-temperature approach. The main obstacles that seem to hamper the successful use of poly-Si films formed using ALILE are (a) the high doping concentration and (b) the difficulty in processing films with several  $\mu\text{m}$  in thickness. The high doping concentration is an inherent characteristic of the aluminium-induced crystallization process, which might restrict the application of these films to the use as seeding layers for subsequent epitaxial growth. The difficulty of forming several  $\mu\text{m}$  thick poly-Si layers might be overcome by substituting the isothermal annealing process used in this work with more sophisticated annealing procedures.

The study on metal-induced crystallization of amorphous silicon presented in this work focused on the aluminium-induced layer exchange. Due to the success in forming large-grained poly-Si in a simple way at low temperatures, it is an exciting field for further investigations. The work discussed here is only the tip of the iceberg for the fabrication of large-grained poly-Si thin-films based on a metal-induced layer exchange process. Different metals, that induce the Si crystallization, varying layer structures and modified annealing procedures are imaginable and could lead to a new way of processing poly-Si films on foreign, low-cost substrates for Si thin-film device applications.





# References

- [1] K. Zweig and M. A. Green, *Progr. Photovolt.* **8**, 1 (2000).
- [2] S. H. Kim, C. MacCracken, and J. Edmonds, *Progr. Photovolt.* **8**, 3 (2000).
- [3] G. Giroult-Matlakowski, "Photovoltaic Market Analysis," presented at the *2nd World Conference and Exhibition on Photovoltaic Energy Conversion*, (Vienna, 1998), p.3403.
- [4] A. Shah, P. Torres, R. Tscharnner, N. Wyrsh, and H. Keppner, *Science* **285**, 692 (1999).
- [5] Z. Shi and M. A. Green, *Progr. Photovolt.* **6**, 247 (1998).
- [6] W. Fuhs and R. Klenk, "Thin-Film Solar Cells-Overview," presented at the *2nd World Conference and Exhibition on Photovoltaic Energy Conversion*, (Vienna, 1998), p.381.
- [7] A. V. Shah, R. Platz, and H. Keppner, *Sol. En. Mat. and Sol. Cells* **38**, 501 (1995).
- [8] V. M. Fthenakis and P. D. Moskowitz, *Progr. Photovolt.* **8**, 27 (2000).
- [9] B. A. Andersson, *Progr. Photovolt.* **8**, 61 (2000).
- [10] O.-A. Neumüller, *Römpps Chemie-Lexikon*, 7 ed. (Franckh'sche Verlangshandlung, Stuttgart, 1975).
- [11] J. H. Werner, R. Bergmann, and R. Brendel, "The Challenge of Crystalline Thin Film Silicon Solar Cells," in *Festkoerperprobleme/Advances in solid state physics*, edited by R. Helbig (Vieweg, Braunschweig, 1995), Vol. 34, p. 115.
- [12] R. Brendel, R. B. Bergmann, P. Lolgen, M. Wolf, and J. H. Werner, *Appl. Phys. Lett.* **70**, 390 (1997).
- [13] D. Thorp, P. Campbell, and S. R. Wenham, *Progr. Photovolt.* **4**, 205 (1996).
- [14] K. Yamamoto, M. Yoshimi, Y. Tawada, Y. Okamoto, A. Nakajima, and S. Igari, *Appl. Phys. A* **69**, 179 (1999).
- [15] R. B. Bergmann, *Appl. Phys. A* **69**, 187 (1999).
- [16] R. E. I. Schropp and M. Zeman, *Amorphous and Microcrystalline Silicon Solar Cells: Modeling, Materials and Device Technology* (Kluwer Academic, Boston, 1998).
- [17] S. Reber and W. Wettling, *Appl. Phys. A* **69**, 215 (1999).
- [18] R. B. Bergmann, G. Oswald, M. Albrecht, and V. Gross, *Sol. En. Mat. and Sol. Cells* **46**, 147 (1997).

- [19] C. Spinella, S. Lombardo, and F. Priolo, *J. Appl. Phys.* **84**, 5383 (1998).
- [20] K. Ishikawa, M. Ozawa, C.-H. Oh, and M. Matsumura, *Jpn. J. Appl. Phys.* **37**, 731 (1998).
- [21] R. S. Sposili and J. S. Im, *Appl. Phys. Lett.* **69**, 2864 (1996).
- [22] J. S. Im, H. J. Kim, and M. O. Thompson, *Appl. Phys. Lett.* **63**, 1969 (1993).
- [23] G. Andrä, J. Bergmann, F. Falk, and E. Ose, "Laser induced liquid phase crystallization of amorphous silicon films on glass for thin film solar cells," presented at the *14th European Photovoltaic Solar Energy Conference*, (Barcelona, 1997), p.1400.
- [24] S. R. Herd, P. Chaudhari, and M. H. Brodsky, *J. Non-Crystall. Solids* **7**, 309 (1972).
- [25] T.-K. Kim, T.-H. Ihn, B.-I. Lee, and S.-K. Joo, *Jpn. J. Appl. Phys.* **37**, 4244 (1998).
- [26] J. Jang, J. Y. Oh, S. K. Kim, Y. j. Choi, S. Y. Yoon, and C. O. Kim, *Nature* **395**, 481 (1998).
- [27] L. K. Lam, S. K. Chen, and D. G. Ast, *Appl. Phys. Lett.* **74**, 1866 (1999).
- [28] M. Boreland, K. Yamaguchi, K. Okitsu, M. Imaizumi, and M. Yamaguchi, "One Step Aluminium Induced Crystal Growth of nc-Si Thin Films Using Electron Beam Excited Plasma Chemical Vapour Deposition," presented at the *16th European Photovoltaic Solar Energy Conference and Exhibition*, (Glasgow, 2000).
- [29] S. Summers, L. Wang, H. S. Reehal, and G. J. Hirst, "Excimer laser and aluminium-induced crystallisation of silicon thin films on foreign substrates for solar cells," presented at the *16th European Photovoltaic Solar Energy Conference and Exhibition*, (Glasgow, 2000).
- [30] K. Shirasawa, H. Senta, H. Hakuma, M. Komoda, K. Fukui, and K. Niira, "Thin film poly-Si formation for solar cells by flux method, CAT-CVD method & PECVD Method," presented at the *16th European Photovoltaic Solar Energy Conference and Exhibition*, (Glasgow, 2000).
- [31] R. Bergmann, J. Kühnle, and J. H. Werner, "Polycrystalline silicon for thin film solar cells," presented at the *1st World Conference on Photovoltaic Energy Conversion*, (Hawaii, 1994), p.1398.
- [32] Z. Shi, T. L. Young, and M. A. Green, "Solution growth of polycrystalline silicon on glass at low temperatures," presented at the *1st World Conference on Photovoltaic Energy Conversion*, (Hawaii, 1994), p.1579.
- [33] T. Matsuyama, T. Baba, T. Tsuyoshi, S. Tsuda, and S. Nakano, *Sol. En. Mat. and Sol. Cells* **34**, 285 (1994).

- [34] J.-S. Maa and S.-J. Lin, *Thin-Solid-Films* **64**, 63 (1979).
- [35] B. Bian, J. Yie, B. Li, and Z. Wu, *J. Appl. Phys.* **73**, 7402 (1993).
- [36] L. Hultman, A. Robertsson, H. T. G. Hentzell, I. Engström, and P. A. Psaras, *J. Appl. Phys.* **62**, 3647 (1987).
- [37] S. F. Gong, H. T. G. Hentzell, A. E. Robertsson, L. Hultman, S. E. Hörnström, and G. Radnoczi, *J. Appl. Phys.* **62**, 3726 (1987).
- [38] S. W. Russell, L. Jian, and J. W. Mayer, *J. Appl. Phys.* **70**, 5153 (1991).
- [39] S. Y. Yoon, K. Ki Hyung, K. Chae Ok, O. Jae Young, and J. Jin, *J. Appl. Phys.* **82**, 5865 (1997).
- [40] T. B. Massalski, *Binary Alloy Phase Diagrams*, 2nd ed. (ASM International, Materials Park, Ohio, 1990).
- [41] M. S. Ashtikar and G. L. Sharma, *J. Appl. Phys.* **78**, 913 (1995).
- [42] C. Hayzelden and J. L. Batstone, *J. Appl. Phys.* **73**, 8279 (1993).
- [43] Z. Jin, G. A. Bhat, M. Yeung, H. S. Kwok, and M. Wong, *J. Appl. Phys.* **84**, 194 (1998).
- [44] J. L. Batstone and C. Hayzelden, *Solid State Phenomena* **37-38**, 257 (1994).
- [45] C. C. Tsai, R. J. Nemanich, and M. J. Thompson, *J. Vac. Sci. Technol.* **21**, 632 (1982).
- [46] T. J. Konno and R. Sinclair, *Mater. Sci. Engin.* **A179/A180**, 426 (1994).
- [47] T. J. Konno and R. Sinclair, *Philosophical Magazine B* **66**, 749 (1992).
- [48] L. H. Allen, J. R. Phillips, D. Theodore, C. B. Carter, R. Soave, J. W. Mayer, and G. Ottaviani, *Phys. Rev. B* **41**, 8203 (1990).
- [49] L. H. Allen, J. W. Mayer, K. N. Tu, and L. C. Feldman, *Phys. Rev. B* **41**, 8213 (1990).
- [50] J. M. Harris, R. J. Blattner, I. D. Ward, C. A. Evans, H. L. Fraser, M. A. Nicolet, and C. L. Ramiller, *J. Appl. Phys.* **48**, 2897 (1977).
- [51] K. Nakamura, M.-A. Nicolet, J. W. Mayer, R. J. Blattner, and C. A. Evans, Jr, *Appl. Phys. Lett.* **46**, 4678 (1975).
- [52] G. Majni and G. Ottaviani, *Appl. Phys. Lett.* **31**, 125 (1977).
- [53] B. Y. Tsaur, G. W. Turner, and J. C. C. Fan, *Appl. Phys. Lett.* **39**, 749 (1981).
- [54] L. M. Koschier, S. R. Wenham, M. Gross, T. Puzzer, and A. B. Sproul, "Low temperature junction and back surface field formation for photovoltaic devices," presented at the *2nd World Conference and Exhibition on Photovoltaic Energy Conversion*, (Vienna, 1998), p.1539.
- [55] S. R. Wenham, L. M. Koschier, O. Nast, and C. B. Honsberg, *IEEE Transactions on Electron Devices* **46**, 2005 (1999).

- [56] F. A. Trumbore, *Bell Syst. Tech. J.* **39**, 205 (1960).
- [57] S. M. Sze, *Physics of Semiconductor Devices*, 2 ed. (Wiley & Sons, New York, 1981).
- [58] T. P. Drüsedau, J. Bläsing, and H. Gnaser, *Appl. Phys. Lett.* **72**, 1510 (1998).
- [59] T. P. Drüsedau, A. Diez, and J. Blasing, *Thin Solid Films* **337**, 41 (1999).
- [60] S. A. Lyon, R. J. Nemanich, N. M. Johnson, and N. M. Biegelsen, *Appl. Phys. Lett.* **40**, 316 (1982).
- [61] H. Richter, Z.P.Wang, and L. Ley, *Solid State Communication* **39**, 625 (1981).
- [62] P. M. Fauchet and I. H. Campbell, *Mat. Res. Soc. Symp. Proc.* **164**, 259 (1990).
- [63] W. Kern, *J. Electrochem. Soc.* **137**, 1887 (1990).
- [64] T. K. Olson, R. G. Lee, and J. C. Morgan, "Contrast Mechanisms in Focused Ion Beam Imaging," presented at the *18th International Symposium for Testing & Failure Analysis*, (Los Angeles, California, 1992), p.373.
- [65] B. L. Adams, S. I. Wright, and K. Kunze, *Metallurgical Transactions A* **24A**, 819 (1993).
- [66] J. I. Goldstein and H. Yakowitz, *Practical Scanning Electron Microscopy* (Plenum Press, New York, 1975).
- [67] M. Schuster and H. Göbel, *Adv. X-Ray Anal.* **39**, 1 (1996).
- [68] D. A. Porter and K. E. Easterling, *Phase Transformations in Metals and Alloys*, 2nd ed. (Chapman&Hall, London, 1992).
- [69] E. B. Graper, *J. Vac. Sci. Technol.* **9**, 33 (1971).
- [70] P. G. Shewmon, "Diffusion," in *Physical Metallurgy*, edited by R.W. Cahn (North-Holland Publishing Company, Amsterdam, 1970), p. 383.
- [71] S. A. Flodstrom, R. Z. Bachrach, R. S. Bauer, and S. B. M. Hagström, *Phys. Rev. Lett.* **37**, 1282 (1976).
- [72] J. L. Vossen and J. J. Cuomo, in *Thin Film Processes*, edited by J.L. Vossen and W. Kern (Academic, New York, 1987).
- [73] F. J. Grunthaner, P. J. Grunthaner, R. P. Vasques, B. F. Lewis, and J. Maserjian, *Phys. Rev. Lett.* **43**, 1683 (1979).
- [74] R. D. Thompson and K. N. Tu, *Appl. Phys. Lett.* **41**, 440 (1982).
- [75] H. Nagel, A. G. Aberle, and S. Narayanan, *Solid State Phenomena* **67-68**, 503 (1999).
- [76] J. A. Venables and C. J. Harland, *Philos. Mag.* **27**, 1193 (1979).
- [77] D. G. Brandon, *Acta Metallurgica* **14**, 1479 (1966).
- [78] A. V. Nikoaleva and Y. A. Nikoalev, *Materials-Science-Forum* **207-209**, 657 (1996).

- [79] A. Fedotov, B. Evtodyi, L. Fionova, Y. Ilyashuk, E. Katz, and L. Polyak, *Physica-Status-Solidi-A* **119**, 523 (1990).
- [80] A. Fedotov, B. Evtody, L. Fionova, J. Ilyashuk, E. Katz, and L. Poljak, *J. Cryst. Growth* **104**, 186 (1990).
- [81] M. Birkholz, S. Fiechter, A. Hartmann, and H. Tributsch, *Phys. Rev. B* **43**, 11926 (1991).
- [82] National Bureau of Standards, NBS Standard Reference Material No. 640. Report No. Vol. 13, 1976.
- [83] L. Haji, P. Joubert, J. Stoemenos, and N. A. Economou, *J. Appl. Phys.* **75**, 3944 (1994).
- [84] S. Loreti, M. Vittori, L. Mariucci, and G. Fortunato, *Solid State Phenomena* **67-68**, 181 (1999).
- [85] J. Platen, B. Selle, I. Sieber, U. Zimmer, and W. Fuhs, *Mat. Res. Soc. Symp. Proc.* **570**, 91 (1999).
- [86] T. Noma, T. Yonehara, and H. Kumomi, *Appl. Phys. Lett.* **59**, 653 (1991).
- [87] S. Selberherr, *Analysis and Simulation of Semiconductor Devices* (Springer, Vienna, 1984).
- [88] Landolt-Börnstein, "Numerical Data and Functional Relationships in Science and Technology", edited by M. Schulz (Springer, Berlin, 1989), Vol. III/22b.
- [89] W. R. Thurber, R. L. Mattis, and Y. M. Liu, *J. Electrochem. Soc.* **127**, 1807 (1980).
- [90] C. S. Hung and J. R. Gliessman, *Phys. Rev.* **96**, 1226 (1954).
- [91] R. N. Bhatt and T. M. Rice, *Phys. Rev. B* **23**, 1920 (1981).
- [92] H. Ibach and H. Lüth, *Festkörperphysik*, 4 ed. (Springer-Verlag, Berlin, 1995).
- [93] J. Y. W. Seto, *J. Appl. Phys.* **46**, 5247 (1975).
- [94] R. Enderlein and N. J. M. Horing, *Fundamentals of semiconductor physics and devices* (World Scientific, Singapore, 1997).
- [95] M. A. Green, *J. Appl. Phys.* **67**, 2944 (1990).
- [96] J. S. Blakemore, *Semiconductor Statistics*, Dover edition (General Publishing Company, Toronto, 1987).
- [97] R. A. Gudmundsen and J. Maserjian, *J. Appl. Phys.* **28**, 1308 (1957).
- [98] J. H. Kim and J. Y. Lee, *Jpn. J. Appl. Phys.* **35**, 2052 (1996).
- [99] M. S. Haque, H. A. Naseem, and W. D. Brown, *J. Appl. Phys.* **75**, 3928 (1994).
- [100] T. Ito and Y. Nakayama, *Transactions of the Japanese Institute of Metals* **25**, 375 (1984).

- [101] U. Köster, *phys. stat. sol. (a)* **48**, 313 (1978).
- [102] J. O. McCaldin and H. Sankur, *Appl. Phys. Lett.* **19**, 524 (1971).
- [103] R. A. Scranton and J. O. McCaldin, *J. Vac. Sci. Technol.* **15**, 1358 (1978).
- [104] J. O. McCaldin, *J. Vac. Sci. Technol.* **11**, 990 (1974).
- [105] C. Anandan, *Appl. Surf. Sci.* **89**, 57 (1995).
- [106] R. S. Bauer and R. Z. Bachrach, *Appl. Phys. Lett.* **37**, 1006 (1980).
- [107] R. Z. Bachrach and R. S. Bauer, *J. Vac. Sci. Technol.* **16**, 1149 (1979).
- [108] J. A. Dean, *Lange's Handbook of chemistry*, 13 ed. (McGraw-Hill Book Company, New York, 1985).
- [109] A. Bierhals, A. G. Aberle, and R. Hezel, *J. Appl. Phys.* **83**, 1371 (1998).
- [110] K.-N. Tu, J. W. Mayer, and L. C. Feldman, *Electronic Thin Film Science* (Macmillan Publishing Company, New York, 1992).
- [111] G. Ottaviani and G. Majni, *J. Appl. Phys.* **50**, 6865 (1979).
- [112] H. Qingheng, E. S. Yang, and H. Izmirliyan, *Solid-State Electronics* **25**, 1187 (1982).
- [113] K. N. Tu, *Appl. Phys. Lett.* **27**, 221 (1975).
- [114] A. Hiraki, *J. Electrochem. Soc.* **127**, 2662 (1980).
- [115] M. S. Haque, H. A. Naseem, and W. D. Brown, *J. Appl. Phys.* **79**, 7529 (1996).
- [116] A. Hiraki, *Surf. Sci.* **168**, 74 (1986).
- [117] P. W. Anderson, "Many-body effects at surfaces," in *Elementary Excitations in Solids, Molecules and Atoms Part A*, edited by J.A. Devreese, A.B. Kunz, and T.C. Collins (Plenum Press, 1974), p. 1.
- [118] J. C. Inkson, *Surf. Sci.* **28**, 69 (1971).
- [119] A. Okiji, H. Kasai, and S. Terakawa, *J. Phys. Soc. Jap.* **44**, 1275 (1978).
- [120] G. Margaritondo, J. E. Rowe, and S. B. Christman, *Phys. Rev. B* **14**, 5396 (1976).
- [121] G. Radnoczi, A. Robertsson, H. T. G. Hentzell, S. F. Gong, and M. A. Hasan, *J. Appl. Phys.* **69**, 6394 (1991).
- [122] R. M. Walser and Bené, *Appl. Phys. Lett.* **28**, 624 (1976).
- [123] R. W. Bené, *J. Appl. Phys.* **61**, 1862 (1987).
- [124] A. E. Robertson, L. G. Hultman, H. T. G. Hentzell, S.-E. Hornstrom, and G. Shaofang, *J. Vac. Sci. Technol. A* **5**, 1447 (1987).
- [125] H. T. G. Hentzell, A. Robertsson, L. Hultman, G. Shaofang, S. E. Hörnström, and P. A. Psaras, *Appl. Phys. Lett.* **50**, 933 (1987).
- [126] A. D. Pelton, "Thermodynamics and Phase Diagrams of Materials," in *Phase Transformations in Materials*, edited by P. Haasen (VCH, Weinheim, 1991), Vol. 5.

- [127] E. P. Donovan, F. Spaepen, D. Turnbull, J. M. Poate, and D. C. Jacobson, *Appl. Phys. Lett.* **42**, 698 (1983).
- [128] F. Spaepen, *Philos. Mag.* **30** (1974).
- [129] P. W. Atkins, *Physical Chemistry* (Oxford University Press, Oxford, 1998).
- [130] G. J. van Gorp, *J. Appl. Phys.* **44**, 2040 (1973).
- [131] J. W. Christian, *The Theory of Transformations in Metals and Alloys*, 1st ed. (Pergamon Press, Oxford, 1965).
- [132] C. Zener, *J. Appl. Phys.* **20**, 950 (1949).
- [133] G. E. Murch, "Diffusion in Crystalline Solids," in *Phase Transformations in Materials*, edited by Peter Haasen (VCH, Weinheim, 1991), Vol. 5, p. 75.
- [134] T. J. Magee and J. Peng, *J. Appl. Phys.* **49**, 4284 (1978).
- [135] T. Kunze, S. Hattmann, J. Seekamp, and J. Müller, "Recrystallized and epitaxially thickened poly-Si layers on graphite substrates," presented at the *26th IEEE Photovoltaic Specialists Conference*, (Anaheim, CA, 1997).
- [136] R. B. Bergmann, C. Zaczek, N. Jansen, S. Oelting, and J. H. Werner, *Appl. Phys. Lett.* **72**, 2996 (1998).
- [137] S. Reber, G. Stollwerck, D. Osswald, T. Kieliba, and C. Häbeler, "Crystalline silicon thin-film solar cells on silicon nitride ceramics," presented at the *16th European Photovoltaic Solar Energy Conference and Exhibition*, (Glasgow, 2000).
- [138] K. Yamamoto, A. Nakashima, T. Suzuki, and M. Yoshimi, *Jpn. J. Appl. Phys.* **33**, L1751 (1994).
- [139] A. Nakajima, T. Suzuki, M. Yoshimi, and K. Yamamoto, "Low temperature fabrication and properties of the thin film polycrystalline Si solar cell on the glass substrate," presented at the *13th EU Photovoltaic Solar Energy Conf.*, (Nice, 1995), p.1550.
- [140] K. Yamamoto, M. Yoshimi, T. Suzuki, Y. Okamoto, Y. Tawada, and A. Nakajima, "Thin film poly-Si solar cell with "STAR Structure" on glass substrate fabricated at low temperature," presented at the *26th IEEE Photovoltaic Specialists Conference*, (Anaheim, 1997), p.575.
- [141] S. Lust, J. Rappich, I. Sieber, W. Henrion, and W. Fuhs, presented at the *16th European Photovoltaic Solar Energy Conference*, (Glasgow, 2000).
- [142] M. Birkholz, O. Nast, K. Kliefoth, E. Conrad, J. Rappich, P. Reinig, and W. Fuhs, "Microcrystalline silicon grown on large-grained polycrystalline silicon formed by

- aluminium-induced crystallisation,” presented at the *16th European Photovoltaic Solar Energy Conference*, (Glasgow, UK, 2000).
- [143] R. Brendel, R. B. Bergmann, B. Fischer, J. Krinke, R. Plieninger, U. Rau, J. Reiß, H. P. Strunk, H. Wanka, and J. H. Werner, “Transport Analysis for Polycrystalline Silicon Solar Cells on Glass Substrates,” presented at the *26th IEEE Photovoltaic Specialists Conference*, (Anaheim, CA, 1997), p.635.
- [144] R. B. Bergmann, R. M. Hausner, N. Jensen, M. Grauvogl, L. Oberbeck, T. Rinke, M. B. Schubert, C. Zaczek, R. Dassow, J. R. Köhler, U. Rau, S. K. Oelting, J. , H. P. Strunk, and J. H. Werner, “High Rate, Low Temperature Deposition of Crystalline Silicon Films for Thin Film Solar Cells on Glass,” presented at the *2nd World Conference and Exhibition on Photovoltaic Solar Energy Conversion*, (Vienna, 1998), p.1260.
- [145] M. A. Green, *Silicon Solar Cells: Advanced Principles & Practice* (Centre for Photovoltaic Devices and Systems, University of New South Wales, Roseberry, 1995).
- [146] J. Dziwior and W. Schmid, *Appl. Phys. Lett.* **31**, 346 (1977).
- [147] D. A. Clugston and P. A. Basore, presented at the *26th IEEE Photovoltaic Specialists Conference*, (Picataway, 1997), p.207.

# Acknowledgments

I would like to thank Prof. W. Fuhs from the Hahn-Meitner-Institut Berlin (HMI) for his fantastic support of my research project from idea to finish. Many thanks also to Profs. M. A. Green and S. R. Wenham, who made it possible for me to conduct the majority of my work at the Photovoltaic Special Research Centre (PVSRC - now Centre for Photovoltaic Engineering), University of New South Wales, Sydney. Without their support, this work would not have been possible.

I would like to thank Prof. G. Weiser for accepting to be co-referee of this thesis.

Many thanks to ALL the members of the PVSRC for the wonderful, interesting time I had there. My special thanks go to Drs. Tom Puzzer and Mark Gross for their brilliant help in deposition and microscopy matters. Thanks heaps to Drs. Matt Boreland and Pietro Altermatt. Furthermore, I'd like to thank Drs. Aihua Wang and Jianhua Zhao, as well as Dr. Armin G. Aberle for his support after he became head of the thin-film group at the end of 1998. And, of course, many thanks to the legendary legends of room 132, Dirk-Holger Neuhaus, Keith McIntosh and Stephen Pritchard.

I would like to thank Dr. Cheng Tsien Chou from Pacific Solar, Sydney, for the orientation imaging microscopy measurements, and Dr. Andreas J. Hartmann from the Centre for Surface Science and Technology, University of New South Wales for the XPS measurements.

I would like to thank ALL my colleagues from the HMI, in particular Drs. Stephan Brehme, Mario Birkholz, Klaus Lips for measurements and discussions. Thanks to Dr. A. Schöpke and Mr. Matthias Rebien for AES and ellipsometry measurements, respectively. I'd also like to thank Dr. Jörg Rappich, Ms. G. Keiler, Ms. M. Schmidt, Mr. Peter Reinig and Mr. René Linke for their support in sample preparation during my time at the HMI.

I acknowledge the financial support from the German Academic Exchange Service under the HSPIII program.

AND, I am indebted to each one of the Coogee Gang for a fabulous time down under and above all to Nicola Hartley.



# List of publications

Some of the results presented in this work have been published in scientific journals and presented at conferences. The publications are as follows:

- O. Nast and A. J. Hartmann, "Influence of interface and Al structure on layer exchange during aluminium-induced crystallization of amorphous silicon", *Journal of Applied Physics* **88**, 716 (2000).
- O. Nast and S. R. Wenham, "Elucidation of the layer exchange mechanism in the formation of polycrystalline silicon by aluminum-induced crystallization" *Journal of Applied Physics* **88**, 124 (2000).
- O. Nast, S. Brehme, S. Pritchard, A. G. Aberle, and S. R. Wenham, "Aluminium-induced crystallisation of silicon on glass for thin-film solar cells", *Solar Energy Materials and Solar Cell* **65**, 385 (2001).
- O. Nast, S. Brehme, D.-H. Neuhaus, and S. R. Wenham, "Polycrystalline silicon thin-films on glass by aluminium-induced crystallization", *IEEE Transactions on Electron Devices* **46**, 2062 (1999).
- O. Nast, T. Puzzer, L. M. Koschier, A. B. Sproul, and S. R. Wenham, "Aluminium-Induced Crystallization of Amorphous Silicon on Glass Substrates above and below the Eutectic Temperature", *Applied Physics Letters* **73**, 3214 (1998).
- S. R. Wenham, L. M. Koschier, O. Nast, and C. B. Honsberg, "Thyristor Photovoltaic Devices Formed by Epitaxial Growth", *IEEE Transactions on Electron Devices* **46**, 2005 (1999).
- O. Nast, T. Puzzer, C. T. Chou, and M. Birkholz, "Grain size and structure analysis of polycrystalline silicon on glass formed by aluminium-induced crystallization for thin-film solar cells, " presented at the 16<sup>th</sup> European Photovoltaic Solar Energy Conference and Exhibition, Glasgow, 1-5 May 2000.
- O. Nast, S. Brehme, S. Pritchard, A. G. Aberle, and S. R. Wenham, "Aluminium-Induced Crystallization of Silicon on Glass for Thin-Film Solar Cells," *PVSEC-11, Technical Digest*, p.727, Sapporo, 21-24 Sept. 1999.

- M. Birkholz, O. Nast, K. Kliefoth, E. Conrad, J. Rappich, P. Reinig, and W. Fuhs, “Microcrystalline silicon grown on large-grained polycrystalline silicon formed by aluminium-induced crystallization”, presented at 16<sup>th</sup> European Photovoltaic Solar Energy Conference and Exhibition, Glasgow, 1-5 May 2000.
- O. Nast, “Grain Size and structure engineering during Al-induced crystallization for Si thin-film solar cells,” presented at the 28<sup>th</sup> IEEE Photovoltaic Specialists Conference, Anchorage, 11-17 Sept. 2000.
- N.-P. Harder, J. A. Xia, S. Oelting, O. Nast, and A. G. Aberle, “Low-temperature epitaxial thickening of sub-micron poly-Si seeding layers made by aluminium-induced crystallization,” presented at the 28<sup>th</sup> IEEE Photovoltaic Specialists Conference, Anchorage, 11-17 Sept. 2000.

Oliver Nast:

**The aluminium-induced layer exchange forming polycrystalline silicon  
on glass for thin-film solar cells**

(Dissertation, Philipps-Universität Marburg 2000)

## **Abstract**

The processing of large-grained polycrystalline silicon (poly-Si) on low-cost and low-temperature substrates is still one of the great obstacles to overcome on the way to cheap silicon thin-film solar cells with high efficiencies. Large-grained poly-Si films on glass are currently formed using laser or solid phase crystallization of amorphous silicon (a-Si). Both crystallization methods have significant draw-backs. In this work, the aluminium-induced layer exchange process (ALILE) is investigated as an alternative crystallization method. ALILE is based on aluminium-induced crystallization, which is the phenomenon of the transformation of amorphous to crystalline silicon when in contact with Al at temperatures well below the Al/Si eutectic temperature of 577°C. Throughout this study, it is shown for the first time that aluminium-induced crystallization of a-Si can instigate a complete layer exchange of adjacent a-Si and Al films on foreign substrates. During this exchange process a continuous poly-Si film is formed when annealed between 350° and 525°C, the temperature range investigated. The aluminium-induced layer exchange process itself as well as the material properties of the poly-Si films on glass are studied. Films with grain sizes exceeding 10 µm can easily be achieved in less than 1 h. Electrical investigations reveal that the poly-Si material has a hole concentration of about  $2 \times 10^{18} \text{ cm}^{-3}$  at room temperature, due to incorporation of Al atoms on substitutional lattice sites. To explain the aluminium-induced layer exchange process, a thermodynamic diffusion model is presented. Additionally, possible applications of the poly-Si films as part of thin-film solar cell structures are discussed.